Exhumation history of the metal-rich Chinese Altai: insights from apatite fission track thermochronology

Thesis submitted in accordance with the requirements of the University of Adelaide for an Honours Degree in Geology

Cameron Warren
October 2019

Word Count: 7067
13 Figures and 4 Tables

THE UNIVERSITY of ADELAIDE

EXHUMATION HISTORY OF THE METAL-RICH CHINESE ALTAI: INSIGHTS FROM APATITE FISSION TRACK THERMOCHRONOLOGY

RUNNING TITLE

Exhumation history of the metal-rich Chinese Altai

ABSTRACT

The Chinese Altai is located in northern China and represents a section of the Altai Mountain range that extends through Mongolia to the east, Kazakhstan to the west and Siberia to the north. The Altai is one of the key structures of the Central Asian Orogenic Belt, which is the world's largest intracontinental orogen. This study uses apatite U-Pb and fission track analysis on granitoid samples to constrain the post-magmatic cooling and exhumation history of the Chinese Altai. The apatite samples yield Lower Devonian-Jurassic U-Pb dates, which reflect cooling contemporaneous with (1) the subduction and closure of the Palaeo-Asian Ocean (2) regional oroclinal bending and (3) the Qiangtang collision. Apatite fission track data record varying thermal histories with respect to faults and shear zones that dissect the study area. The analysed samples preserve three cooling histories, (1) fast cooling in the Early Jurassic in response to the Qiangtang collision, (2) slow cooling or thermal quiescence during the Jurassic and Early Cretaceous, and/or (3) fast cooling in the mid-late Cretaceous in response to distant tectonic events such as mountain building in the Mongol Okhotsk Orogenic Belt or extension in the Tethys Ocean. Additionally, all models show rapid Neogene cooling (since ~ 30 Ma), which can be interpreted as a far-field response to the India-Eurasia collision and convergence. Cretaceous rapid cooling is primarily recorded to the east and along fault-splays of the Fuyun Fault, a major NNW-SSE strike slip fault in the study area. The results obtained in this study within the Chinese Altai are consistent with those of previous studies further west along other NW-SE orientated shear zones and contribute to our understanding of stress propagation throughout Central Asia in response to far-field tectonic stress tensors.

KEYWORDS

Chinese Altai, CAOB, Mesozoic, Cenozoic, thermal history, thermochronology, AFT, fault reactivation, Fuyun Fault, ISZ

TABLE OF CONTENTS

LIST OF FIGURES AND TABLES

1. INTRODUCTION

The Altai is a mountain range that is located on the borders of northern China, western Mongolia, eastern Kazakhstan and Siberia (Figure 1) and represents a key topographic feature within the Central Asian Orogenic Belt (CAOB). The CAOB is a widespread accretionary orogen that initiated in the Precambrian (~1000 Ma) and continued to form until the Palaeozoic (~250 Ma) (Windley, Alexeiev, Xiao, Kröner, & Badarch, 2007; Xiao et al., 2015). After its amalgamation, the CAOB has undergone several phases of intracontinental reactivation by tectonic drivers away from the plate margins. The case study for this thesis (the Chinese Altai) is situated along the northern border of China within the complex structural framework of the Irtysh and Fuyun Fault zones (Figure 2). It has been suggested that major shear zones in the Altai region record rapid cooling during the Cretaceous (Glorie, De Grave, Delvaux, et al., 2012; Nachtergaele et al., 2018; Yuan et al., 2006) in response to far field tectonic processes (Gillespie et al., 2017; Glorie, De Grave, Delvaux, et al., 2012; Jolivet et al., 2007). Yuan et al. (2006) suggested that the Cretaceous rapid cooling models, based on apatite fission track (AFT) results, could be linked with the collision of the Lhasa Block with Asia (De Grave, Buslov, & Van den haute, 2007); however, the development of the Mongol-Okhotsk Orogenic Belt (MOOB) (Glorie, De Grave, Buslov, et al., 2012; Jolivet et al., 2009; Metelkin, Vernikovsky, Kazansky, & Wingate, 2010) and extensional tectonics resultant of slab-rollback in the Tethys Ocean and/or West Siberian Basin (WSB) are also suggested to have reactivated the CAOB (Glorie et al., 2019; Jepson et al., 2018; Saunders, England, Reichow, & White, 2005). It is hypothesised that these Cretaceous regional tectonic events have propagated stress through the CAOB, which has initiated exhumation and mountain building events that ultimately led to the present day topography (De Grave et al., 2007; De Grave et al., 2012; Jolivet et al., 2007; Nachtergaele et al., 2018). The current deformation in southern Central Asia (e.g. in the Tian Shan) is considered to be related to the

India-Eurasia collision. A recent model by Van Hinsbergen et al. (2012) suggests the India-Eurasia collision can be explained by a change of intensity from a soft to a hard impact. The effects from this collision on northern Central Asia (such as within the Altai) is poorly understood.

The structural architecture of northern Chinese Altai is relatively well studied; however, the reactivation history of the Fuyun Fault is yet to be constrained. The Fuyun Fault runs NNW-SSE and offsets ore zones as well as a series of pre-existing NW-SE dextral strike slip faults including the Irtysh Fault (Figure 2). The Irtysh Shear Zone (ISZ) is a major tectonic boundary that runs through the CAOB and records 1000 km of lateral displacement, which occurred in the Permian (Glorie, De Grave, Delvaux, et al., 2012). In proximity to the ISZ, the Chinese Altai hosts three metallogenic belts which include a volcanogenic massive sulphide (VMS) Pb-Zn-Cu belt, shear zone related gold systems and porphyry Cu-Au-Mo deposits (Wan et al., 2011). For this study, our samples were taken across the three ore belts, aiming to examine potential relationships between fault reactivation, regional exhumation and ore deposit occurrences.

In more detail, this study aims to reconstruct the reactivation history of the Fuyun Fault and the ISZ using multi-method apatite thermochronology including fission track (AFT) analysis and uranium-lead (AU-Pb) dating. Based on thermal history models, the timing of exhumation/denudation will be determined, supported by the sedimentary stratigraphy in the nearby Junggar, Western Siberian and Ob-Zaisan basins. Subsequently, the potential causes of exhumation and fault reactivation will be discussed in a regional tectonic context. It is furthermore aimed to bridge a potential link between exhumation levels and the preservation of potential ore deposits.

2. GEOLOGICAL SETTING

2.1 Regional history

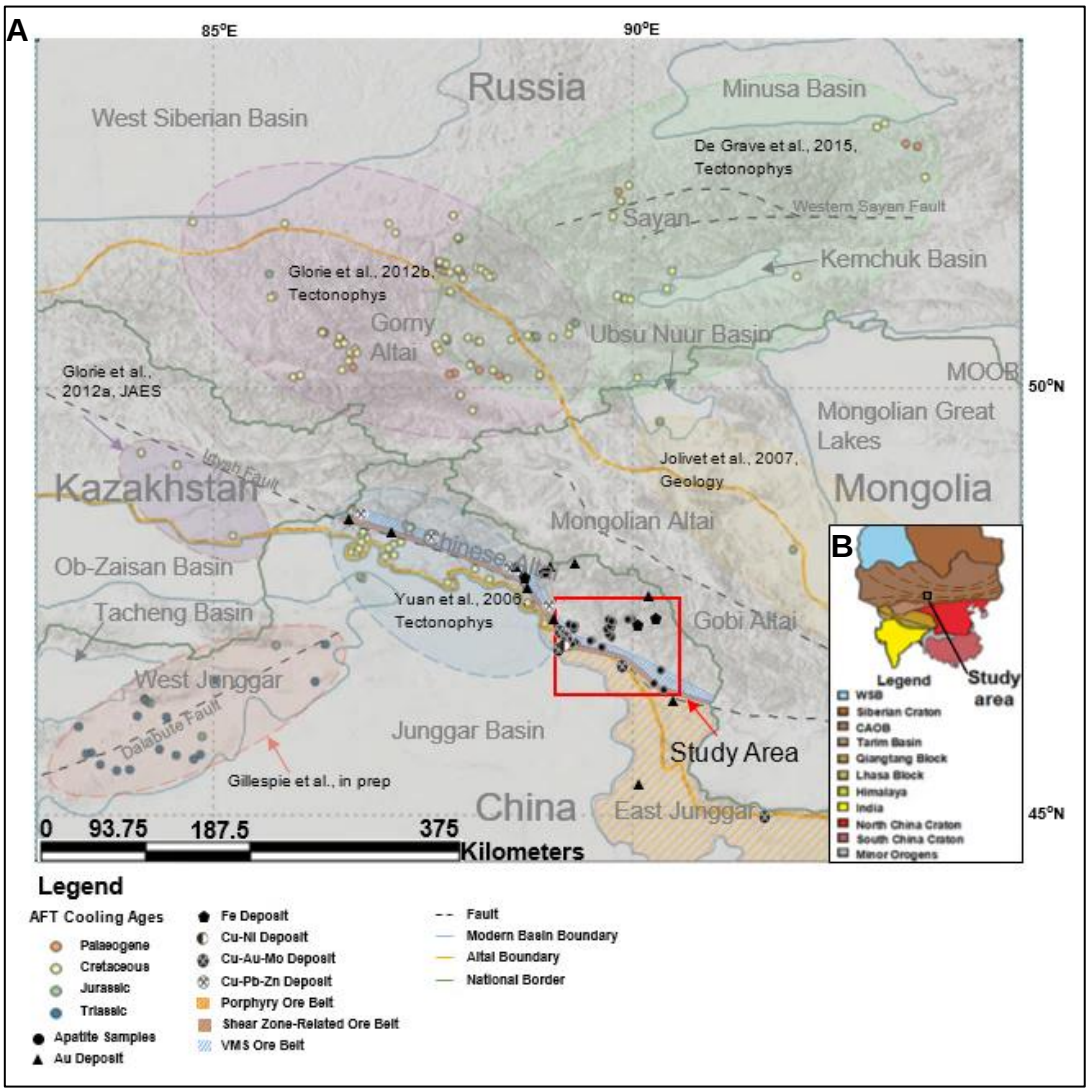

Figure 1: Topographic map (A) of the Altai mountain range (outlined in gold) and surrounding parts of the CAOB, including modern-day basins (blue-grey coloured line) as well as major fault lines (dashed line). This study area is situated in the Chinese Altai, near East Junggar in NE China (red square) and near the Mongolian NW boundary (national borders outlined in green). Apatite samples (black dots) are shown in the outlined study area. Ore belts and ore deposits after Wan et al. (2011) and Wan, Zhang, & Xiang, (2010). AFT cooling ages (coloured dots) from previous studies (coloured ellipses) within the region are shown on the map. The insert (B) shows the location of the study area in comparison with basins and continental building blocks that make up modern-day Asia (Tapponnier & Molnar, 1976). The CAOB (light brown) has dashed lines which represent the deformation directions as a result of the oroclinal bending process (Li et al., 2017; Xiao et al., 2015).

2.1.1 THE CENTRAL ASIAN OROGENIC BELT

The CAOB amalgamated during the Neoproterozoic-Late Palaeozoic (Windley et al., 2007) as a result of the final collision and amalgamation of the Siberian, Tarim, Baltic and North China cratons. (Wilhem, Windley, & Stampfli, 2012; Windley et al., 2007; Xiao & Santosh, 2014) The amalgamation of the CAOB was accompanied by extensive magmatism (Jahn, 2004; Jahn, Wu, & Chen, 2000; Li, Wang, Wilde, & Tong, 2013), oroclinal bending (Şengör, Natal'In, & Burtman, 1993; Xiao, Huang, Han, Sun, & Li, 2010) and the development of strike-slip fault zones (Li, Sun, Rosenbaum, Cai, & Yu, 2015). Throughout the Meso-Cenozoic, reactivation of the CAOB occurred in response to the stress from regional intracontinental tectonic activity (e.g. De Grave et al., 2007; De Grave, De Pelsmaeker, Zhimulev, Glorie, & Buslov, 2014). The timeline of regional tectonic events that affect the CAOB has been intensively studied with low-temperature thermochronology (e.g. De Grave et al., 2014; Glorie & De Grave, 2016; Glorie, De Grave, Buslov, et al., 2012).

2.1.2 DISTANT TECTONIC EVENTS

During the Mesozoic, multiple Cimmerian blocks collided with Eurasia whilst the Palaeo-Tethys Ocean was being consumed by progressive subduction (Glorie, De Grave, Delvaux, et al., 2012). Cimmerian blocks such as the Lhasa and Qiangtang Blocks collided with the Southern Eurasian continent resultant of subduction zone driving forces (Kapp, DeCelles, Gehrels, Heizler, & Ding, 2007; Otto, 1997; Schwab et al., 2004; Yin & Harrison, 2000). It is thought that these accretion-collision events caused successive reactivation events at the margins of the Eurasian continent (Glorie, De Grave, Delvaux, et al., 2012) and throughout the CAOB (De Grave et al., 2007). A brief period of back-arc extension due to slab roll-back in the Tethys Ocean has been postulated at the end of the Early Cretaceous (Li et al., 2017; Zahirovic et al., 2016).

The MOOB was formed in north-eastern Siberia due to the closure of the ocean between Mongolia-North China and Siberia (Jolivet et al., 2009; Metelkin, Vernikovsky, & Kazansky, 2012; Metelkin et al., 2010). The closure of this ocean has been suggested to have occurred during the Late Jurassic-Early Cretaceous based on the reconstructed localities from a proposed closure model by Metelkin et al. (2012).

Continued subduction of the Neo-Tethys eventually resulted in the Indian-Eurasian continent-continent collision (De Grave, Buslov, & Van den haute, 2007). This collision caused crustal thickening in the Tibetan Plateau and the Himalayan orogeny as well as leading to a far field reactivation of the CAOB. The timing of the collision of the India-Eurasia collision is still debated. A two stage collision model has been suggested by Van Hinsbergen et al. (2012) whom believes that the collision between India and Eurasia increased in intensity and has transitioned from a 'soft' collision ~ 50 Ma to a 'hard' collision ~25 Ma.

In order to translate the thermal history of the study area to the exhumation history, the sedimentation history of adjacent basins needs to be evaluated. Since exhumation is known to cause cooling and erosion, if nearby basins contain sediments with ages that coincide with the recorded cooling models, a relationship can be suggested between the cooling and exhumation histories (e.g. Glorie and De Grave., 2016). Below is a summary for the prominent basins.

2.1.3 SEDIMENTARY HISTORY

The Junggar basin resides along the southern edge of the ISZ and is a large pull-apart intracontinental basin which was created in response to sinistral displacements in the Late Permian-Early Triassic (Allen & Natal'in, 1995; Glorie, De Grave, Delvaux, et al., 2012). Regional convergence initiated local thrusting and deformation which drove uplift and

subsequent erosion leading to the deposition of sediment in the basin. Over the Mesozoic and Cenozoic, the Junggar Basin accumulated 5 km of terrestrial sediments. Weifeng and Yequan (2004) suggest that throughout the Mesozoic, the accumulated sediments in the Junggar Basin transitioned between debris flows, alluvial fans, braided rivers and lacustrine environments in response to uplift and erosion of surrounding regions as a result of the collision between Cimmerian blocks (Lhasa and Qiangtang) and the Eurasian margin.

The Ob-Zaisan Basin makes up the north-western part of the Junggar Basin along the Chinese-Kazakh border (Figure 1). Up to 6 km of Mesozoic and Cenozoic clastic sediment is recorded in the Ob-Zaisan Basin which has been linked to the adjacent eroding Altai orogeny (Thomas et al., 2002).

The WSB is a large flatland which stretches between the Siberian Craton (East) to the Ural Mountains (West) (Figure 1). Similar to the Junggar and Ob-Zaisan basins, the WSB contains Mesozoic and Cenozoic clastic sediments which were deposited as the lower unit of three megacycles of sedimentary deposition between the Triassic and Quaternary (Peterson & Clarke, 1991). Between the Late Permian and Early Triassic, asymmetric horsts and grabens were created across the basin as a repercussion of regional extension. The grabens are partially made up of basalt which is overlaid by ~3 km of Triassic aged continental sedimentary cover (Saunders et al., 2005). These sediments are suggested to have been eroded from a Late Triassic aged Siberian Altai-Sayan orogen (Davies, Allen, Buslov, & Safonova, 2010; Glorie & De Grave, 2016; Le Heron, Buslov, Davies, Richards, & Safonova, 2008).

2.1.4 STRUCTURAL ARCHITECTURE

There is little published data on the reactivation history of the shear zones in the study area. The Tuerhongshate Shear Zone (north) runs parallel to the ISZ (south) in a NW-SE orientation. To the north, separating the ISZ from the Altai formation is the Fuyun-Xibodu Fault (Figure 2). South of the ISZ, the Irtysh Fault runs in a similar orientation and is offset by the NNW-SSE orientated Fuyun Fault under cover.

Along the Irtysh Fault in Kazakhstan, Glorie, De Grave, Delvaux, et al. (2012) reported Cretaceous AFT ages, which record rapid cooling at that time and were interpreted to be related to fault reactivation resultant of far-field effects of the MOOB formation.

This study is situated near the ISZ in the vicinity of the Irtysh and Fuyun fault intersection (Figure 2). This project aims to use AFT and AU-Pb analysis to constrain the reactivation history of the ISZ, to provide an insight into the potential causes of these reactivations and to reconstruct the Chinese Altai exhumation history in general.

2.2 Local history

Closure of the Ob-Zaisan Ocean between West Junggar and the Chinese Altai, began in the Late Carboniferous and caused subsequent arc-continent collision. This occurred along the ISZ which was subject to three deformation stages (D1:D3) (Li, Sun, et al., 2015). The collision was characterised by initial crustal thickening at ~323-295 Ma (D1), orogeny-parallel extension at ~295 Ma (D2) and sinistral transpressional deformation at ~286-253 Ma (D3) (Li, Sun, et al., 2015; Li et al., 2017). Based on $^{40}Ar/^{39}Ar$ ages, Li et al. (2017), suggest that oroclinal bending occurred prior to final Ob-Zaisan Ocean closure, driven by slab rollback/trench retreat. The Irtysh Fault was created in response to widespread oroclinal bending, where activation of the ISZ has been dated to ~290-244 Ma in the Chinese Altai

(Briggs et al., 2007; Laurent-Charvet, Charvet, Monié, & Shu, 2003; Li, Yuan, Sun, Long, & Cai, 2015) and ~290-265 Ma in the Kazakhstan segment (Buslov et al., 2004). These ages are suggested to be linked to sinistral shearing and contraction (Laurent-Charvet et al., 2003; Qu, 1991; Qu & Zhang, 1991) in the ISZ deformation history (Li, Sun, et al., 2015). The emplacement of Palaeozoic aged granitoids surrounding the faults is hence considered to be linked to the same tectonic processes and/or the subduction and closure of the Palaeo-Asian Ocean (PAO) (e.g. Windley et al., 2007; Xiao et al., 2018).

Further along the Irtysh fault in Kazakhstan, Glorie, De Grave, Delvaux, et al. (2012) reported ~340-320 Ma zircon ages for the syn- and post-collisional Kalba-Narym intrusives, suggesting that their emplacement occurred during the Siberia-Kazakhstan collision. Latter authors further suggested that the ISZ experienced an 'early brittle' left lateral transtensional stress regime prior to Late Carboniferous–Early Permian intrusion emplacement. Subsequently, the stress regime is suggested to have transitioned to a 'late brittle' regime, which occurred under compression and rheological shortening in response to crustal cooling and ductile shearing (Glorie, De Grave, Delvaux, et al., 2012) in D3 (Li, Yuan, et al., 2015). AFT data and thermal history modelling indicates that the basement rocks from the Kazakhstan section of the ISZ were subjected to Late Cretaceous (~100-70 Ma) cooling (Glorie, De Grave, Delvaux, et al., 2012). This phase of cooling is suggested to have occurred due to increased denudation of the Late Mesozoic Altai orogen, which is possibly linked to far field effects of the MOOB development and subsequent collapse (Glorie, De Grave, Buslov, et al., 2012).

The NNW-SSE orientated Fuyun Fault offsets NW-SE orientated faults in the study area (Figure 2), which suggests this fault has been created at a later stage in respect to the Irtysh Fault. Findings from Lin. (1994) suggest the Fuyun fault was formed in the Cretaceous or

earlier, which is indicated by offset Mesozoic (~80-110 Ma) granite intrusions dated using K-Ar methods.

A period of tectonic quiescence from the Late Mesozoic-Early Cenozoic followed. This interpretation complies with findings from De Grave. (2002) in the Northern Altai and Jolivet et al. (2007) in the Gobi Altai whom both agree on a period of cooling followed by ceased tectonic activity at that time. In both areas there are reported remains of late Mesozoic erosional peneplains in support of this interpretation. A final stage of cooling from ~25 Ma was indicated in some of the thermal history models for the Kazakhstan section of the ISZ (Glorie, De Grave, Delvaux, et al., 2012), which potentially reflects reactivation of the ISZ from the Cenozoic Altai mountain building episode. This Oligocene mountain building episode aligns with a change in the palaeostress field which is characterised by minor transpressional and dextral strike-slip under shallow conditions (Glorie, De Grave, Delvaux, et al., 2012).

In this paper we aim to reconstruct the reactivation history of the Chinese Altai around the Irtysh and Fuyun faults.

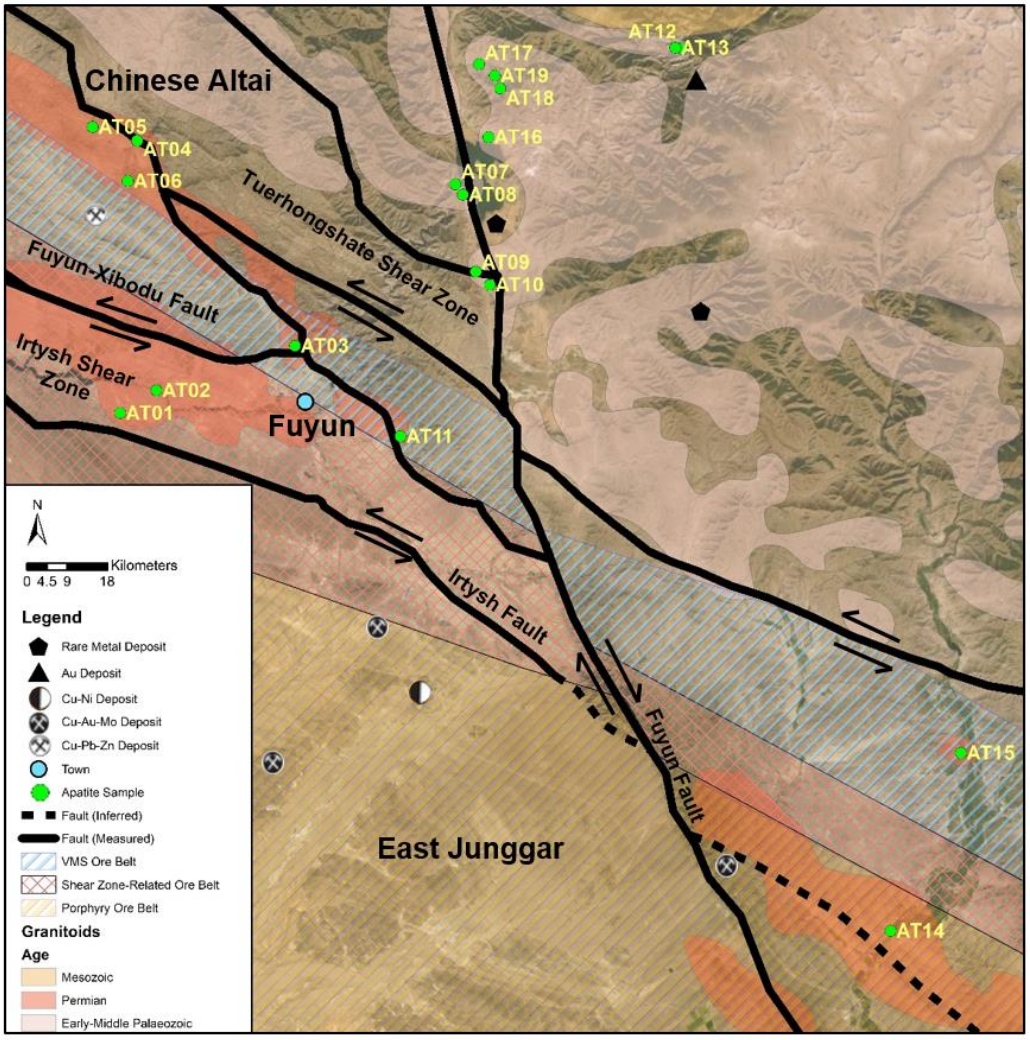

Figure 2 – Topographic map of the study area situated in the Chinese Altai near Fuyun (blue dot). Apatite samples (green dots) were taken throughout the region from Permian and Early-Middle Palaeozoic aged granitoids (Permian granitoids – orange polygons, Early-Middle Palaeozoic granitoids – beige polygons, Mesozoic granitoids – yellow polygon) are plotted after Tong et al. (2014). The Chinese Altai is separated from East Junggar by the Irtysh Fault (measured fault – solid line and inferred fault – dashed line) which divides the mountains from the flat lands. Shear zones and faults after Li, Sun, et al. (2015) are labelled. When vergence directions are known arrows show the offset direction. Ore belts and ore deposits are plotted after Wan et al. (2011) and Wan et al. (2010).

3. METHODS

3.1 Laboratory processing

Granitoid samples were collected in the Chinese Altai by Adelaide Thermochronology Laboratory and Study Group (ATLaS) PhD students (Gilby Jepson & Jack Gillespie) and were prepared by crushing, sieving and mineral separation using standard methods at the Institute of Geology and Geophysics, Chinese Academy of Sciences (IGGCAS). Upon arrival

at the University of Adelaide, apatites were handpicked under a binocular microscope and mounted in EpoxyCure resin on thin sections slides. The apatite grains were then ground and polished to expose the apatites (See Appendix A for complete outline of processing). The samples were then etched in a solution of 5.5M HNO_3 for 20±0.5 seconds at 20±0.5ºC to expose the fission tracks. The fission track density was calculated by counting the number of tracks in a reference grid. The density portrays the fission track age of individual apatite grains as they pass through the 60-120ºC AFT closure temperature (Wagner, Gleadow, & Fitzgerald, 1989). The counting aim was 1000 tracks minimum per sample using 40 grains when possible. Using 1000X magnification, 100 horizontal confined tracks were measured (when sample quality permits) to calculate the cooling rate through the partial annealing zone. Using spot analysis on an Agilent 7900x mass spectrometer and a Resonetics M-50 laser system the uranium concentration and U-Pb concentrations of each grain was measured. Primary standards for U-Pb analysis and data reduction were Madagascar apatite (524.6±3.2 Ma) (Chew, Petrus, & Kamber, 2014), Durango apatite (31.44±0.18 Ma) (McDowell, McIntosh, & Farley, 2005) and McClure apatite (524.6±3.2 Ma) (Chew et al., 2014). Reference material were used as secondary standards to ensure accuracy (Chew et al., 2014). NIST 610 was used as primary standard for trace element concentration calculations with ^{43}Ca as internal standard. Durango was used as primary standard for Cl concentration calculations (Chew, Donelick, Donelick, Kamber, & Stock, 2014). Additional analytical details can be found in Table 1.

3.2 Apatite fission track analysis

Using low-T thermochronology techniques such as AFT we can reconstruct the thermal history preserved in apatite grains. The thermal history recorded within the apatite grains record the cooling time and rate through the apatite partial annealing zone (APAZ). As the

samples pass through the APAZ (60-120 ^{o}C), fission tracks, which form by the spontaneous fission of ^{238}U (Wagner et al., 1989) are annealed and decrease in length and area density (Gleadow, Duddy, Green, & Lovering, 1986). The extent of the annealing process is controlled by a proportional relationship to the rate and timing of cooling (Chew & Spikings, 2015; Wagner et al., 1989). This implies that a population of long fission tracks indicates apatites spent a short time in the APAZ and were thus subject to a fast cooling rate (Gleadow, Duddy, Green, & Hegarty, 1986).

The age of samples were depicted by using AFT ages from individual apatite grains calculated by RadialPlotter software (Vermeesch, 2009, 2017). Samples with a chi-squared (χ^2) passing result of >0.05 (O'Sullivan & Parrish, 1995) and a single-grain age dispersion of <25% are considered as recording a single AFT population. In contrary, samples that do not pass the χ^2 test or show a single-grain dispersion of >25% are thought to contain apatite grains which show heterogeneity (Galbraith & Laslett, 1993) and thus potentially contain multiple ages. For samples with this complication, RadialPlotter's 'Automatic Mixture Model' function was used which allowed us to statistically define the various age populations. Variations in age populations are often correlated to variations in chemical composition of the apatites. High concentrations of Cl within apatite are suggested to have reducing effects on fission track annealing (Green, Duddy, Gleadow, Tingate, & Laslett, 1986), whilst (Hendriks & Redfield, 2005) propose that U enhances fission track annealing. Therefore, apatite grains of different chemical signatures potentially reflect variations of annealing rates within the sample. The chemical signature of apatite (Cl in this study) was introduced in the subsequent thermal history modelling as a kinetic parameter.

3.3 Low-temperature thermal history modelling

Using AFT ages from individual grains and confined track lengths, thermal history models were constructed using the QTQt software (Gallagher, 2012). Other constraints including crystallisation age and AU-Pb age were used to assist with the thermal modelling. Samples were constrained to a present day temperature range of 25±5^{o}C, with all granite samples modelled using their AU-Pb age or a fixed crystallisation temperature of 475±75^{o}C when AU-Pb data was unavailable.

To test the plausibility of each model, the modelling procedure involved running a short test of 10,000 models. It was deemed plausible if the software produced a model that corresponded to the AFT age of the sample. If the sample passed, then the procedure was ran to create 200,000 models to show the “expected" thermal history.

Table 1 - Analytical details of the LA-ICP-MS as calibrated for AFT and AU-Pb dating.

Laser	
Type	Excimer Laser
Brand and Model	Resonetics M-50-LR
Wavelength	193 nm
Pulse Duration	20 ns
Spot Size	29 um
Repetition Rate	5 Hz
Laser Fluence	~3.5 J/cm2
ICP-MS	
Brand and Model	Agilent 7700s
Forward Power	1300 W
Torch Depth	4.5 mm
Gas Flow (L min-1)	
Cool (Ar)	15
Auxiliary (Ar)	0.89
Carrier (He)	0.7
Sample (Ar)	0.93
Data Acquisition Parameters	
Data Acquisition Protocol	Time-resolved analysis
Scanned Masses	^{29}Si, ^{35}Cl, ^{43}Ca, ^{55}Mn, ^{88}Sr, ^{89}Y, ^{202}Hg, ^{204}Pb, ^{206}Pb, ^{207}Pb, ^{208}Pb, ^{232}U, ^{238}U
Detector Mode	Pulse counting
Background Collection	15 seconds
Ablation for Age Calculation	30 seconds
Washout	15 seconds
Standards	
Primary Standards	NIST610, Madagascar Apatite
Secondary Standards	Durango Apatite, McClure Mountain Apatite

4. RESULTS

4.1 Samples

Table 2 – Sample locations, lithology details and crystallisation ages from maps and/or previous studies* from Tong et al. (2014) and references therein.

Sample	Latitude (N)	Longitude (E)	Altitude (m)	Lithology	Crystallisation Ages (Ma)
AT-01	89.2915450	46.9859290	844	Granitoid	Permian ZU-Pb - 283±4*
AT-02	89.3367110	47.0050070	752	Granitoid	Permian ZU-Pb - 283±4*
AT-03	89.5093370	47.0430060	1107	Granitoid	Permian
AT-04	89.3126140	47.2170490	1029	Granitoid	Permian
AT-05	89.2570740	47.2287260	1089	Granitoid	Permian
AT-06	89.3010040	47.1828220	1011	Granitoid	Permian
AT-07	89.7093220	47.1801010	1167	Granitoid	Early-Middle Palaeozoic
AT-08	89.7186900	47.1713970	1286	Granitoid	Early-Middle Palaeozoic
AT-09	89.7347740	47.1058730	1332	Granitoid	Early-Middle Palaeozoic
AT-10	89.7522010	47.0947160	1257	Granitoid	Early-Middle Palaeozoic
AT-11	89.6410000	46.9660000	1020	Granitoid	Permian ZU-Pb - 257±5*
AT-12	89.9923840	47.2948360	1769	Granitoid	Early-Middle Palaeozoic
AT-13	89.9834130	47.2956780	1565	Granitoid	Early-Middle Palaeozoic
AT-14	90.2519410	46.5433950	1173	Granitoid	Permian ZU-Pb - 283±4*
AT-15	90.3396450	46.6958420	1298	Granitoid	Permian
AT-16	89.7506580	47.2201040	1167	Granitoid	Early-Middle Palaeozoic
AT-17	89.7388830	47.2818940	1457	Granitoid	Early-Middle Palaeozoic
AT-18	89.7654070	47.2613040	1996	Granitoid	Early-Middle Palaeozoic
AT-19	89.7584150	47.2721780	1740	Granitoid	Early-Middle Palaeozoic

Nineteen samples were collected (Figure 2) and analysed using the AFT and AU-Pb methods.

Three samples were excluded from both methods due to their absence of apatite (samples 6, 7

and 12) with a further two samples left out from AU-Pb methods (samples 5 and 9) due to an insufficient number of grains for a reliable age regression. NW-SE running shear zones (e.g. ISZ) and faults (e.g. Fuyun-Xibodu Fault) as well as a NNW-SSE running fault, the Fuyun Fault, were targeted to constrain the reactivation history of the Chinese Altai structural architecture. Nine samples were collected from Permian aged granitoids (Table 2), which coincide with the locality of the ore belts that run through the NE-SW part of the study area (Figure 2). The remaining 10 samples were collected from Early-Middle Palaeozoic aged granitoids that are located geographically north of the ore belts and to the NE of the Tuerhongshate Shear Zone. To the far north of the study area, a Mesozoic aged granitoid is the youngest emplaced intrusion.

AT-01 and AT-02 were sourced in the ISZ nearby to the Fuyun Migmatite Permian granitoid, which yields a zircon uranium-lead (ZU-Pb) age of 283±4 Ma (Zhang et al., 2012). AT-11 was sourced along an unnamed fault near the Wugiagou (ZU-Pb 257±5 Ma) Permian granitoid (Chen & Han, 2006). AT-14 was sourced down in the SE of the study area, slightly north of the Irtysh Fault and nearby to the Mayin'ebo (ZU-Pb 283±4 Ma) Permian granitoid (Zhou et al., 2007). The other 16 samples are from areas with unknown ages. Samples have been placed in two groups based on their geographic proximity to each other and AFT age similarities (Figure 3).

- Group 1, west of Fuyun Fault, consists of eleven samples AT-01, AT-02, AT-03, AT-04, AT-05, AT-06, AT-07, AT-08, AT-09, AT-10 and AT-11 which are sourced from Permian and Early-Middle Palaeozoic granitoids. These samples were collected in the vicinity of shear zones and minor faults in the NW of the study area and are located on the western side of the Fuyun Fault (Figure 3).
- Group 2, east of Fuyun Fault, consists of eight samples AT-12, AT-13, AT-14, AT-15, AT-16, AT-17, At-18 and AT-19. These samples predominantly occupy the northern part

of the study area and were sourced from Early-Middle Palaeozoic granitoids; however, in addition, Group 2 also includes AT-14 and AT-15 from Permian granitoids in the far SE corner of the study area (Figure 3).

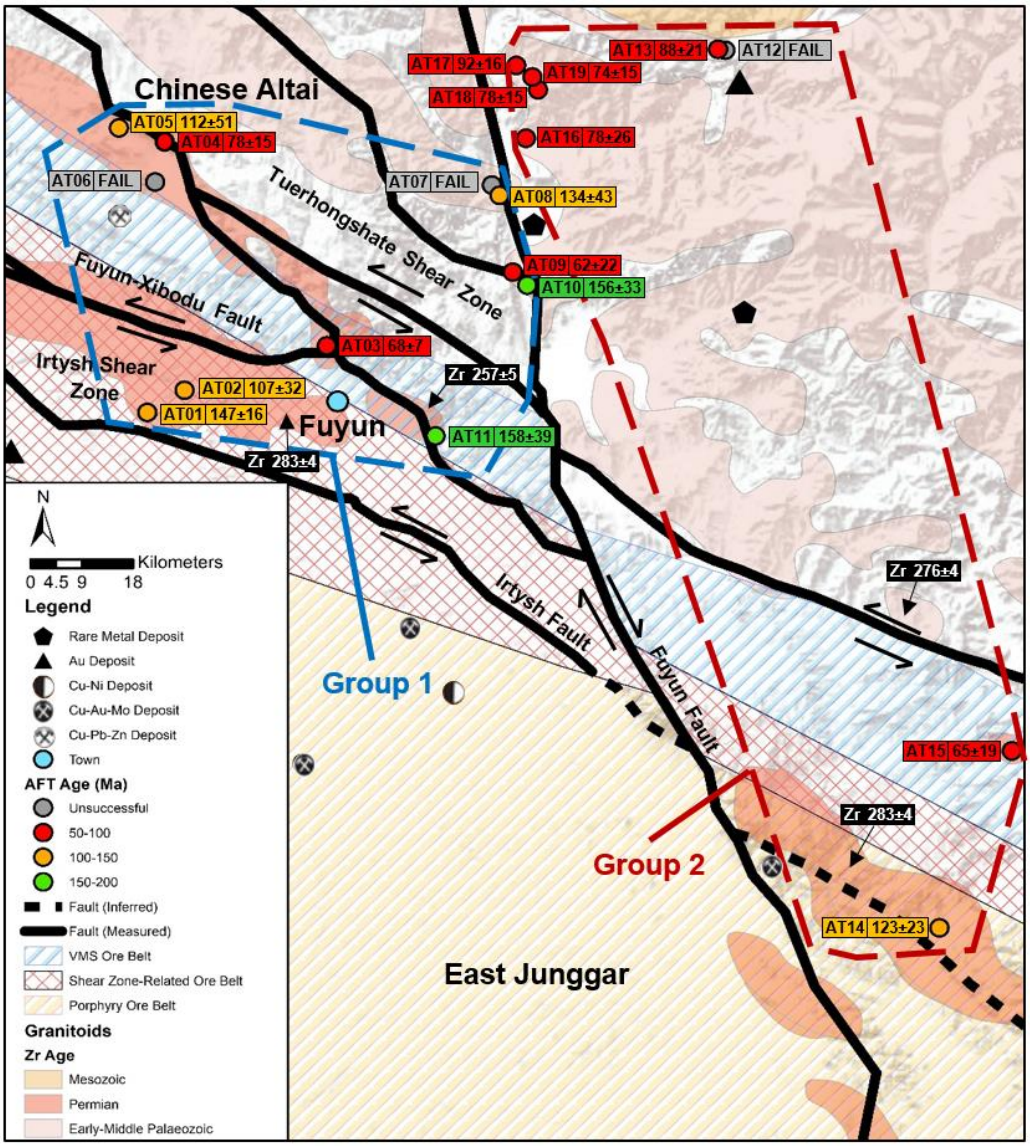

Figure 3 - Topographic map wither superimposed geology of the study area situated in the Chinese Altai near Fuyun (blue dot). The two groups of samples are outlined by dashed polygons (blue = group 1, red = group 2) sample symbols are coloured following their AFT age (red – 50-100 Ma, orange – 100-150 Ma, green – 150-200 Ma and grey – failed sample). Their numeric age and error as calculated by the RadialPlotter software (Vermeesch, 2009) is included in the box alongside at the sample ID. ZU-Pb ages for granitoids with known ages are displayed in black boxes with white print with arrows pointing to the dated source. Shear zones and known faults after Li, Sun, et al. (2015) are labelled, additionally when strike-slip displacement is known arrows show the offset direction. Ore belts and ore deposits after Wan et al. (2011) and Wan et al. (2010).

4.2 Apatite fission track results

Table 3– Summary table showing AFT data per sample group. ps represents the average density of spontaneous fission tracks. Ns represents the number of tracks counted across all analysed grains of the specified sample. ^{35}Cl and ^{238}U represent the median elemental concentrations of the analysed grains with 1σ reporting the median analytical uncertainty. t represents the central AFT age as calculated by the RadialPlotter software (Vermeesch, 2009) with 2σ reporting the uncertainty. nl represents the total number of measured confined tracks from the specified sample. MTL represents the mean track length of all the confined fission tracks measured in the sample with SD as the 1σ standard deviation of the distribution. Disp represents the level of dispersion amongst the single-grain AFT ages with $P(\chi^2)$ representing the probability at which the analysed grains are of a single population. Disp and $P(\chi^2)$ were calculated with RadialPlotter. Dashes indicate insufficient data. Further AFT data can be found in Appendix B.

Sample	ρs ($x10^5/cm^2$)	Ns	n	^{35}Cl (ppm)	1σ (ppm)	^{238}U (ppm)	1σ (ppm)	t (Ma)	2σ (Ma)	nl	MTL (μm)	SD (μm)	Disp (%)	$P(\chi^2)$
Group 1 samples, west of Fuyun Fault														
AT-01	75.30	322	3	620.00	210	97.90	2.30	147.36	16.21	71	11.96	1.76	0	0.5
AT-02	24.08	868	18	555.00	235.00	49.75	1.60	106.6	32.4	100	11.97	2.08	63.7	0
AT-03	30.32	701	15	2300.00	280.00	79.80	1.60	68.34	6.54	100	12.47	1.79	11.8	0.04
AT-04	17.78	954	19	1070.00	280.00	46.00	1.20	78.34	14.97	100	12.35	1.48	24.8	0
AT-05	16.79	44	2	615.00	175.00	28.36	0.55	112.5	51.2	27	10.95	1.87	0	0.03
AT-06														
AT-07														
AT-08	3.80	37	6	580.00	230.00	5.07	0.21	133.6	43.2	72	11.29	1.76	0	0.32
AT-09	9.34	30	3	1000.00	190.00	28.28	0.65	61.9	22.2	68	11.15	1.77	0	0.85
AT-10	7.73	89	7	720.00	200.00	10.99	0.50	156.3	32.6	9	12.62	1.22	0	0.48
AT-11	10.04	236	14	490.00	200.00	12.26	0.38	158.4	39.0	20	11.52	1.54	39.1	0
Group 2 samples, east of Fuyun Fault														
AT-12														
AT-13	15.90	341	15	590.00	230.00	37.10	0.96	88.5	20.8	100	11.76	1.95	40	0
AT-14	5.95	143	11	480.00	170.00	7.11	0.38	122.7	22.6	-	-	-	13.6	0.23
AT-15	24.85	559	13	450.00	200.00	67.00	1.50	65.07	18.56	100	12.75	1.57	49.9	0
AT-16	4.88	59	9	400.00	160.00	9.52	0.38	78.3	26.4	12	11.47	1.46	31.5	0.09
AT-17	3.86	129	16	455.00	140.00	8.28	0.32	91.70	16.41	56	11.87	1.75	8.5	0.58
AT-18	11.50	220	9	390.00	190.00	27.30	0.86	77.56	14.83	27	11.85	1.62	20	0.03
AT-19	11.99	230	9	430.00	160.00	26.46	0.55	74.22	15.30	105	11.91	1.43	22.9	0.01

4.2.1 DATA ACCURACY

Durango apatite was used for zeta calibration (Vermeesch, 2017) of single-grain AFT ages for unknown apatite samples. The weighted average AFT age yielded by Durango apatite in this work was 31.00±3.45 Ma (Figure 4) which is within uncertainty of the published $^{40}Ar/^{39}Ar$ age of 31.44±0.18 Ma (McDowell et al., 2005), thus supporting the reliability of our fission track results.

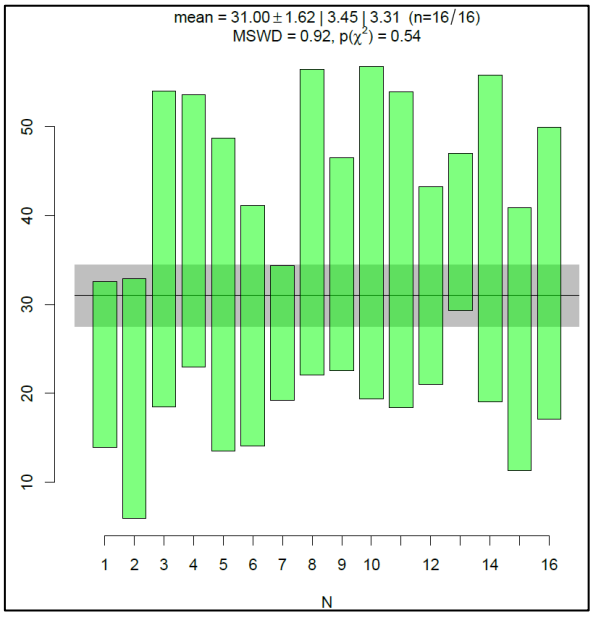

Figure 4 – AFT weighted average age for the analysed primary standard Durango apatite. N (x-axis) represents the number of grains used in the analysis. Y-axis represents the AFT age. MSWD represents the mean square weighted deviation of the AFT data. p(χ^2) represents the probability at which the analysed grains are of a single age population.

4.2.2 GROUP 1 SAMPLES, WEST OF FUYUN FAULT

Group 1 is characterised by the largest variation in AFT age and Cl of the two groups. Group 1 central AFT ages range from 158.4±39 Ma to 61.9±22.2 Ma (Figure 5 A-S). Sample AT-06 and AT-07 failed as they did not contain enough apatite, hence will not be included in further discussion. AT-01, AT-08, AT-09 and AT-10 passed both the χ^2 test and the single-grain age dispersion test which suggests the samples records a single-grain age population. All other samples either had a χ^2 <0.05 and/or a dispersion >25% which potentially suggests the sample has more than one age population. Six of the nine samples in Group 1 had an

abundant amount of confined fission tracks (≥50) while 27, 9 and 20 tracks were measured for AT-05, AT-10 and AT-11 respectively. The combined radial plot for Group 1 gave a central AFT age of 99.63±11.44 Ma with a variation in Cl from ~200 ppm to 120,000 ppm (Figure 5 S).

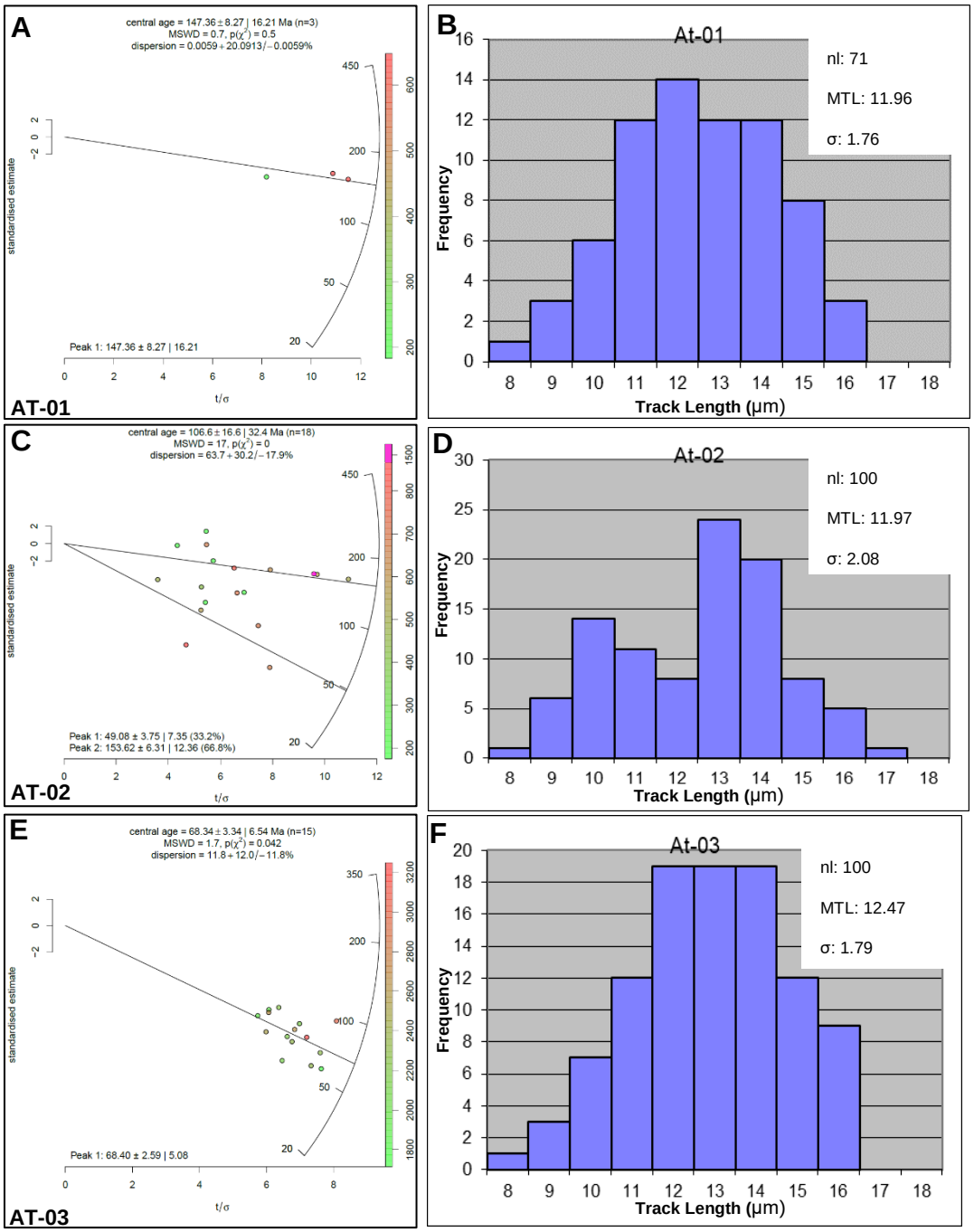

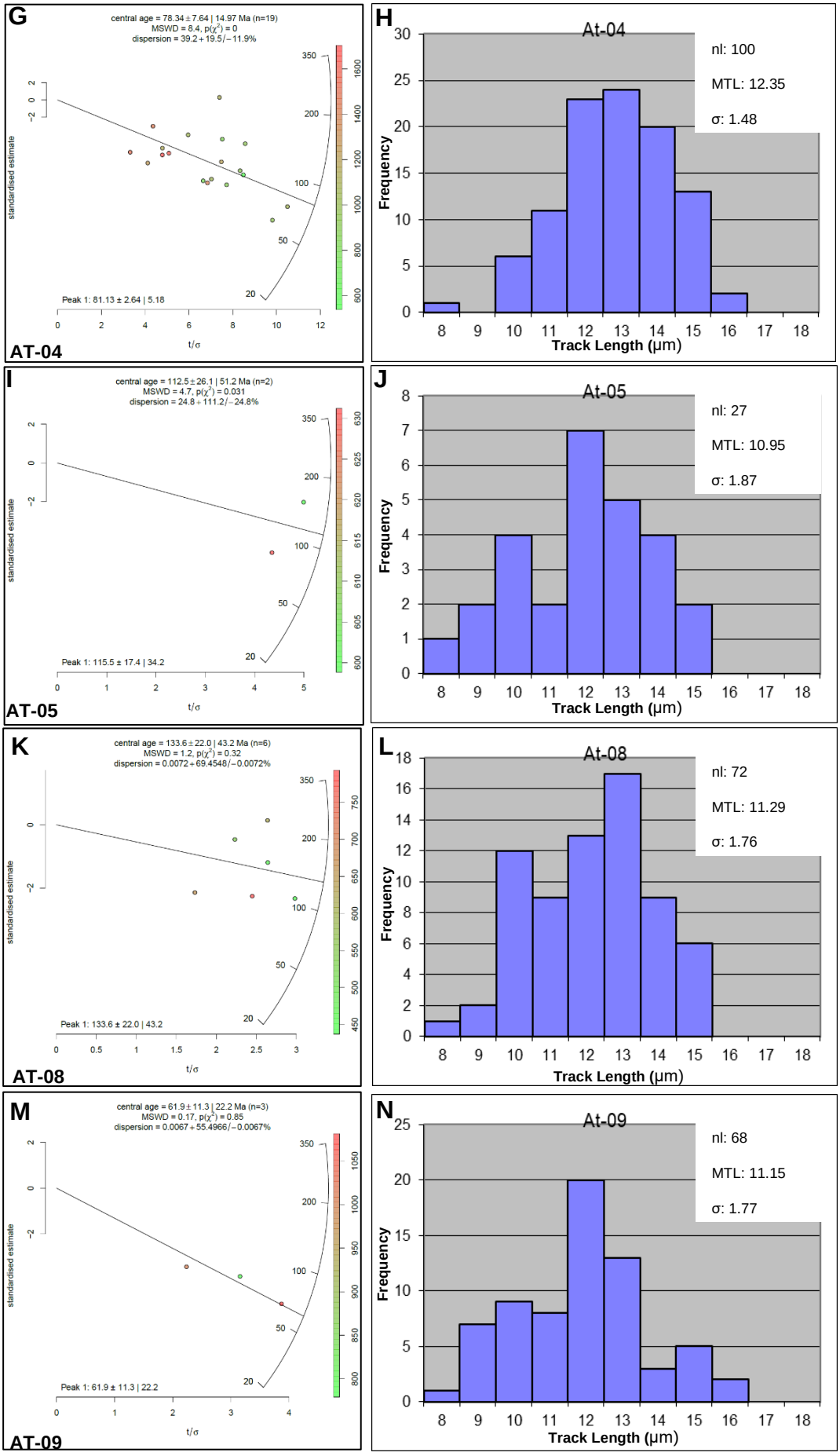
G
central age = 78.34 ± 7.64 | 14.97 Ma (n=19)
MSWD = 8.4, p(χ²) = 0
dispersion = 39.2 + 19.5 / − 11.9%
standardised estimate
Peak 1: 81.13 ± 2.64 | 5.18
t/σ
AT-04
H
At-04
nl: 100
MTL: 12.35
σ: 1.48
Frequency
Track Length (μm)
I
central age = 112.5 ± 26.1 | 51.2 Ma (n=2)
MSWD = 4.7, p(χ²) = 0.031
dispersion = 24.8 + 111.2 / − 24.8%
standardised estimate
Peak 1: 115.5 ± 17.4 | 34.2
t/σ
AT-05
J
At-05
nl: 27
MTL: 10.95
σ: 1.87
Frequency
Track Length (μm)
K
central age = 133.6 ± 22.0 | 43.2 Ma (n=6)
MSWD = 1.2, p(χ²) = 0.32
dispersion = 0.0072 + 69.4548 / − 0.0072%
standardised estimate
Peak 1: 133.6 ± 22.0 | 43.2
t/σ
AT-08
L
At-08
nl: 72
MTL: 11.29
σ: 1.76
Frequency
Track Length (μm)
M
central age = 61.9 ± 11.3 | 22.2 Ma (n=3)
MSWD = 0.17, p(χ²) = 0.85
dispersion = 0.0067 + 55.4966 / − 0.0067%
standardised estimate
Peak 1: 61.9 ± 11.3 | 22.2
t/σ
AT-09
N
At-09
nl: 68
MTL: 11.15
σ: 1.77
Frequency
Track Length (μm)

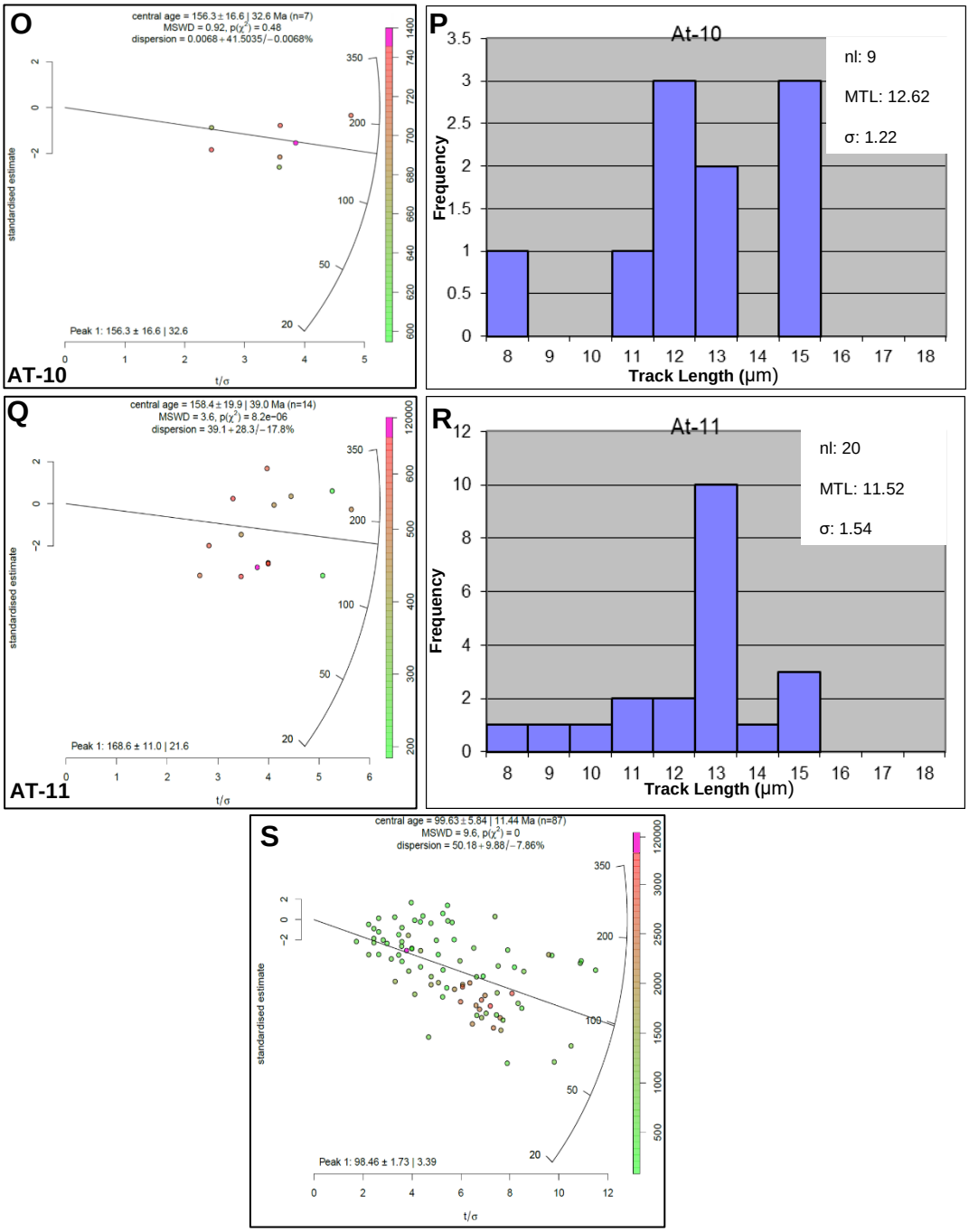

Figure 5 – Radial plots showing calculated AFT central ages and histograms showing the frequency and distribution of MTLs for Group 1 (A-R). A combined radial plot (S) displays all the analysed grains from Group 1. Radial plots and their associated central age values and age-peak discriminations are generated with RadialPlotter software (Vermeesch, 2009). Radial plots with two peaks have the percentage of data associated with each peak bracketed next to the associated age. The x-axis represents the degree of uncertainty which decreases from left to right. The curved y-axis (right) displays AFT age in Ma which increases bottom to top. The straight y-axis (left) represents 2σ from the central age. The coloured scale on the radial plot represents the concentration of Cl in ppm for each grain analysed. In reference to the frequency plots, nl represents the number of confined fission tracks that were measured, MTL – mean track length and σ – standard deviation of the measured lengths. Dashes indicate insufficient data.

4.2.3 GROUP 2 SAMPLES, EAST OF FUYUN FAULT

Group 2 is characterised by the smallest variation of AFT age and Cl of the two groups. Group 2 central AFT ages range from 122.7±22.6 Ma to 65.07±18.56 Ma (Figure 6 A-N). Sample AT-12 failed as the sample didn't contain enough apatite and hence will not be further mentioned in this discussion. AT-14 and AT-17 were the only samples to pass both the χ^2 test and the single-grain age dispersion test which suggests these samples record single-grain age populations. All other samples had a χ^2 <0.05 and a dispersion >25% which may suggest that the samples contain more than one single-grain age population. Four of the seven samples in Group 2 had an abundant amount of confined fission tracks (≥50) while 12 and 27 tracks were measured for AT-16 and AT-18 respectively. AT-14 had ≤5 confined fission tracks and hence isn't mentioned. The combined radial plot for Group 2 gave a central AFT age of 87.79±8.42 Ma (Figure 6 O) with a variation in Cl from ~200 ppm to ~1500 ppm (Figure 6).

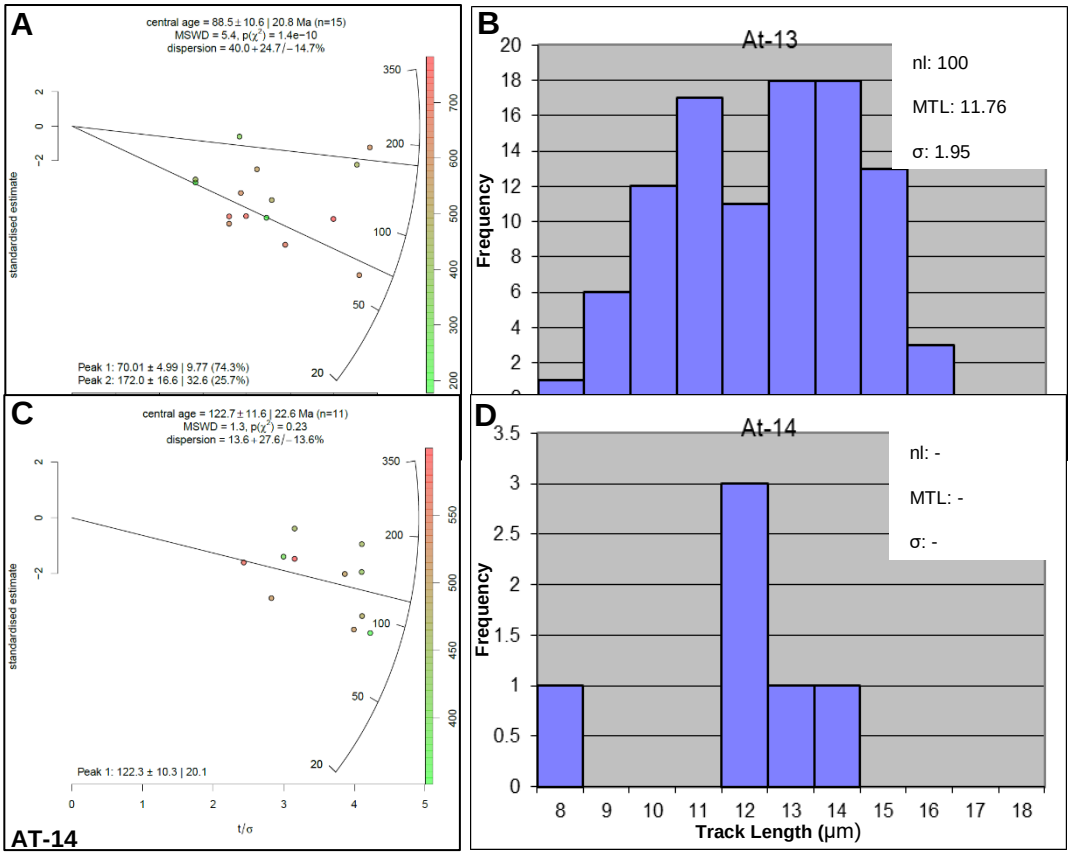

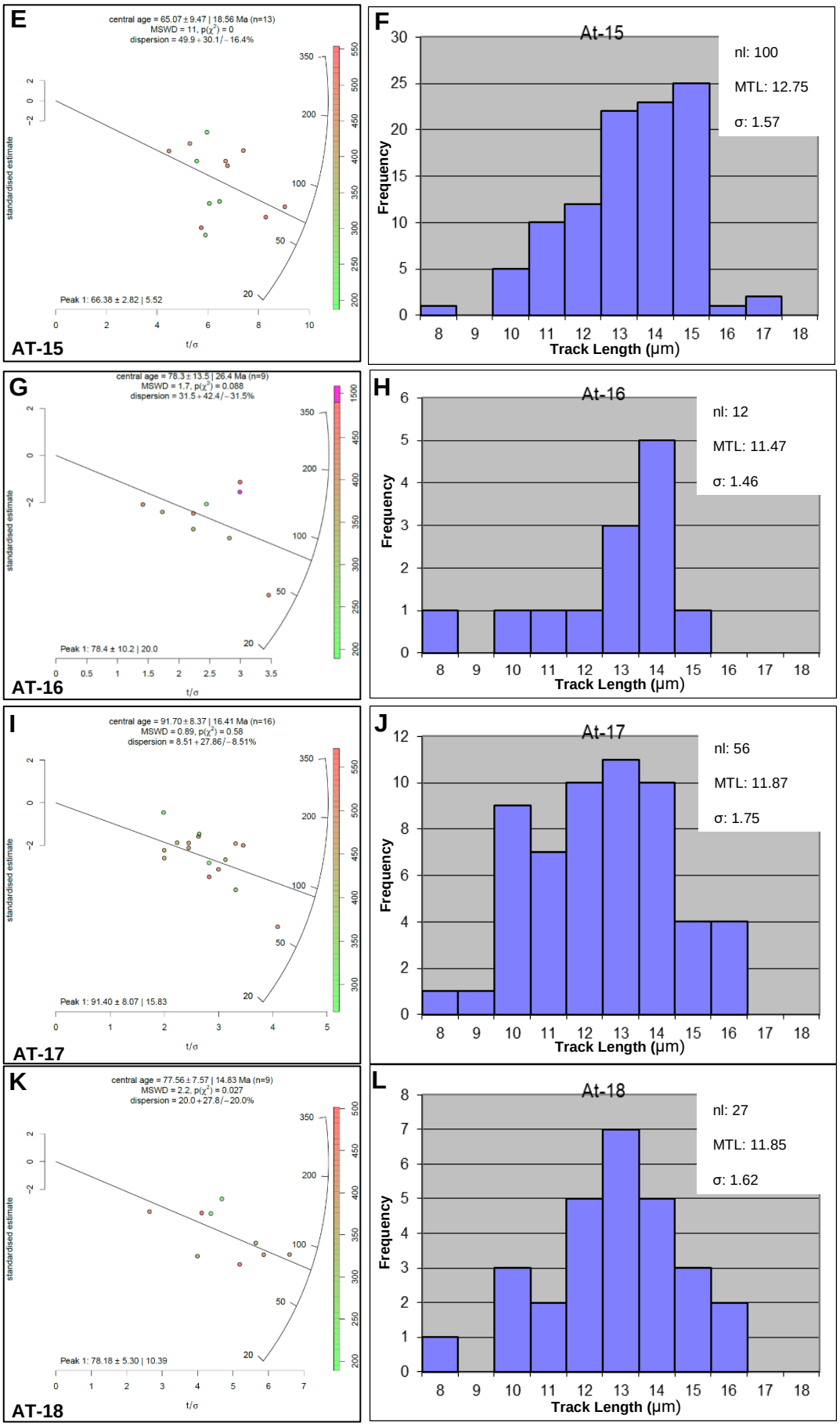
E
central age = 65.07 ± 9.47 | 18.56 Ma (n=13)
MSWD = 11, p(χ²) = 0
dispersion = 49.9 + 30.1/− 16.4%
Peak 1: 66.38 ± 2.82 | 5.52
standardised estimate
t/σ
AT-15
F
At-15
nl: 100
MTL: 12.75
σ: 1.57
Frequency
Track Length (μm)
G
central age = 78.3 ± 13.5 | 26.4 Ma (n=9)
MSWD = 1.7, p(χ²) = 0.088
dispersion = 31.5 + 42.4/− 31.5%
Peak 1: 78.4 ± 10.2 | 20.0
standardised estimate
t/σ
AT-16
H
At-16
nl: 12
MTL: 11.47
σ: 1.46
Frequency
Track Length (μm)
I
central age = 91.70 ± 8.37 | 16.41 Ma (n=16)
MSWD = 0.89, p(χ²) = 0.58
dispersion = 8.51 + 27.86/− 8.51%
Peak 1: 91.40 ± 8.07 | 15.83
standardised estimate
t/σ
AT-17
J
At-17
nl: 56
MTL: 11.87
σ: 1.75
Frequency
Track Length (μm)
K
central age = 77.56 ± 7.57 | 14.83 Ma (n=9)
MSWD = 2.2, p(χ²) = 0.027
dispersion = 20.0 + 27.8/− 20.0%
Peak 1: 78.18 ± 5.30 | 10.39
standardised estimate
t/σ
AT-18
L
At-18
nl: 27
MTL: 11.85
σ: 1.62
Frequency
Track Length (μm)

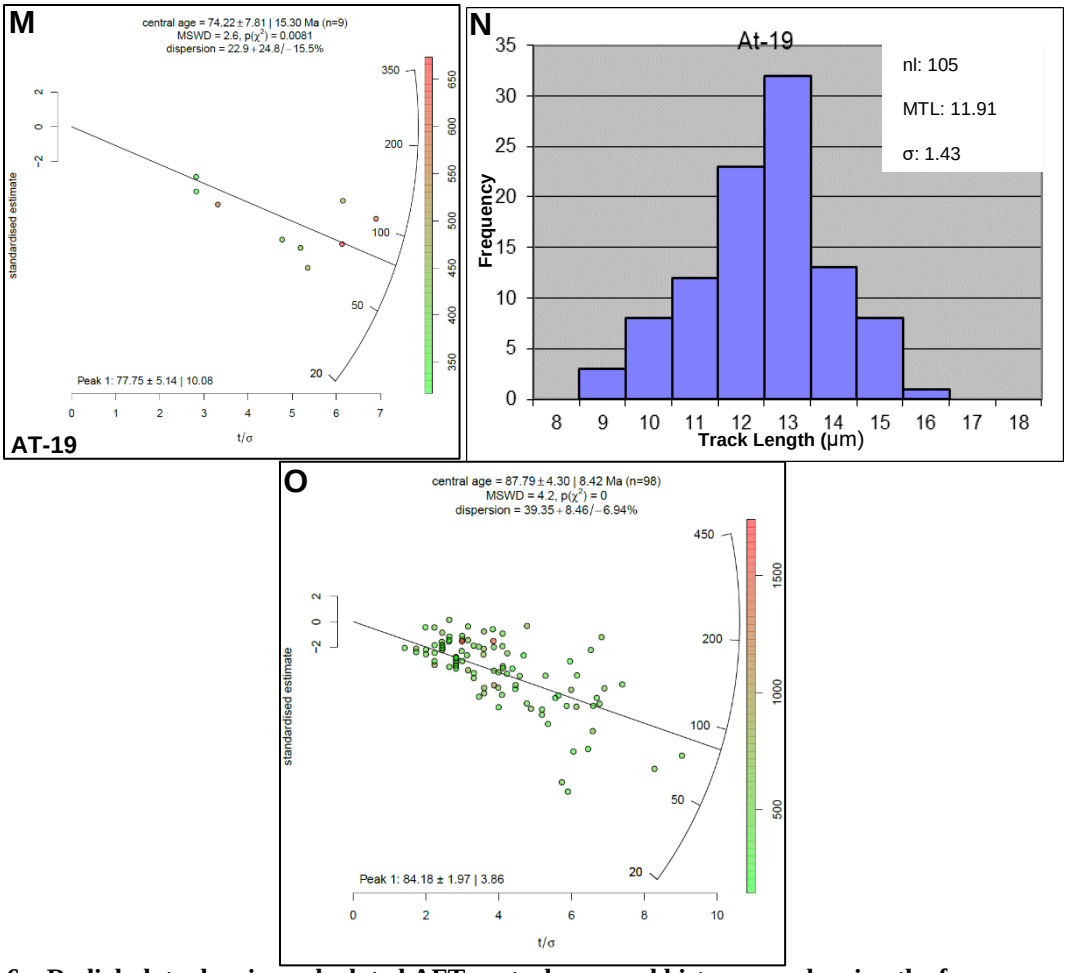

Figure 6 – Radial plots showing calculated AFT central ages and histograms showing the frequency and distribution of MTLs for Group 1 (A-N). A combined radial plot (O) displays all the analysed grains from Group 2 (caption as in Figure 5).

4.2.4 POOLED STUDY AREA

The combined study area samples yield a central AFT age of 91.85±7.19 Ma on the radial plot. Two statistically defined age peaks are present with a P1 AFT age of 66.39±2.76 Ma and a P2 AFT age of 152.16±8.15 Ma (Figure 7), which represent the two AFT data trends. Cl is relatively random across the different aged grains; however, a slight trend indicates the higher Cl concentrations align with P1. This correlation does not comply with the general consensus that grains with higher Cl concentration have a higher closure temperature, preserve longer confined track lengths and hence retain older ages for a given thermal history (Green et al., 1986).

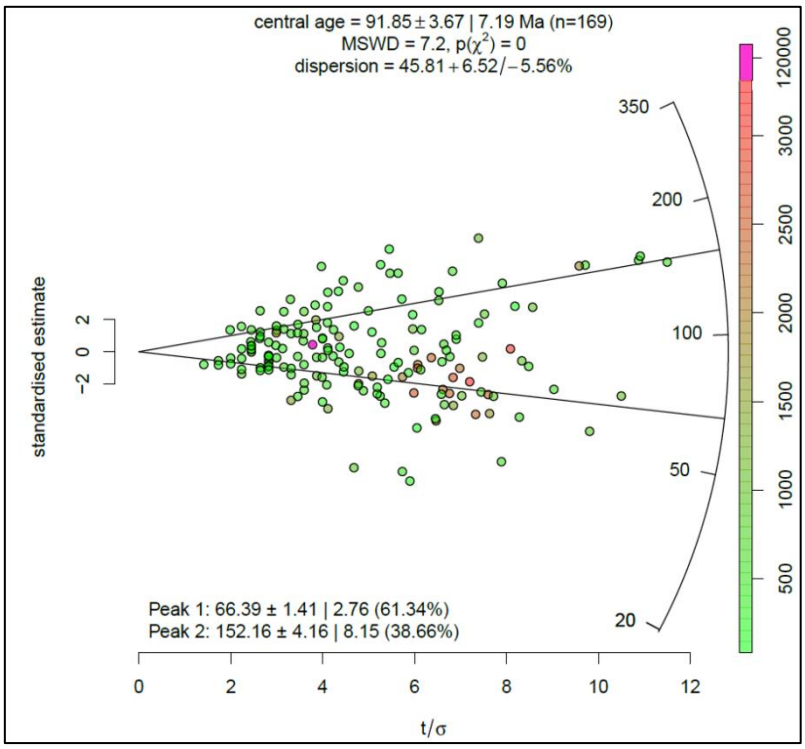

Figure 7 – Radial plot showing the combined single-grain AFT age data throughout the study area (caption as in Figure 5).

4.3 Apatite U-Pb results

Thirteen samples yield meaningful AU-Pb ages, while samples AT-05, AT-08 and AT-09 have a high uncertainty due to the small number of apatite grains. Lower intercept ages range from 153.4±51.7 Ma (Jurassic) to 415±61 Ma (Lower Devonian). The AU-Pb data is compared to central AFT ages and (where available) published ZU-Pb ages (Table 4). Outlier grains that were observed to have down-hole zonation or experienced analytical problems were excluded from the age calculations (Figure 9).

Table 4 - Summary data table showing AU-Pb ages with AFT and ZU-Pb age comparisons organised by ascending sample number. n represents the number of grains used in the AU-Pb analysis. MSWD represents the mean square weighted deviation of the AU-Pb data. The AU-Pb age was calculated by a Tera-Wasserburg Concordia plot where the lower intercept age is used and has a 95% confidence uncertainty. AFT age represents the central AFT age as calculated using RadialPlotter software (Vermeesch, 2009) with 1σ reporting the uncertainty. ZU-Pb age is the crystallisation age from published data as reported by Tong et al. (2014) and references therein. Samples without ZU-Pb ages use mapped ages as reported by Tong et al. (2014) and refer to geological age. Samples shaded in grey failed both AFT and AU-Pb methods. Dashes (-) indicate no data as these samples were non concordant for AU-Pb analysis. Further AU-Pb data can be found in Appendix C.

Sample	Lithology	n	MSWD	AU−Pb Age (Ma)	2σ (Ma)	AFT Age (Ma)	2σ (Ma)	Published ZU−Pb Ages (Ma)
AT-01	Granitoid	4	3.3	262	18	147	16	283±4
AT-02	Granitoid	19	0.78	267	7	107	32	283±4
AT-03	Granitoid	15	0.82	260	11	68	7	Permian
AT-04	Granitoid	20	2.1	240	12	78	15	Permian
AT-05	Granitoid	-	-	-	-	112	51	Permian
AT-06	Granitoid							
AT-07	Granitoid							
AT-08	Granitoid	6	1.7	246	164	134	43	Early-Middle Palaeozoic
AT-09	Granitoid	-	-	-	-	62	22	Early-Middle Palaeozoic
AT-10	Granitoid	6	0.6	415	61	156	33	Early-Middle Palaeozoic
AT-11	Granitoid	14	1.3	254	20	158	39	257±5
AT-12	Granitoid							
AT-13	Granitoid	18	4.1	169	5	88	21	Early-Middle Palaeozoic
AT-14	Granitoid	10	2.1	277	27	123	23	283±4
AT-15	Granitoid	16	3.7	268	7	65	19	Permian
AT-16	Granitoid	9	7.6	170	20	78	26	Early-Middle Palaeozoic
AT-17	Granitoid	16	2.2	153	52	92	16	Early-Middle Palaeozoic
AT-18	Granitoid	9	3.5	201	18	78	15	Early-Middle Palaeozoic
AT-19	Granitoid	10	1.8	175	16	74	15	Early-Middle Palaeozoic

4.3.1 DATA ACCURACY

Durango and McClure apatites were analysed as secondary standards to assess the accuracy of the U-Pb data. Durango apatite yielded a ^{207}Pb weighted average of 30.88±0.82 Ma and McClure apatite yielded an age of 527.74±6.40 Ma (Figure 8). These ages are in agreement with published ^{40}Ar/^{39}Ar ages of 31.44±0.18 Ma (McDowell et al., 2005) and 524.6±3.2 Ma (Chew et al., 2014) respectively; thus, the AU-Pb age data for the analysed unknown samples is deemed reliable.

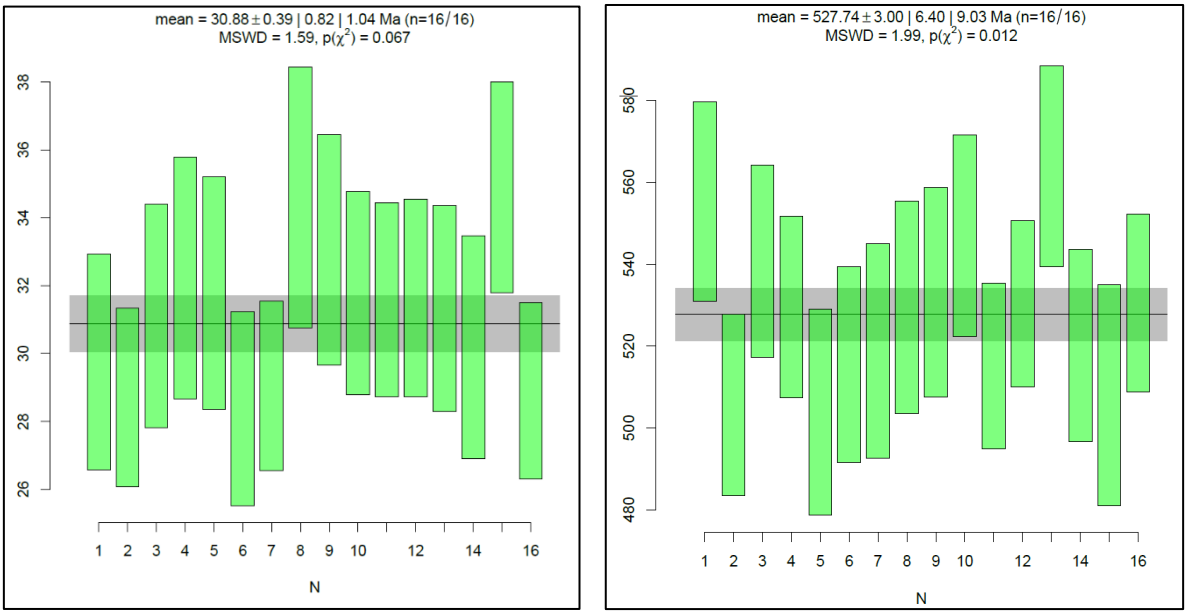

Figure 8 – ^{207}Pb corrected weighted average for ^{206}Pb/^{238}U ages for analysed Durango apatite and McClure apatite standards. n (x-axis) represents the number of grains analysed. Y-axis represents the ^{207}Pb corrected weighted average for the ^{206}Pb/^{238}U ages in Ma.

4.3.2 TERA-WASSERBURG CONCORDIA PLOTS

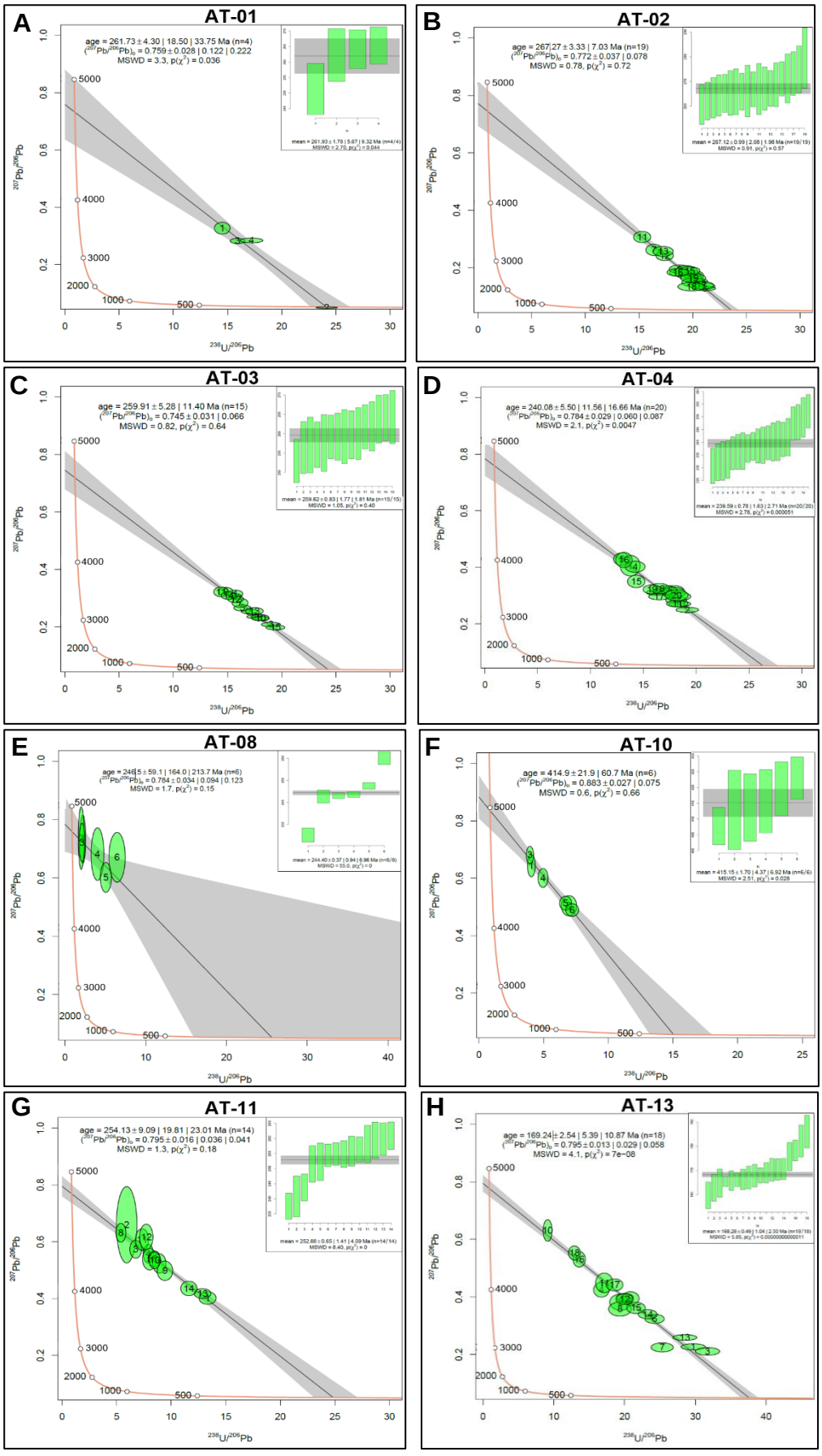

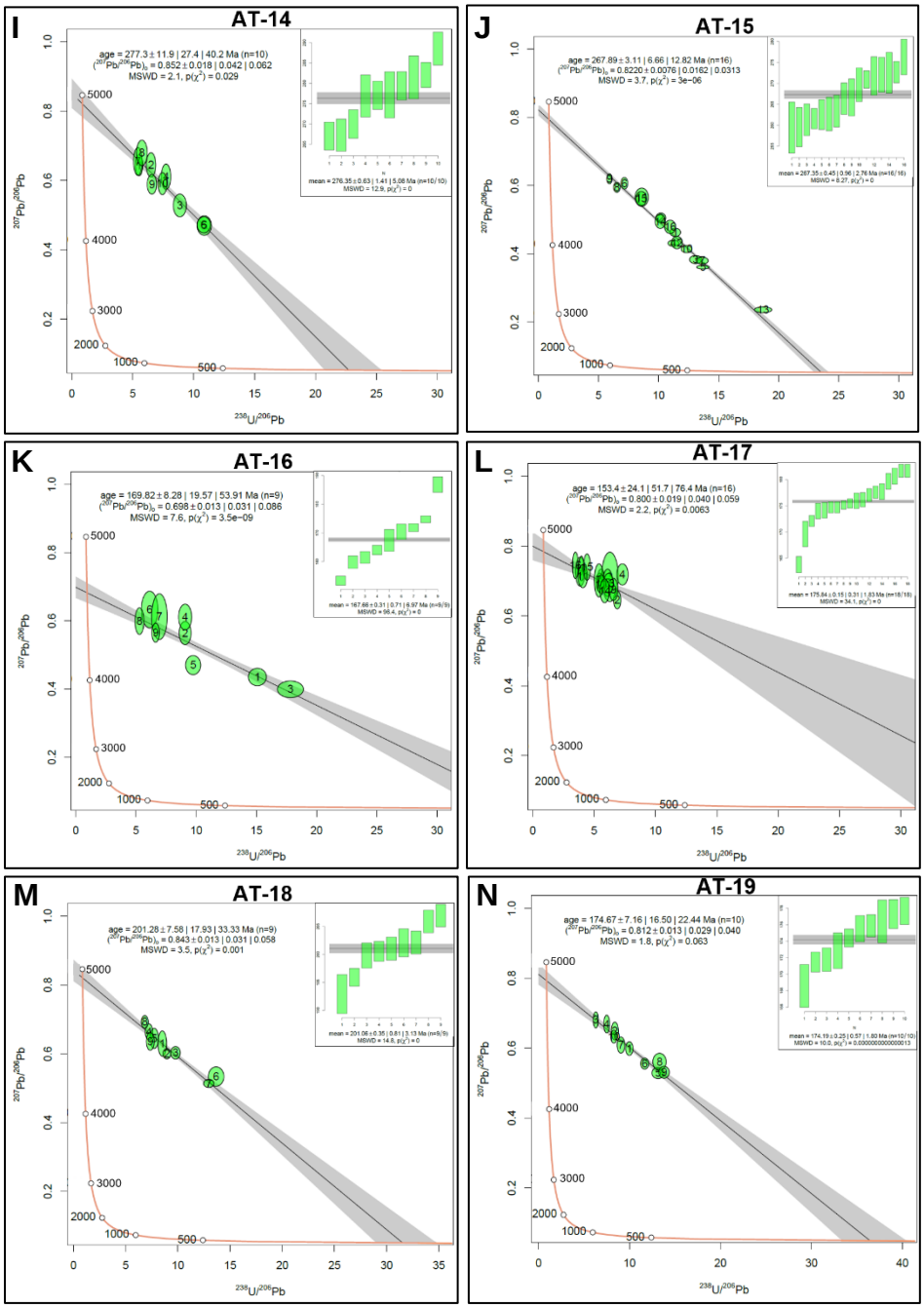

Figure 9 – Terra-Wasserburg Concordia plots for all eligible samples within the study area (A-N). Green ellipses represent each single-grain age which were used to create the common-Pb line. Each ellipse represent a 2σ uncertainty for $^{207}Pb/^{206}Pb$ as well as $^{238}U/^{206}Pb$. Ranked ^{207}Pb corrected weighted average $^{206}Pb/^{238}U$ age plots are inset in the top right corner for each sample.

4.4 Thermal history modelling

"Expected" thermal history models are summarised in Figure 10. Detailed models including individual T(t) plots and prediction histograms can be found in Appendix D.

4.4.1 GROUP 1 SAMPLES, WEST OF FUYUN FAULT

Group 1 samples display a range of models (Figure 10 A). The samples with the oldest AFT ages (AT-01, AT-10 and AT-11) display rapid cooling through the APAZ at ~185-170 Ma. AT-01 leaves the APAZ in the Late Jurassic and remains at upper APAZ (~60 ^{o}C) until the early Palaeogene. AT-10 and AT-11 record similar thermal histories but are poorly constrained. AT-03 and AT-04 cool through the APAZ at a moderate cooling rate (~2.3 ^{o}C/Ma) during the Early Cretaceous. AT-02 records a similar cooling rate, but enters the APAZ earlier at ~120 Ma. AT-05 cooled slowly through the APAZ since ~140 Ma. AT-08, AT-09 and AT-10 record relatively slow cooling through the APAZ since ~145 Ma, ~100 Ma and ~170 Ma respectively. Note the dashed lines in AT-05, AT-10 and AT-11, which represent poorly constrained thermal histories (limited confined length data); therefore, these cooling paths should be treated with caution. In summary, Group 1 samples, taken west of the Fuyun Fault record evidence for rapid cooling at ~180-185 Ma and mostly slow/moderate cooling thereafter. Most samples remained at upper APAZ temperatures (~80-60 ^{o}C) throughout most of the Late Cretaceous-Palaeogene and record a second cooling phase at ~30-15 Ma. The significance of this later cooling phase needs to be interpreted with caution as it may represent a well-documented modelling artefact (e.g. Redfield, 2010).

4.4.2 GROUP 2 SAMPLES, EAST OF FUYUN FAULT

Group 2 samples, taken from the eastern fault block of the Fuyun Fault, record more consistent thermal history models. Rapid cooling through the APAZ is modelled at ~75-115 Ma followed by prolonged residence in the APAZ during the Early Cretaceous-Paleogene. AT-13, AT-17 and AT-19 enter the APAZ at ~115 Ma, ~105 Ma and ~90 Ma and their models suggest a second cooling phases at ~35 Ma, ~30 Ma and ~10 Ma respectively. In summary, Group 2 samples, record evidence for rapid cooling through the APAZ at ~75-115

Ma and subsequent cooling at ~35-10 Ma.

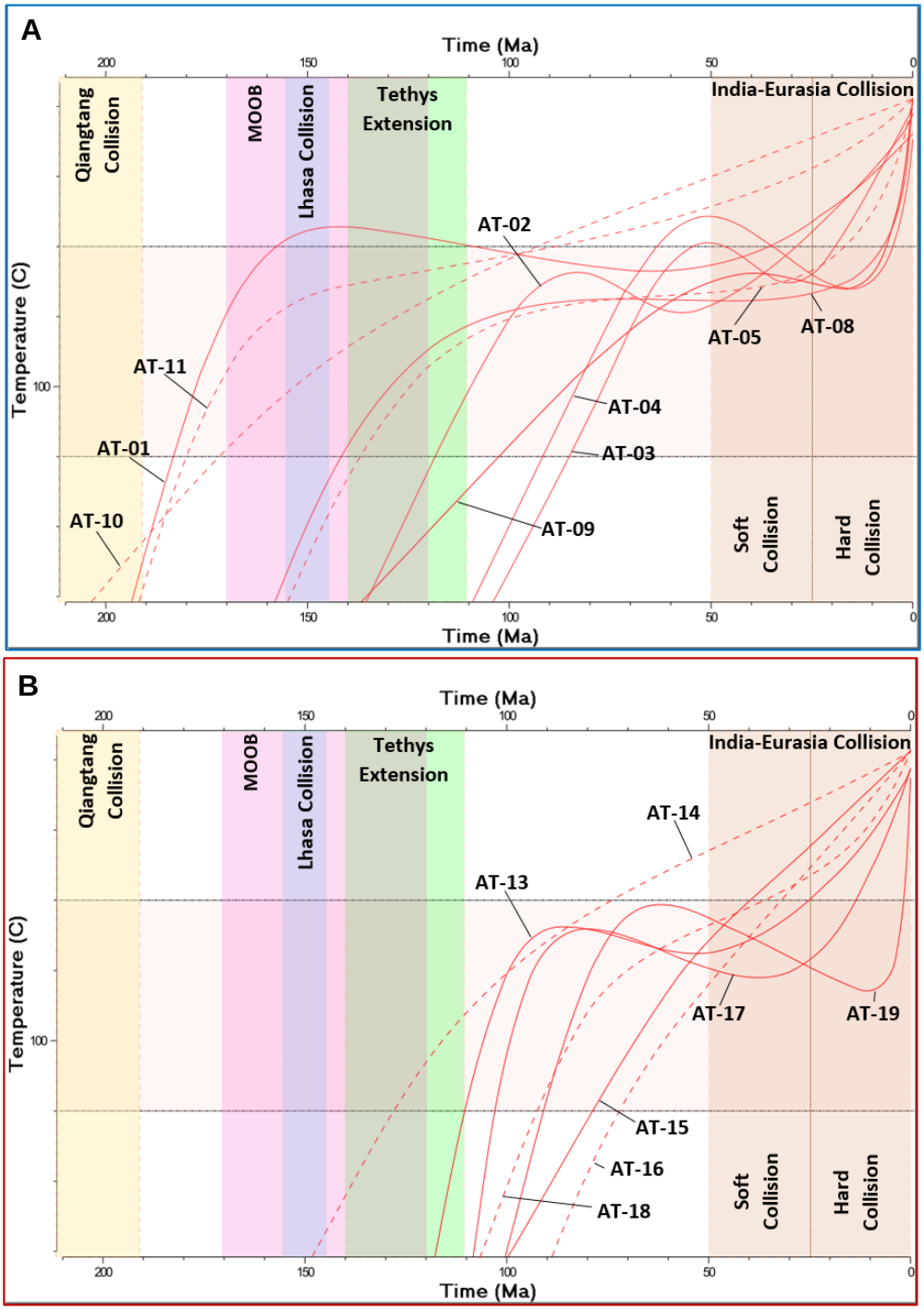

Figure 10 – Combined thermal history models for samples associated with Group 1, west of Fuyun Fault (A - blue) and Group 2, east of Fuyun Fault (B - red). The y-axis represents temperature in degrees Celsius and the x-axis represents time in Ma. The rose coloured zone represents the APAZ between ~60-120 ºC (Wagner et al., 1989). The other coloured zones represent the timing of regional tectonic events. Beige zone = Qiangtang collision (~230-190 Ma), blue zone = Lhasa collision (~155-145 Ma), green zone = Tethys Extension (~140-110 Ma), pink zone = MOOB formation (~170-120 Ma) and brown zone = India-Eurasia collision (~50 Ma-Present) with dotted line representing the change in collision intensity as suggested by Van Hinsbergen et al. (2012). Well-constrained samples with ≥ 50 confined lengths are represented by a solid line. Samples that are poorly-constrained with ≤ 49 confined lengths are represented by a dashed line.

5. DISCUSSION

5.1 AU-Pb age interpretations

Obtained sample AU-Pb dates are compared to ZU-Pb dates to distinguish which samples resemble post-magmatic cooling. ZU-Pb data from Tong et al. (2014) and references therein. When ZU-Pb data is not available, geological mapped crystallisation ages are used (Figures 2 and 3). Samples AT-08, AT-13, AT-16, AT-17, AT-18 and AT-19 were collected from Early-Middle Palaeozoic granitoids and record AU-Pb ages ranging from ~246-153 Ma. As the AU-Pb ages are younger than their corresponding crystallisation ages, they record evidence for thermal cooling after emplacement.

The cluster of Group 2 samples in the north-east of the study area yield Cretaceous-Jurassic ages and were collected from Early-Middle Palaeozoic aged granitoids (Figures 2 and 3). These sampled granitoids are in close proximity to the later emplaced Mesozoic aged granitoids in the far north of the study area. We interpret the age discrepancy between the Early-Middle Palaeozoic emplacement age and the recorded AU-Pb age (for Group 2 samples in the NE) to be resultant of emplacement and related heat of the nearby Mesozoic (80-110 Ma) granitoids (Lin, 1994). We further suggest that these samples were partially thermal reset and hence record an AU-Pb mixed age between the emplacement of the Mesozoic and Early-Middle Palaeozoic granitoids.

5.2 AFT Age vs altitude plot

The AFT age vs altitude plot (Figure 11) displays the relationship between central AFT ages and the altitudes at which the samples were taken from. This plot is used to identify the timing of rapid cooling (Fitzgerald & Malusà, 2019). Two groups of data can be seen in Figure 11. The samples with younger AFT central ages come from a larger range of elevation

in comparison to the older samples. The nearly vertical age-elevation trend for these samples indicates a record of more rapid cooling in comparison to the older samples. Hence the Mid-Cretaceous AFT data may suggest a significant thermal event during the Cretaceous, while the older AFT ages are a record of slow cooling during the Jurassic. These suggestions coincide with the recorded cooling periods in the thermal history models (Figure 10).

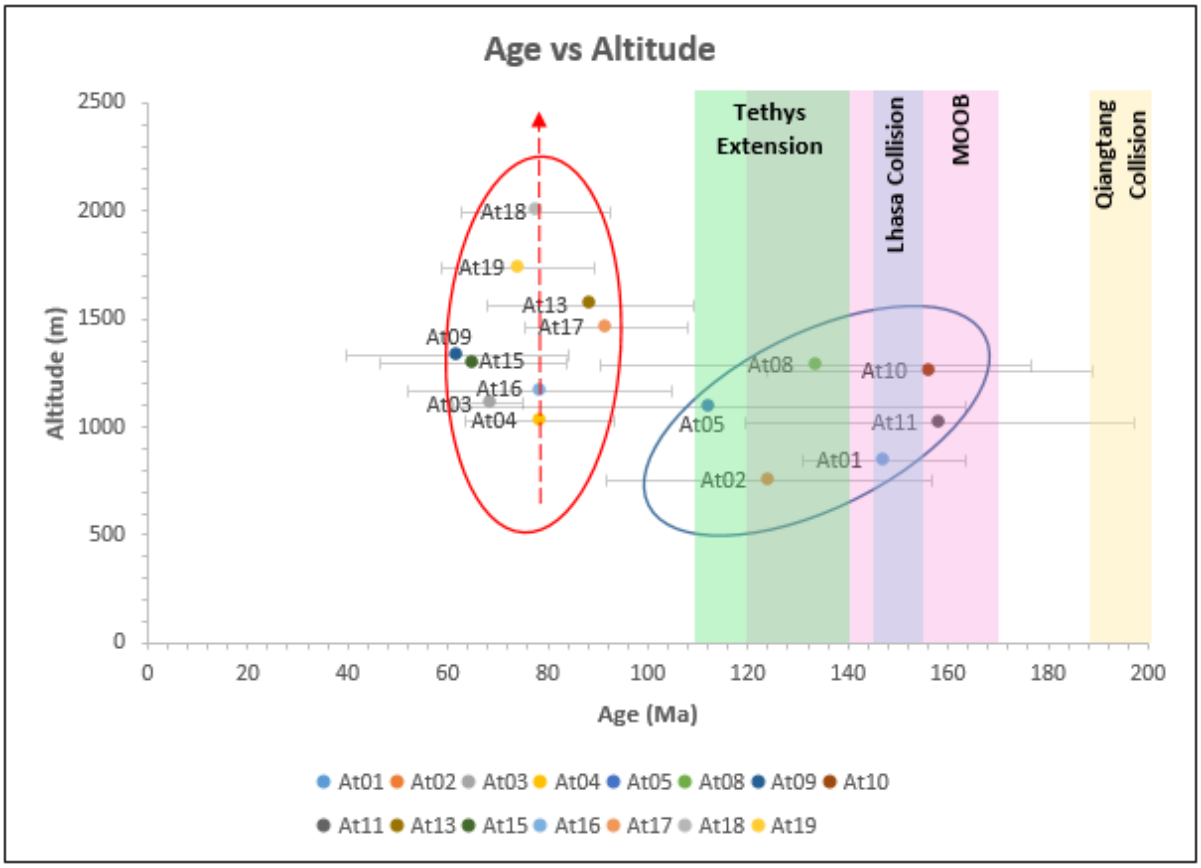

Figure 11 – Age vs altitude plot of all samples including age uncertainties (grey horizontal error bars). The Blue zone represents timing of the Lhasa collison, the green zone represents the timing of Tethys extension, the pink zone represents the timing of the MOOB formation and the beige zone represents the timing of the Qiangtang collision. The coloured ellipses represent two data trends. The red ellipse with the red arrow display a young age cluster of samples that were obtained from a larger elevation range. The blue ellipse contains the older samples that are from lower elevation on average.

5.3 AFT age vs mean track length 'Boomerang' plot

The 'Boomerang' plot compares central AFT ages with mean confined fission track lengths (MTL) for each sample (Gallagher, Brown, & Johnson, 1998; Green, 1986), which acts as

another means to help identify the main thermo-tectonic events that have impacted the study area. In this plot (Figure 12), two clear trends (circled) are evident on either sides of a characteristic ‘Boomerang’ trend. The two clusters on either ‘blade’ represent the samples which have longer MTLs and thus experienced relatively faster cooling. The data in the centre of the ‘curve’ represents samples with short MTLs, which reflects slow cooling, prolonged residence in the APAZ.

The full boomerang trend spans the Late Jurassic-Paleocene (Figure 12). The Late Jurassic marks the oldest AFT age recorded (~160 Ma) for a sample with a MTL of ~12.5 μm. All other samples with Jurassic-Early Cretaceous AFT ages record MTL values <12.5 μm indicative of prolonged residence time in the APAZ. AT-05 records the smallest MTLs of all the samples and sits around the central section of the boomerang. Longer MTLs begin at ~90 Ma (AT-13 and AT-17) and continue to increase in value until about 13 μm at ~65 Ma (AT-15). The samples with ~90-65 Ma AFT ages define the “second blade” of the boomerang trend. MTL values of ~13.5-14 μm (Gleadow et al., 1986) are required to record the timing of fast cooling events, which is thus likely at a time before 160 Ma and a time after 60 Ma in the study area.

In summary, the ‘Boomerang’ plot indicates two periods of rapid cooling, an older preservation of a thermal event in the Jurassic (>160 Ma) and a younger partial record of a <60 Ma thermal event. Additionally, there is some evidence for initiation of more rapid cooling since the Mid-Late Cretaceous (~90 Ma).

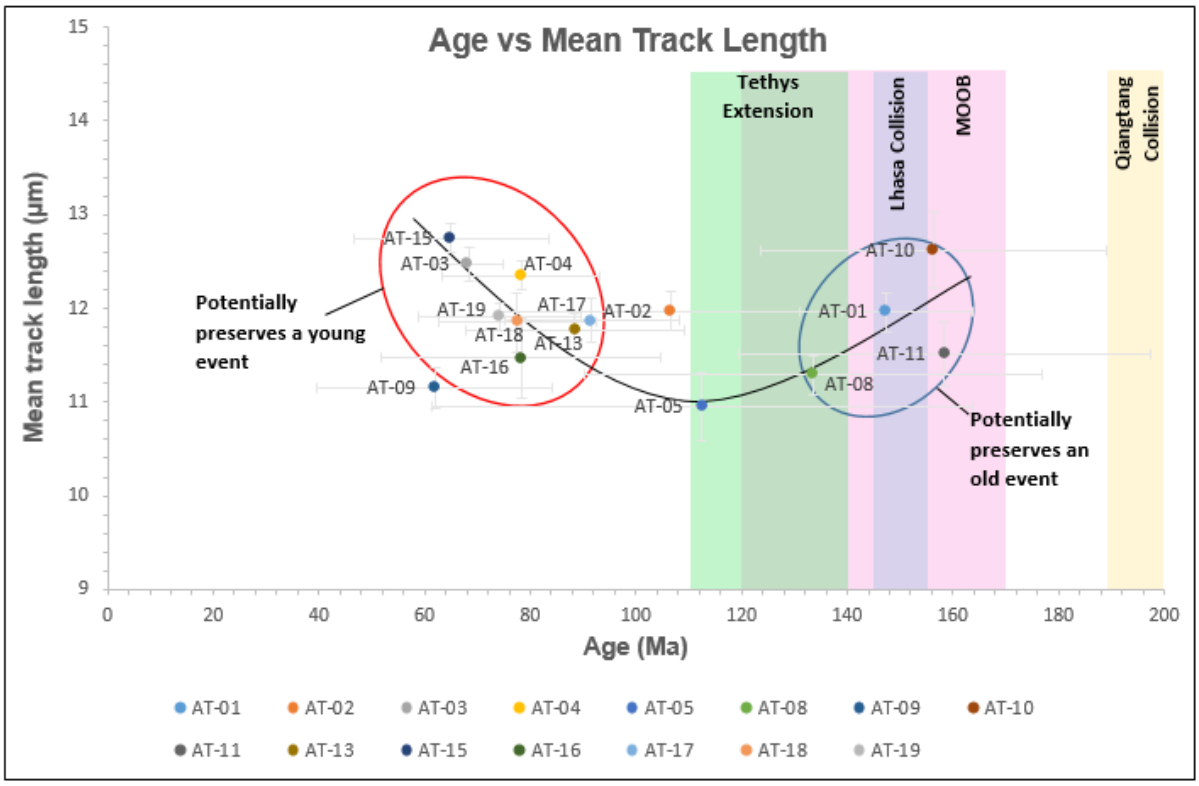

Figure 12 – 'Boomerang' plot displays the relationship between MTL and central AFT age for all samples in the study area. Age uncertainty is represented by the grey x-axis error bars. MTL uncertainty is represented by the grey y-axis error bars. Blue zone represents timing of the Lhasa collison, green zone represents the timing of Tethy's extension, the pink zone represents the timing of the MOOB formation and the beige zone represents the timing of the Qiangtang collision. The coloured ellipses represent two data trends. The red ellipse represents a cluster of samples that record a young event. The blue ellipse represents a cluster of samples that record an older event. The black solid line suggests the 'boomerang' trend.

5.4 Geographical distribution of cooling events and cooling mechanism

5.4.1 COOLING HISTORY AND EXHUMATION

As discussed above, three different thermal histories are preserved in the Chinese Altai. Samples that yielded the younger AFT central ages also contained the higher Cl concentrations, which indicates there is not a clear relationship between chemistry and age. This suggests that the different thermal histories are not controlled by the effects of annealing kinetics but rather by the geographic position of samples with respect to the structural architecture of the study area. As discussed earlier, understanding the sedimentation history in the local basins is required to form a relationship between the recorded cooling history

models and the exhumation history. This relationship is first understood by the positive feedback between thermal cooling, exhumation and erosion. Eroded sediments from the mountain building event are expected to be found in the nearby basins. If the sediment age coincides with the timing of the recorded thermal history, a relationship between the thermal history and cooling history can be made (e.g. Glorie and De Grave., 2016).

The Junggar Basin accumulated 5 km of terrestrial sediments transition between debris flows, alluvial fans, braided rivers and lacustrine environments over the Meso-Cenozoic. Weifeng and Yequan (2004) suggest the deposition to be in response to the collision of Cimmerian blocks (Lhasa and Qiangtang) at the Eurasian margin. Additionally, the Ob-Zaisan Basin records 6 km of Meso-Cenozoic clastic sediment that has been linked to the adjacent eroding Altai orogeny (Thomas et al., 2002). Similarly, The WSB contains Meso-Cenozoic clastic sediments. The sediment stratigraphy records are similar for the three nearby basins to the study area and comply with the timing of rapid cooling yielded in the thermal history models.

5.4.2 STRUCTURAL ARCHITECTURE

The Fuyun Fault formed in the Cretaceous (≤110 Ma) (Lin, 1994) and offsets the NW-SE orientated Irtysh Fault, which it intersects in the study area. An inverse distance weighted (IDW) interpolation map (Figure 13) was generated to revel the timing of exhumation with respect to the fault zone. The figure shows majority of the western side of the Fuyun Fault displays old AFT ages (cold colours), whilst east of the Fuyun Fault, the model records young AFT ages (hot colours), suggesting that the fault bocks have been reactivated with respect to the Fuyun Fault. Hence, the Fuyun Fault is the primary fault that accommodated strain in the Cretaceous, while the section of the Irtysh Fault in the study area appears to have been inactive at that time. Two faults splays of the Fuyun Fault also record Cretaceous AFT

ages, strengthening the observation that the Fuyun Fault controlled Cretaceous deformation and exhumation in the study area.

In more detail, one of the Fuyun Fault splays intersects the Fuyun-Xibodu Fault (Figure 13), which two samples (AT-03 and AT-04) are located along. In contrast, AT-05 and AT-11 are located on either side of this fault splay and record slow cooling thermal histories. Hence, the record of rapid cooling in the fault versus slow cooling away from the fault, suggests that the NW-SE orientated fault splay was reactivated during the Late Cretaceous. AT-09 is also located on a NE-SW orientated Fuyun Fault splay, which is located north the Tuerhongshate Shear Zone. Thermal history models suggest AT-09 records rapid cooling during Late Cretaceous and in the Neogene (Figure 10). Samples AT-08 and AT-10 are situated on fault blocks either side of the fault splay that AT-09 is located along and record older thermal histories (Figure 13). It is interpreted that the Fuyun Fault splay north of the Tuerhongshate Shear Zone was locally reactivated in response to an Early Cretaceous tectonic event as well as by an event in the Late Palaeogene-Early Neogene, whilst fault blocks either side were not.

Samples AT-01 and AT-02 are located in the ISZ. Based on thermal modelling and AFT interpretation plots (Figures 10A and 12), both samples record slow cooling thermal histories and thus suggest the ISZ was not reactivated in this section of the Chinese Altai. This finding differs to those from previous studies further west along the ISZ (e.g. Glorie, De Grave, Delvaux, et al. (2012), which indicates that the strain is being accommodated in the Chinese Altai.

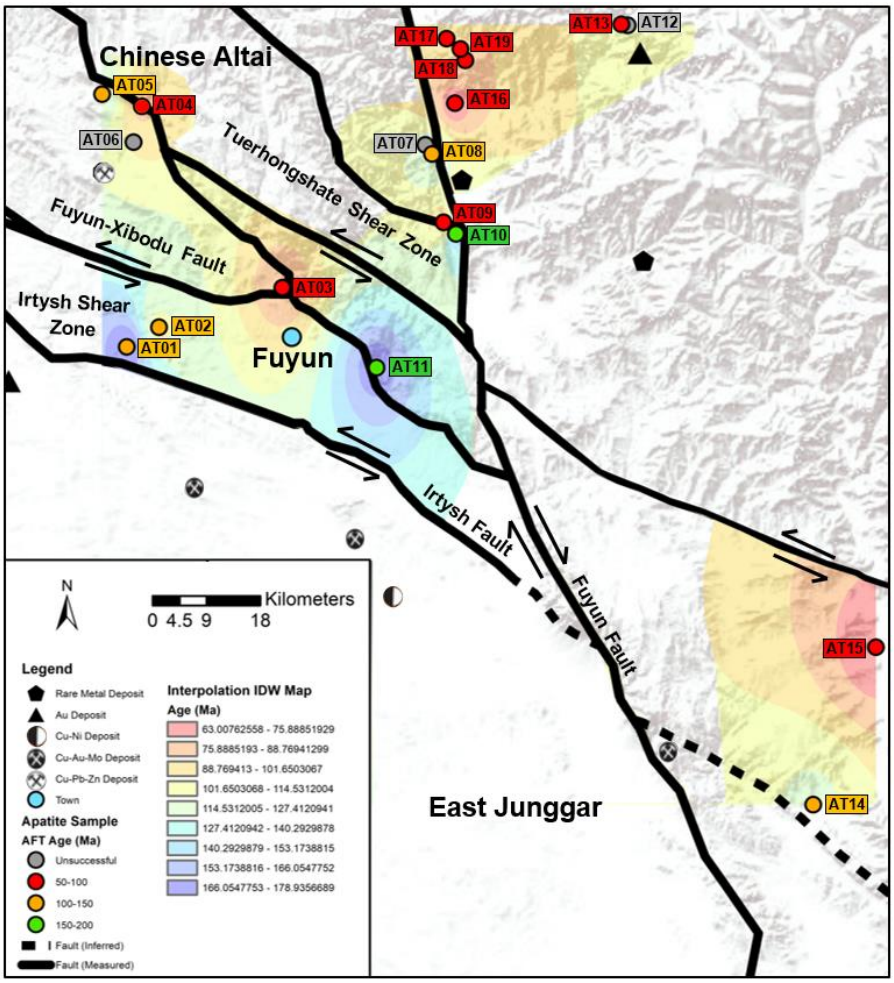

Figure 13 – Topographic terrain map showing all samples in the study area. An Inverse Distance Weighted (IDW) Interpolation map was generated using thermal history model age at 100 ºC within the APAZ. Hot colours represent areas consequent of reactivation whilst cold colours represent areas that record old granitoid emplacement. Sample symbols are coloured following their AFT age (red – 50-100 Ma, orange – 100-150 Ma, green – 150-200 Ma and grey – failed sample). Shear zones and known faults after Li, Sun, et al. (2015) are labelled, additionally when strike-slip displacement is known arrows show the offset direction. Ore deposits after Wan et al. (2011) and Wan et al. (2010).

5.5 The thermo-tectonic history of the Chinese Altai

5.5.1 PALAEOZOIC – JURASSIC

Samples with Palaeozoic AU-Pb ages that are similar to their ZU-Pb are interpreted to be linked to granitoid emplacement. Lower Devonian granitoid emplacement is considered to be linked to the subduction of the Palaeo-Pacific Plate during the closure of the PAO. Permian granitoid emplacement is considered to be in response to the closure of the PAO and/or in

response to region scale oroclinal bending during which the Irtysh Fault as well as other NW-SE orientated faults were created (Li, Sun, et al., 2015).

5.5.2 CRETACEOUS EXHUMATION

The majority of the AFT ages obtained in this study support the findings of previous studies within the Altai (e.g. De Grave, Van den haute, Buslov, Dehandschutter, & Glorie, 2008; Glorie, De Grave, Delvaux, et al., 2012; Jolivet et al., 2007; Yuan et al., 2006). The thermal history models record fast cooling that can be linked to exhumation and fault reactivation (see previous sections 5.4.1 and 5.4.2) at ~95-70 Ma, which correlates with AFT data across the Altai (e.g. Glorie, De Grave, Delvaux, et al., 2012; Yuan et al., 2006). Most of the samples that enter the APAZ during the Late Jurassic-Early Cretaceous record fast cooling, which is interpreted to be a lagged response (Glorie and De Grave., 2016) to the Qiangtang collision. As previously mentioned (see previous section 5.4.1), sedimentation in the adjacent basins support that the recorded rapid cooling is associated with a period of exhumation during that time. Additionally to sediments, the Junggar Basin records Cretaceous fault reactivation linked to regional compression as a result of tectonic deformation of Central Asia (Allen, Macdonald, Xun, Vincent, & Brouet-Menzies, 1997; Vincent & Allen, 2001). To the east of the study area, the closure of the Mongol-Okhotsk Ocean and the creation of the Mongol-Okhotsk Orogeny (Cogné, Kravchinsky, Halim, & Hankard, 2005; Kravchinsky, Cogné, Harbert, & Kuzmin, 2002) is suspected to have caused Cretaceous deformation in the Chinese Altai (De Grave et al., 2009; Novikov, 2002). Glorie, De Grave, Delvaux, et al. (2012) attributed their similar AFT ages and models further west along the ISZ to a localised increased uplift and denudation of a Mesozoic Altai orogeny as a result of far-field stress from the MOOB. Alternatively, Cretaceous deformation could be induced from stress propagation as a result of the far-field Lhasa Block collision at the Southern Eurasian margin

(De Grave et al., 2007); however, this event likely occurred too early to be responsible for the mid-late Cretaceous cooling recorded by our samples (Figure 10). Another possible interpretation is that the reactivation of faults and associated fault blocks in the Early Cretaceous may be associated to extensional tectonics in response to slab-rollback of the subducting Tethys Ocean (~140-110 Ma) (Zahirovic et al., 2016).

The structural history of the NW-SE orientated ISZ has been studied extensively and its formation has been linked to widespread oroclinal bending. The activation of the ISZ has been dated using $^{40}Ar/^{39}Ar$ methods to ~290-244 Ma in the Chinese Altai (Briggs et al., 2007; Laurent-Charvet et al., 2003; Li, Yuan, et al., 2015) and is suggested to be linked to sinistral shearing and contraction (Laurent-Charvet et al., 2003; Qu, 1991; Qu & Zhang, 1991) in the ISZ deformation history (Li, Sun, et al., 2015). In contrast, the Fuyun Fault is poorly structurally constrained and for this discussion, we consider the fault to be a transpressional (or transtensional) strike-slip fault since formation in the Cretaceous. In the study area, the eastern side of the Fuyun Fault has been exhumed with respect to the western side. The reactivated Fuyun Fault in the Chinese Altai is orientated in a NNW-SSE direction, which would align better with an ENE-WSW tensor resultant of the MOOB (170-120 Ma) then a SW-NE tensor subsequent of the Lhasa (155-145 Ma) or Tethys (~140-110 Ma) in the far south-west. The thermal history models suggest one or a combination of the regional tectonic events discussed previously are likely to be responsible for a widespread Cretaceous reactivation of the Chinese Altai. The modelled cooling pathways occur later than the events, which is suspected due to the time lag between cooling and denudation (Glorie and De Grave., 2016).

5.5.3 LATE PALAEOGENE – EARLY NEOGENE REACTIVATION

To the far south of the study area, subduction of the Neo-Tethys triggered the Indian-Eurasian continent-continent collision during the Cenozoic (Van Hinsbergen et al., 2012). The collision is linked to far field reactivation of the CAOB and is considered to be a main driver for the present day topography in the Altai Mountains (De Grave et al., 2007). The thermal history models support that the Chinese Altai has been reactivated in response to the Cenozoic India-Eurasia collision. This correlates with Glorie, De Grave, Delvaux, et al. (2012) further west along the ISZ, as their samples provided evidence for a Cenozoic rapid cooling event. A reactivation during this time is supported by clastic sedimentation in the Junggar Basin (Vincent & Allen, 2001) as well as in the Ob-Zaisan Basin which has been linked to the adjacent eroding Altai orogeny (Thomas et al., 2002).

5.6 Geographical distribution of ore belts and ore deposits

The VMS and Shear Zone-Related Ore Belts are rectangular zones following the NW-SE orientation of the ISZ (Figures 2 and 3) and are located in the Chinese Altai. The Porphyry Ore Belt is located beneath the Irtysh Fault in East Junggar. These zones and the mountain range further north are metal rich and are likely areas for mineral exploration. Using the collected sample elevation and AFT data, we attempt to draw a link between exhumation level and mineral prospectivity within the study area.

To the far north above the three ore belts mentioned previously, the mountains of the Chinese Altai host rare earth element (REE) deposits and a gold deposit in close proximity to sampled granitoids. These deposits are located on the highly exhumed side of the Fuyun Fault (eastern side) at more than 1100 m above sea level. The REE deposits are not seen elsewhere in the study area, which suggests that they require further uplifting or they were exhumed

previously and eroded away entirely. Detected mineral deposits in the ore belts are located in areas away from collected data, hence a link between exhumation and mineral prospectivity cannot be made.

6. CONCLUSIONS

We have revealed the low-temperature thermal history of the Chinese Altai in relation to the deformation history of the Fuyun Fault.

1. Apatite samples yield Lower Devonian-Jurassic U-Pb ages (~415-153 Ma), which reflect cooling in response to the subduction and closure of the Palaeo-Asian Ocean, regional oroclinal bending and the Qiangtang collision.
2. Central AFT ages and thermal history models reflect Late Jurassic-Early Cretaceous fast cooling, which is interpreted to be a lagged response to the Qiangtang collision (~230-190 Ma).
3. Central AFT ages and thermal history modelling indicate the Fuyun Fault was active during the Cretaceous (~120-70 Ma), possibly linked to far field effects of the MOOB formation (170-120 Ma) or slab-rollback of the subducting Tethys Ocean (~140-110 Ma).
4. Thermal history models suggest renewed tectonic activity within the Chinese Altai during Late Palaeogene-Early Neogene (~30-10 Ma). This recent cooling history is interpreted to be associated with the India-Eurasia collision and convergence.

7. ACKNOWLEDGMENTS

I would like to thank my supervisor, Stijn Glorie, as well as PhD Students Jack Gillespie, Angus Nixon and Gilby Jepson for their assistance throughout the project. I would also like to thank Juraj Farkas and Katie Howard for their support to myself and the entire honours cohort throughout the year. Finally, I would also like to thank Sarah Gilbert for her assistance with the LA-ICP-MS equipment and optical microscopes provided by Adelaide Microscopy.

8. REFERENCES

ALLEN, M., MACDONALD, D., XUN, Z., VINCENT, S., & BROUET-MENZIES, C. (1997). Early Cenozoic two-phase extension and late Cenozoic thermal subsidence and inversion of the Bohai Basin, northern China. *Marine and Petroleum Geology, 14*(7-8), 951-972.

ALLEN, M., & NATAL'IN, B. (1995). Junggar, Turfan and Alakol basins as Late Permian to? Early Triassic extensional structures in a sinistral shear zone in the Altaid orogenic collage, Central Asia. *Journal of the Geological Society, 152*(2), 327-338.

BRIGGS, S. M., YIN, A., MANNING, C. E., CHEN, Z.-L., WANG, X.-F., & GROVE, M. (2007). Late Paleozoic tectonic history of the Ertix Fault in the Chinese Altai and its implications for the development of the Central Asian Orogenic System. *Geological Society of America Bulletin, 119*(7-8), 944-960.

BUSLOV, M., WATANABE, T., FUJIWARA, Y., IWATA, K., SMIRNOVA, L., SAFONOVA, I. Y., KIRYANOVA, A. (2004). Late Paleozoic faults of the Altai region, Central Asia: tectonic pattern and model of formation. *Journal of Asian Earth Sciences, 23*(5), 655-671.

CHEN, L., & HAN, B. (2006). Geochronology, geochemistry and Sr-Nd-Pb isotopic composition of maric intrusive rocks in Wuqiagou area, north Xinjiang: Constraints for mantle sources and deep processes. *Acta Petrologica Sinica, 22*(5), 1201-1214.

CHEW, D., PETRUS, J., & KAMBER, B. (2014). U–Pb LA–ICPMS dating using accessory mineral standards with variable common Pb. *Chemical Geology, 363*, 185-199.

CHEW, D. M., DONELICK, R. A., DONELICK, M. B., KAMBER, B. S., & STOCK, M. J. (2014). Apatite chlorine concentration measurements by LA-ICP-MS. *Geostandards and Geoanalytical Research, 38*(1), 23-35.

CHEW, D. M., & SPIKINGS, R. A. (2015). Geochronology and thermochronology using apatite: time and temperature, lower crust to surface. *Elements, 11*(3), 189-194.

COGNÉ, J.-P., KRAVCHINSKY, V. A., HALIM, N., & HANKARD, F. (2005). Late Jurassic-Early Cretaceous closure of the Mongol-Okhotsk Ocean demonstrated by new Mesozoic palaeomagnetic results from the Trans-Baikal area (SE Siberia). *Geophysical Journal International, 163*(2), 813-832.

DAVIES, C., ALLEN, M. B., BUSLOV, M. M., & SAFONOVA, I. (2010). Deposition in the Kuznetsk Basin, Siberia: insights into the Permian–Triassic transition and the Mesozoic evolution of Central Asia. *Palaeogeography, Palaeoclimatology, Palaeoecology, 295*(1-2), 307-322.

DE GRAVE, J. (2002). Denudation and cooling of the Lake Teletskoye Region in the Altai Mountains (South Siberia) as revealed by apatite fission-track thermochronology. *Tectonophysics, 349*(1-4), 145-159.

DE GRAVE, J., BUSLOV, M. M., & VAN DEN HAUTE, P. (2007). Distant effects of India–Eurasia convergence and Mesozoic intracontinental deformation in Central Asia: Constraints from apatite fission-track thermochronology. *Journal of Asian Earth Sciences, 29*, 188-204. doi:10.1016/j.jseaes.2006.03.001

DE GRAVE, J., BUSLOV, M. M., VAN DEN HAUTE, P., METCALF, J., DEHANDSCHUTTER, B., & MCWILLIAMS, M. O. (2009). Multi-method chronometry of the Teletskoye graben and its basement, Siberian Altai Mountains: new insights on its thermo-tectonic evolution. *Geological Society, London, Special Publications, 324*(1), 237-259.

DE GRAVE, J., DE PELSMAEKER, E., ZHIMULEV, F. I., GLORIE, S., & BUSLOV, M. M. (2014). Meso-Cenozoic building of the northern Central Asian Orogenic Belt: thermotectonic history of the Tuva region. *Tectonophysics, 621*, 44-59.

DE GRAVE, J., GLORIE, S., RYABININ, A., ZHIMULEV, F., BUSLOV, M. M., IZMER, A., VAN DEN HAUTE, P. (2012). Late Palaeozoic and Meso-Cenozoic tectonic evolution of the southern Kyrgyz Tien Shan: Constraints from multi-method thermochronology in the Trans-Alai, Turkestan-Alai segment and the southeastern Ferghana Basin. *Journal of Asian Earth Sciences, 44*, 149-168. doi:10.1016/j.jseaes.2011.04.019

DE GRAVE, J., VAN DEN HAUTE, P., BUSLOV, M. M., DEHANDSCHUTTER, B., & GLORIE, S. (2008). Apatite fission-track thermochronology applied to the Chulyshman Plateau, Siberian Altai Region. *Radiation Measurements, 43*(1), 38-42. doi:10.1016/j.radmeas.2007.11.068

FITZGERALD, P. G., & MALUSÀ, M. G. (2019). Concept of the Exhumed Partial Annealing (Retention) Zone and Age-Elevation Profiles in Thermochronology. In *Fission-Track Thermochronology and its Application to Geology* (pp. 165-189): Springer.

GALBRAITH, R., & LASLETT, G. (1993). Statistical models for mixed fission track ages. *Nuclear tracks and radiation measurements, 21*(4), 459-470.

GALLAGHER, K. (2012). Transdimensional inverse thermal history modeling for quantitative thermochronology. *Journal of Geophysical Research: Solid Earth, 117*(B2).

GALLAGHER, K., BROWN, R., & JOHNSON, C. (1998). Fission track analysis and its applications to geological problems. *Annual Review of Earth and Planetary Sciences, 26*(1), 519-572.

GILLESPIE, J., GLORIE, S., XIAO, W., ZHANG, Z., COLLINS, A. S., EVANS, N., DE GRAVE, J. (2017). Mesozoic reactivation of the Beishan, southern Central Asian Orogenic Belt: Insights from low-temperature thermochronology. *Gondwana Research, 43*, 107-122. doi:10.1016/j.gr.2015.10.004

GLEADOW, A., DUDDY, I., GREEN, P. F., & LOVERING, J. (1986). Confined fission track lengths in apatite: a diagnostic tool for thermal history analysis. *Contributions to Mineralogy and Petrology, 94*(4), 405-415.

GLEADOW, A. J., DUDDY, I. R., GREEN, P. F., & HEGARTY, K. A. (1986). Fission track lengths in the apatite annealing zone and the interpretation of mixed ages. *Earth and planetary science letters, 78*(2-3), 245-254.

GLORIE, S., AGOSTINO, K., DUTCH, R., PAWLEY, M., HALL, J., DANIŠÍK, M., COLLINS, A. S. (2017). Thermal history and differential exhumation across the Eastern Musgrave Province, South Australia: Insights from low-temperature thermochronology. *Tectonophysics, 703*, 23-41.

GLORIE, S., & DE GRAVE, J. (2016). Exhuming the Meso–Cenozoic Kyrgyz Tianshan and Siberian Altai-Sayan: A review based on low-temperature thermochronology. *Geoscience Frontiers, 7*(2), 155-170. doi:10.1016/j.gsf.2015.04.003

GLORIE, S., DE GRAVE, J., BUSLOV, M. M., ZHIMULEV, F. I., ELBURG, M. A., & VAN DEN HAUTE, P. (2012). Structural control on Meso-Cenozoic tectonic reactivation and denudation in the Siberian Altai: Insights from multi-method thermochronometry. *Tectonophysics, 544-545*, 75-92. doi:10.1016/j.tecto.2012.03.035

GLORIE, S., DE GRAVE, J., DELVAUX, D., BUSLOV, M. M., ZHIMULEV, F. I., VANHAECKE, F., VAN DEN HAUTE, P. (2012). Tectonic history of the Irtysh shear zone (NE Kazakhstan): New constraints from zircon U/Pb dating, apatite fission track dating and palaeostress analysis. *Journal of Asian Earth Sciences, 45*, 138-149. doi:10.1016/j.jseaes.2011.09.024

GLORIE, S., OTASEVIC, A., GILLESPIE, J., JEPSON, G., DANIŠÍK, M., ZHIMULEV, F., XIAO, W. (2019). Thermo-tectonic history of the Junggar Alatau within the Central Asian Orogenic Belt (SE Kazakhstan, NW China): Insights from integrated apatite U/Pb, fission track and (U–Th)/He thermochronology. *Geoscience Frontiers*.

GREEN, P., DUDDY, I., GLEADOW, A., TINGATE, P., & LASLETT, G. (1986). Thermal annealing of fission tracks in apatite: 1. A qualitative description. *Chemical Geology: Isotope Geoscience Section, 59*, 237-253.

GREEN, P. F. (1986). On the thermo-tectonic evolution of Northern England: evidence from fission track analysis. *Geological Magazine, 123*(5), 493-506.

HASEBE, N., BARBARAND, J., JARVIS, K., CARTER, A., & HURFORD, A. J. (2004). Apatite fission-track chronometry using laser ablation ICP-MS. *Chemical Geology, 207*(3-4), 135-145.

HENDRIKS, B., & REDFIELD, T. (2005). Apatite fission track and (U-Th)/He data from Fennoscandia: An example of underestimation of fission track annealing in apatite. *Earth and planetary science letters, 236*(1-2), 443-458.

JAHN, B.-M. (2004). The Central Asian Orogenic Belt and growth of the continental crust in the Phanerozoic. *Geological Society, London, Special Publications, 226*(1), 73-100.

JAHN, B.-M., WU, F., & CHEN, B. (2000). Granitoids of the Central Asian Orogenic Belt and continental growth in the Phanerozoic. *Earth and Environmental Science Transactions of the Royal Society of Edinburgh, 91*(1-2), 181-193.

JEPSON, G., GLORIE, S., KONOPELKO, D., MIRKAMALOV, R., DANIŠÍK, M., & COLLINS, A. S. (2018). The low-temperature thermo-tectonic evolution of the western Tian Shan, Uzbekistan. *Gondwana Research, 64*, 122-136.

JOLIVET, M., DE BOISGROLLIER, T., PETIT, C., FOURNIER, M., SANKOV, V., RINGENBACH, J. C., ANISIMOVA, S. (2009). How old is the Baikal Rift Zone? Insight from apatite fission track thermochronology. *Tectonics, 28*(3).

JOLIVET, M., RITZ, J.-F., VASSALLO, R., LARROQUE, C., BRAUCHER, R., TODBILEG, M., ARZHANIKOV, S. (2007). Mongolian summits: An uplifted, flat, old but still preserved erosion surface. *Geology, 35*(10). doi:10.1130/g23758a.1

KAPP, P., DECELLES, P. G., GEHRELS, G. E., HEIZLER, M., & DING, L. (2007). Geological records of the Lhasa-Qiangtang and Indo-Asian collisions in the Nima area of central Tibet. *Geological Society of America Bulletin, 119*(7-8), 917-933.

KRAVCHINSKY, V. A., COGNÉ, J.-P., HARBERT, W. P., & KUZMIN, M. I. (2002). Evolution of the Mongol-Okhotsk Ocean as constrained by new palaeomagnetic data from the Mongol-Okhotsk suture zone, Siberia. *Geophysical Journal International, 148*(1), 34-57.

LAURENT-CHARVET, S., CHARVET, J., MONIÉ, P., & SHU, L. (2003). Late Paleozoic strike-slip shear zones in eastern Central Asia (NW China): New structural and geochronological data. *Tectonics, 22*(2).

LE HERON, D. P., BUSLOV, M. M., DAVIES, C., RICHARDS, K., & SAFONOVA, I. (2008). Evolution of Mesozoic fluvial systems along the SE flank of the West Siberian Basin, Russia. *Sedimentary Geology, 208*(1-2), 45-60.

LI, P., SUN, M., ROSENBAUM, G., CAI, K., & YU, Y. (2015). Structural evolution of the Irtysh Shear Zone (northwestern China) and implications for the amalgamation of arc systems in the Central Asian Orogenic Belt. *Journal of Structural Geology, 80*, 142-156. doi:10.1016/j.jsg.2015.08.008

LI, P., SUN, M., ROSENBAUM, G., JOURDAN, F., LI, S., & CAI, K. (2017). Late Paleozoic closure of the Ob-Zaisan Ocean along the Irtysh shear zone (NW China): Implications for arc amalgamation and oroclinal bending in the Central Asian orogenic belt. *Geological Society of America Bulletin, 129*(5-6), 547-569. doi:10.1130/b31541.1

LI, P., YUAN, C., SUN, M., LONG, X., & CAI, K. (2015). Thermochronological constraints on the late Paleozoic tectonic evolution of the southern Chinese Altai. *Journal of Asian Earth Sciences, 113*, 51-60.

LI, S., WANG, T., WILDE, S. A., & TONG, Y. (2013). Evolution, source and tectonic significance of Early Mesozoic granitoid magmatism in the Central Asian Orogenic Belt (central segment). *Earth-Science Reviews, 126*, 206-234.

LIN, A. (1994). Glassy pseudotachylyte veins from the Fuyun fault zone, northwest China. *Journal of Structural Geology, 16*(1), 71-83.

MCDOWELL, F. W., MCINTOSH, W. C., & FARLEY, K. A. (2005). A precise 40Ar–39Ar reference age for the Durango apatite (U–Th)/He and fission-track dating standard. *Chemical Geology, 214*(3-4), 249-263.

METELKIN, D., VERNIKOVSKY, V., & KAZANSKY, A. Y. (2012). Tectonic evolution of the Siberian paleocontinent from the Neoproterozoic to the Late Mesozoic: paleomagnetic record and reconstructions. *Russian Geology and Geophysics, 53*(7), 675-688.

METELKIN, D. V., VERNIKOVSKY, V. A., KAZANSKY, A. Y., & WINGATE, M. T. D. (2010). Late Mesozoic tectonics of Central Asia based on paleomagnetic evidence. *Gondwana Research, 18*(2-3), 400-419. doi:10.1016/j.gr.2009.12.008

NACHTERGAELE, S., DE PELSMAEKER, E., GLORIE, S., ZHIMULEV, F., JOLIVET, M., DANIŠÍK, M., DE GRAVE, J. (2018). Meso-Cenozoic tectonic evolution of the Talas-Fergana region of the Kyrgyz Tien Shan revealed by low-temperature basement and detrital thermochronology. *Geoscience Frontiers, 9*(5), 1495-1514. doi:10.1016/j.gsf.2017.11.007

NOVIKOV, I. (2002). Late Paleozoic, Middle Mesozoic, and Late Cenozoic stages of the Altai orogeny. *Geologiya I Geofizika, 43*(5), 434-445.

O'SULLIVAN, P. B., & PARRISH, R. R. (1995). The importance of apatite composition and single-grain ages when interpreting fission track data from plutonic rocks: a case study from the Coast Ranges, British Columbia. *Earth and planetary science letters, 132*(1-4), 213-224.

OTTO, S. C. (1997). Mesozoic-Cenozoic history of deformation and petroleum systems in sedimentary basins of Central Asia; implications of collisions on the Eurasian margin. *Petroleum Geoscience, 3*(4), 327-341.

PATON, C., HELLSTROM, J., PAUL, B., WOODHEAD, J., & HERGT, J. (2011). Iolite: Freeware for the visualisation and processing of mass spectrometric data. *Journal of Analytical Atomic Spectrometry, 26*(12), 2508-2518.

PETERSON, J. A., & CLARKE, J. W. (1991). *Geology and hydrocarbon habitat of the West Siberian Basin*: Amer Assn of Petroleum Geologists.

QU, G. (1991). Deformational structure of tectonic division of the Altaides, Xinjiang. *Geoscience, 3*, 132-144.

QU, G., & ZHANG, J. (1991). Irtys structural zone. *Geoscience Xinjiang, 3*(11).

REDFIELD, T. (2010). On apatite fission track dating and the Tertiary evolution of West Greenland topography. *Journal of the Geological Society, 167*(2), 261-271.

SAUNDERS, A. D., ENGLAND, R. W., REICHOW, M. K., & WHITE, R. V. (2005). A mantle plume origin for the Siberian traps: uplift and extension in the West Siberian Basin, Russia. *Lithos, 79*(3-4), 407-424.

SCHWAB, M., RATSCHBACHER, L., SIEBEL, W., MCWILLIAMS, M., MINAEV, V., LUTKOV, V., FRISCH, W. (2004). Assembly of the Pamirs: Age and origin of magmatic belts from the southern Tien Shan to the southern Pamirs and their relation to Tibet. *Tectonics, 23*(4).

ŞENGÖR, A., NATAL'IN, B., & BURTMAN, V. (1993). Evolution of the Altaid tectonic collage and Palaeozoic crustal growth in Eurasia. *Nature, 364*(6435), 299.

TAPPONNIER, P., & MOLNAR, P. (1976). Slip-line field theory and large-scale continental tectonics. *Nature, 264*(5584), 319.

THOMAS, J.-C., LANZA, R., KAZANSKY, A., ZYKIN, V., SEMAKOV, N., MITROKHIN, D., & DELVAUX, D. (2002). Paleomagnetic study of Cenozoic sediments from the Zaisan basin (SE Kazakhstan) and the Chuya depression (Siberian Altai): tectonic implications for central Asia. *Tectonophysics, 351*(1-2), 119-137.

TONG, Y., WANG, T., JAHN, B.-M., SUN, M., HONG, D.-W., & GAO, J.-F. (2014). Post-accretionary Permian granitoids in the Chinese Altai orogen: geochronology, petrogenesis and tectonic implications. *American Journal of Science, 314*(1), 80-109.

VAN HINSBERGEN, D. J., LIPPERT, P. C., DUPONT-NIVET, G., MCQUARRIE, N., DOUBROVINE, P. V., SPAKMAN, W., & TORSVIK, T. H. (2012). Greater India Basin hypothesis and a two-stage Cenozoic collision between India and Asia. *Proceedings of the National Academy of Sciences, 109*(20), 7659-7664.

VERMEESCH, P. (2009). RadialPlotter: A Java application for fission track, luminescence and other radial plots. *Radiation Measurements, 44*(4), 409-410.

VERMEESCH, P. (2017). Statistics for LA-ICP-MS based fission track dating. *Chemical Geology, 456*, 19-27.

VINCENT, S. J., & ALLEN, M. B. (2001). Sedimentary record of Mesozoic intracontinental deformation in the eastern Junggar Basin, northwest China: response to orogeny at the Asian margin. *Memoirs-Geological Society of America*, 341-360.

WAGNER, G., GLEADOW, A., & FITZGERALD, P. (1989). The significance of the partial annealing zone in apatite fission-track analysis: Projected track length measurements and uplift chronology of the Transantarctic Mountains. *Chemical Geology: Isotope Geoscience Section, 79*(4), 295-305.

WAN, B., XIAO, W., ZHANG, L., WINDLEY, B. F., HAN, C., & QUINN, C. D. (2011). Contrasting styles of mineralization in the Chinese Altai and East Junggar, NW China: implications for the accretionary history of the southern Altaids. *Journal of the Geological Society, 168*(6), 1311-1321.

WAN, B., ZHANG, L., & XIANG, P. (2010). The Ashele VMS-type Cu-Zn deposit in Xinjiang, NW China formed in a rifted arc setting. *Resource Geology, 60*(2), 150-164.

WEIFENG, W., & YEQUAN, C. (2004). Tectonic evolution and petroleum systems in the Junggar Basin. *Acta Geologica Sinica-English Edition, 78*(3), 667-675.

WILHEM, C., WINDLEY, B. F., & STAMPFLI, G. M. (2012). The Altaids of Central Asia: a tectonic and evolutionary innovative review. *Earth-Science Reviews, 113*(3-4), 303-341.

WINDLEY, B., ALEXEIEV, D., XIAO, W., KRÖNER, A., & BADARCH, G. (2007). Tectonic models for accretion of the Central Asian Orogenic Belt. *Journal of the Geological Society, 164*, 31-47. doi:10.1144/0016-76492006-022

XIAO, W., HUANG, B., HAN, C., SUN, S., & LI, J. (2010). A review of the western part of the Altaids: a key to understanding the architecture of accretionary orogens. *Gondwana Research, 18*(2-3), 253-273.

XIAO, W., & SANTOSH, M. (2014). The western Central Asian Orogenic Belt: a window to accretionary orogenesis and continental growth. *Gondwana Research, 25*(4), 1429-1444.

XIAO, W., WINDLEY, B. F., HAN, C., LIU, W., WAN, B., ZHANG, J. E., SONG, D. (2018). Late Paleozoic to early Triassic multiple roll-back and oroclinal bending of the Mongolia collage in Central Asia. Earth-Science Reviews, 186, 94-128.

XIAO, W., WINDLEY, B. F., SUN, S., LI, J., HUANG, B., HAN, C., CHEN, H. (2015). A Tale of Amalgamation of Three Permo-Triassic Collage Systems in Central Asia: Oroclines, Sutures, and Terminal Accretion. *Annual Review of Earth and Planetary Sciences, 43*(1), 477-507. doi:10.1146/annurev-earth-060614-105254

YIN, A., & HARRISON, T. M. (2000). Geologic evolution of the Himalayan-Tibetan orogen. *Annual Review of Earth and Planetary Sciences, 28*(1), 211-280.

YUAN, W., CARTER, A., DONG, J., BAO, Z., AN, Y., & GUO, Z. (2006). Mesozoic–Tertiary exhumation history of the Altai Mountains, northern Xinjiang, China: New constraints from apatite fission track data. *Tectonophysics, 412*(3-4), 183-193. doi:10.1016/j.tecto.2005.09.007

ZAHIROVIC, S., MATTHEWS, K. J., FLAMENT, N., MÜLLER, R. D., HILL, K. C., SETON, M., & GURNIS, M. (2016). Tectonic evolution and deep mantle structure of the eastern Tethys since the latest Jurassic. *Earth-Science Reviews, 162*, 293-337. doi:10.1016/j.earscirev.2016.09.005

ZHANG, C.-L., SANTOSH, M., ZOU, H.-B., XU, Y.-G., ZHOU, G., DONG, Y.-G., WANG, H.-Y. (2012). Revisiting the “Irtish tectonic belt”: Implications for the Paleozoic tectonic evolution of the Altai orogen. *Journal of Asian Earth Sciences, 52*, 117-133.

ZHOU, G., ZHANG, Z., WANG, X.-K., WANG, X., LUO, S., HE, B., & ZHANG, X. (2007). Zircon U-Pb SHRIMP and 40Ar-39Ar dating of the granitic mylonite in the Mayinebo fault belt of north Xinjiang and its geological significance. *Acta Geologica Sinica, 81*(3), 359-369.

9. APPENDIX A: EXTENDED METHODS

9.1 Crushing and separation

The samples were crushed and separated at the Institute of Geology and Geophysics, Chinese Academy of Sciences (IGGCAS) following normal procedures.

9.2 Picking

Picking apatite grains from the crushed samples was the first step of the AFT analysis process. Using two side by side Olympus SZ61 microscopes under ~45x magnification, we were able to pick grains from a petri dish under one microscope and place them onto a thin section slide under the other microscope. The shallow petri dishes were ~10cm in diameter and were thoroughly cleaned with ethanol before and in between samples. Double sided tape was used to ensure the apatite grains were held in place (Figure 14). A reference point was drawn on the slide prior to fixing the tape to the slide. This was done to ensure maximum density of the grains in the one location whilst making sure the slide would still fit within the Resonetics M-50 laser chamber for analysis in a later stage. Dependent on grain availability, 100 apatite grains were picked; unfortunately, some samples did not contain this quantity. Apatite grains were positioned in an orientation so that the c-axis was parallel to the surface. Apatites were picked based on their clear colour, hexagonal crystal shape and absence of visual fractures and inclusions. Grains smaller than ~50μm were avoided in the picking process as they may be lost later during the laser ablation process. A fine needle was used to select and transport apatite grains to the slide, where the grains were placed in an organised grid on the reference point.

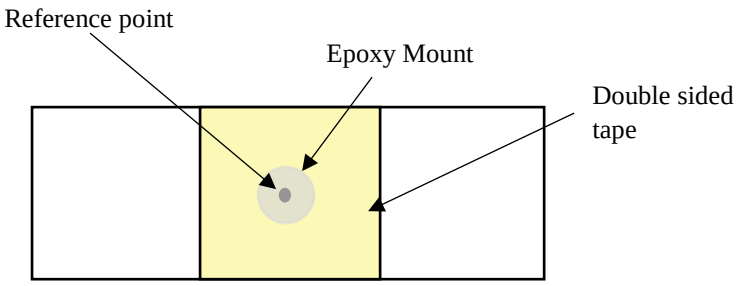

Figure 14 - The configuration of the thin section slide used for apatite picking and mounting.

9.3 Mounting

Prior to creation of the epoxy mixture, a plastic cup was tared on a set of scales. Precisely 1g of epoxy resin was firstly poured into the cup, followed by 0.2g of epoxy hardener. The 5:1 epoxy mixture was slowly and steadily stirred to homogenise the mixture whilst carefully prepared to prevent the creation of air bubbles. The mixture was then dripped onto the sample grid until there was a bubble-like shape of mixture surrounding the reference point. A new slide was then cleaned with ethanol and placed exactly on top of the picking slide. In order to control the height of the epoxy surface, extra slides were used as spacers to ensure the mixture was exactly 1 slide thick. The mounts were left to dry over a 3 day period and once dried, the sticky tape was separated from the picking slide with the use of a razor blade. This was done to expose the apatite grains for the grinding process.

9.4 Grinding

Ethanol was used to remove the sticky tape residue from the apatite mounts. The mounts were then grinded against fine wet 1000 sand paper to expose the internal section of the crystals. The mounts were rubbed in a figure-eight pattern to ensure even grinding across the mount. After 15 seconds of grinding, the mounts were checked under a picking microscope to analyse the degree of grinding. The mount became less reflective and contained an evenly

scratched surface when the grinding was sufficient. Once the mounts had reached this stage, the top 1/3-1/4 of the apatite grain had been removed; however, there was still enough grain beneath the epoxy surface to hold it in place.

9.5 Polishing

Post grinding, the edges and corners of the mount slide were grounded down and smoothed out to prevent damage to the polishing cloths.

The mounts were firstly polished on a 3µm cloth with 3µm diamond suspension paste for two 10 minute intervals. Following this, the mounts were then polished on a 1µm cloth with 1µm diamond suspension paste for two 3 minute intervals. The 3µm cloth and paste was used first in order to remove large scratches and imperfections. The 1µm was used second to ensure the surface was polished smoothly and evenly. It was crucial to make sure the correct cloth was used for the selected diamond paste to ensure polishing effectiveness. The mounts were span for the entire time period to ensure an even polish. After the mounts underwent the two stages of polishing, the mount was checked under a high powered microscope at ~100x magnification to access the polished surface. Polishing was then continued based on the condition of the surface for each individual mount. This step continued until the surface of the apatites showed no further improvement.

9.6 Etching

This step is used to reveal the ^{238}U fission tracks. The samples were first cleaned with ethanol and then dried to avoid any contamination or dilution to the etching acid. A small beaker (250ml) was half filled with 5M HNO_3 at 20^{o}C and was placed alongside a large beaker (500ml) filled with deionised water. Two mounts were submerged in the nitric acid at the

same time for 20±0.5 seconds and then were instantly placed in the beaker containing deionised water. It was important to do this quickly to dilute the acid and thus prevent future etching. This method was continued for 10 samples (5 runs) and then the beaker containing 5M HNO_3 was emptied and refreshed. This was done in order to ensure the acid was the same strength and thus etching across all samples would be uniform.

9.7 Counting

Firstly, a minimum of 40 apatite grains (where possible) were imaged using a Zeiss AXIO Imager M2m Autoscan System under a magnification of 1000X. Imaged grains strictly had a width of 50μm or more so the region of interest (ROI) of the counting area was 10μm from either edge thus allowing a 30μm spacing for the laser spot in between. This was done to prevent the inclusion of foreign geochemical traces from outside of the targeted grain as external fission tracks could protrude into the ROI without precautions. ROI's were created on the imaged grains using FastTracks software and was used to calculate the fission track density. The counted area is also the target location for the laser ablation where element concentrations (U, Pb, Cl etc.) will be measured and more importantly, will be used to constrain fission track age. One Durango apatite standard was counted per 20 'unknown' grains (apatite grains to be analysed) were counted for calibration purposes prior to laser ablation.

Confined fission tracks are tracks that have not breached the surface and thus preserve their entire length. Confined tracks are revealed from the etching process when the acid enters the confined track via an intersection with a track that has penetrated the surface (TINTs) or via a crack or cleavage in the grain (TINCLEs) (A. Gleadow et al., 1986). Confined tracks were measured using the FastTracks software in order to generate thermal history cooling models.

A minimum of 30 confined tracks were required to produce a model; however, the target was 100 confined tracks.

9.8 LA-ICP-MS analysis

The apatite grains were analysed using laser ablation inductively coupled with plasma mass spectrometry (LA-ICP-MS) in order to measure elemental concentrations (U, Pb, Cl etc.). This was accomplished using a solid state New Wave-213 laser which was coupled with an Agilent 7900X mass spectrometer (analytical data in Table 2). Care was taken to place the 30μm laser ablation spot diameter in localities of fission track homogeneity to ensure precise and accurate ages. To further assure the legitimacy of results, the laser ablation sessions were set up to analyse a 'block' of standards to calibrate prior to every twenty unknown grains. Each block of standards contained one Durango apatite standard, one McClure apatite standard, two Madagascar standards and two NIST 610 standards.

9.9 Data reduction

Iolite software was used in the data reduction process (Paton, Hellstrom, Paul, Woodhead, & Hergt, 2011), where Madagascar was used as the primary standard for the AU-Pb analysis and Durango as the primary standard for the AFT analysis (D. M. Chew et al., 2014). Data reduction was executed by creating customised raw data spreadsheets. These spreadsheets were then fed through an analytical run in Iolite to examine the LA-ICP-MS analysis U/Ca ratio for each grain as a line graph. This was done to determine if any grains produced anomalous features including spikes or increasing/decreasing trends. Any existing anomalous features are disregarded when possible as the signal should be flat, thus indicating a steady signal of U/Ca throughout the grain. The NIST 610 and McClure standards were also used to

test the accuracy of the acquired data from the unknown samples. Using the ^{238}U concentrations and calculated fission track densities, a 'zeta' calibration factor was calculated (Vermeesch, 2009, 2017). The zeta calibration factor is used to overcome any uncertainties of fission track analysis (Hasebe, Barbarand, Jarvis, Carter, & Hurford, 2004) by collating the Durango standard data and comparing it to the data of the unknown grains.

AFT Age Equation (Hasebe et al., 2004)

$$t = \frac{1}{\lambda D} ln(1 + \frac{\lambda D \rho s M}{\lambda f N A 238 U 10 - 6 d R s p k})$$

Where λD = 238U total decay constant (1.55.125x10-10 a-1), λf = 238U spontaneous fission decay constant (8.46x10-17 a-1), NA = Avogadro's number (6.02214x1023 mol-1), d = apatite density (3.19 g/cm2 as in Hasebe et al. (2004)), M = atomic mass of 238U (238.0508 amu), k = observational parameter = 1 (constant), 238U is the samples measured 238-Uranium concentration (μg/g), ρs = spontaneous fission track density (tracks/cm2), and Rsp = the registration factor, corresponding to the range or to half the measured mean confined fission track length.

9.10 Modelling

Calculated zeta ages and Cl data is fed into the RadialPlotter software (Vermeesch, 2009) which constructs a radial plot and calculates the central age for the sample based on the single-grain ages. The central age gives the best estimation of the AFT cooling age. For this study, the central age for the samples are reported in the table within the results section. Samples that have a chi-squared ($\chi 2$) value of >0.05 (O'Sullivan & Parrish, 1995) and/or that recorded a single-grain age dispersion of <25% are regarded as homogenous and hence show a single age population. Alternatively, samples with a chi-squared ($\chi 2$) value of <0.05 or a

single-grain age dispersion >25% are regarded as heterogeneous and potentially show 2 or multiple single age populations. Multiple AFT age-populations, contain different annealing kinetics can be used to help distinguish the two trends, one way of doing so was colour coding Cl abundance on the radial plot to present the different annealing kinetics.

QTQt software developed (Gallagher, 2012) was used to create thermal history plot. The thermal cooling software uses apparent apatite fission track age, the uncertainty of the age, confined track length data and Cl weight percent (wt%) to model the evolution through time (t-T evolution). The granite samples were constrained beneath the APAZ with AU-Pb ages at temperatures of 475±75^{o}C in order to model the rock evolution through the APAZ. Models were constrained to a present day temperature range of 25±5^{o}C with the depositional age being the formation age calculated by the AU-Pb ratio of the individual sample. Modelling of the samples used Monte-Carlo approach which allows many models to be created in order to narrow down the possibilities and picks the best model based on the data. The simulation began with a Burn-in of 10,000 and a Post-Burn-in of 10,000 in order to create 10,000 models and access the plausibility of the model. If the generated model has a cooling path that coincides with the AFT data it is deemed acceptable. These models were then further refined by running a second simulation with an extra 200,000 possible models (200,000 Burn-in, 200,000 Post-Burn-in).

10. APPENDIX B: AFT DATA TABLE

Table 5 – Single-grain AFT data from samples used in this study. ρ_s represents the fission track density of each grain. Ns represents the amount of fission tracks counted in each grain. ^{35}Cl and ^{238}U represent the concentration of those elements in each grain, with the 1σ reporting the analytical uncertainty. t represents the single-grain AFT age, where the 1σ reports the uncertainty. Calculations made with the assistance of in house Excel spreadsheets (e.g. Gillespie et al., 2017; Glorie et al., 2017).

Grain	ρ_s (x10^5/cm^2)	Ns	Cl (ppm)	1σ (ppm)	U (ppm)	1σ (ppm)	t (Ma)	1σ (Ma)
At001 - 1.d	72.66	135	620	250	92.6	2.3	148	12.9

At001 - 2.d	66.52	68	Below LOD	Below LOD	97.9	2.9	128.8	15.7
At001 - 3.d	86.73	119	630	210	106.6	1.5	153.8	14.1
Grain	ρ_s ($x10^5/cm^2$)	Ns	Cl (ppm)	1σ (ppm)	U (ppm)	1σ (ppm)	t (Ma)	1σ (Ma)
At02 - 1.d	17.20	30	Below LOD	Below LOD	49.1	2.6	66.35	12.24
At02 - 2.d	19.20	29	430	250	40.8	3.2	89.29	16.95
At02 - 3.d	19.20	33	Below LOD	Below LOD	22.39	0.67	161.63	28.24
At02 - 4.d	11.20	30	670	200	9.4	0.22	222.72	40.75
At02 - 5.d	5.87	19	Below LOD	Below LOD	5.08	0.2	216.8	49.92
At02 - 6.d	31.40	48	Below LOD	Below LOD	58.3	1.3	101.97	14.76
At02 - 10.d	17.80	13	490	290	55.2	2.5	56.11	17.79
At02 - 11.d	52.70	64	610	240	63.9	2.4	156.2	19.74
At02 - 12.d	26.30	30	Below LOD	Below LOD	16.7	0.6	274.97	52.2
At02 - 13.d	15.50	63	670	230	77.1	2.1	36.42	4.73
At02 - 19.d	8.15	22	840	290	79.8	2.2	19.47	4.16
At02 - 21.d	20.90	125	520	260	25.1	1	157.14	14.4
At02 - 23.d	17.80	56	690	290	52.1	1.3	65.05	8.73
At02 - 24.d	37.10	43	790	220	47.1	1.4	148.6	22.77
At02 - 26.d	44.90	97	550	190	53.4	1.8	158.66	16.33
At02 - 27.d	29.50	28	560	440	104.3	4.8	40.44	8.87
At02 - 29.d	32.70	93	1740	560	38.84	0.9	159.06	16.6
At02 - 30.d	26.10	45	700	290	50.4	2.2	97.83	14.74
Grain	ρ_s ($x10^5/cm^2$)	Ns	Cl (ppm)	1σ (ppm)	U (ppm)	1σ (ppm)	t (Ma)	1σ (Ma)
At-03 - 1.d	21.60	36	2530	320	69.5	1.6	59.33	9.91
At-03 - 2.d	36.30	46	2340	310	111	2.6	62.03	9.17
At-03 - 4.d	31.00	59	1770	190	106.8	3.1	55.01	7.21
At-03 - 5.d	36.00	58	2300	240	106.7	1.6	64.17	8.44
At-03 - 6.d	31.40	52	3190	390	85.2	1.3	70.27	9.76
At-03 - 7.d	31.10	37	1960	230	74	1.5	79.76	13.14
At-03 - 8.d	23.00	54	2330	250	81.7	1.6	53.5	7.3
At-03 - 9.d	28.20	47	2640	270	74.2	1.5	72.04	10.53

At-03 - 10.d	23.40	37	2650	250	57.8	1.4	76.93	12.68
At-03 - 11.d	33.80	33	1950	220	92.8	1.5	69.29	12.07
At-03 - 12.d	35.10	66	2970	380	71.5	1.7	93.11	11.51
At-03 - 13.d	29.80	49	2160	320	72.2	1.4	78.56	11.25
At-03 - 14.d	26.90	44	2170	280	79.8	1.7	63.9	9.66
At-03 - 16.d	33.10	41	2250	320	73	2.5	85.94	13.5
At-03 - 17.d	34.10	42	2120	320	138.7	2.7	46.85	7.24
Grain	ρ_s ($x10^5/cm^2$)	Ns	Cl (ppm)	1σ (ppm)	U (ppm)	1σ (ppm)	t (Ma)	1σ (Ma)
At04 - 3.d	16.15	23	1660	300	51.3	1.6	60.03	12.55
At04 - 4.d	11.20	60	890	260	33.46	0.7	63.59	8.24
At04 - 5.d	19.93	59	850	250	29.8	1.6	124.43	16.54
At04 - 6.d	33.76	74	950	280	54.5	1.1	125.89	14.69
At04 - 7.d	9.88	17	1240	390	48.9	1.5	38.49	9.35
At04 - 8.d	18.51	50	1050	250	57.1	1.8	61.65	8.77
At04 - 9.d	8.67	11	1480	280	45.1	1.3	36.58	11.04
At04 - 10.d	22.83	111	1070	280	61.94	0.97	70.05	6.67
At04 - 11.d	18.11	98	950	190	62.7	1.7	54.95	5.6
At04 - 12.d	20.15	73	580	160	46.8	1.3	81.78	9.64
At04 - 13.d	17.11	23	1140	250	46	1.2	70.88	14.81
At04 - 14.d	10.18	36	1050	360	17.66	0.67	115.54	19.38
At04 - 15.d	13.20	45	810	340	45.2	1.8	55.53	8.35
At04 - 16.d	11.96	26	1610	370	33.7	1.1	67.55	13.29
At04 - 17.d	32.02	55	1110	280	25.28	0.55	237.19	32.09
At04 - 18.d	16.25	47	1400	390	55.35	0.87	55.88	8.16
At04 - 19.d	22.74	57	1200	310	49.4	1.8	87.21	11.66
At04 - 20.d	18.98	70	950	180	42.31	0.89	85.08	10.21
At04 - 21.d	16.27	19	1430	320	27.15	0.52	113.25	26
Grain	ρ_s ($x10^5/cm^2$)	Ns	Cl (ppm)	1σ (ppm)	U (ppm)	1σ (ppm)	t (Ma)	1σ (Ma)
At05 - 1.d	12.76	19	630	210	30.81	0.69	78.6	18
At05 - 3.d	20.82	25	600	140	25.91	0.4	151.8	30.4

Grain	ρ_s ($x10^5/cm^2$)	Ns	Cl (ppm)	1σ (ppm)	U (ppm)	1σ (ppm)	t (Ma)	1σ (Ma)
At08 - 1.d	2.79	5	540	180	2.83	0.17	184.8	82.8
At08 - 2.d	4.35	7	620	250	3.4	0.18	239.7	90.8
At08 - 3.d	1.46	9	450	140	2.65	0.2	104.1	34.9
At08 - 4.d	4.61	6	780	320	9.67	0.28	90.5	37
At08 - 5.d	7.21	7	460	310	9.4	0.37	144.8	54.8
At08 - 6.d	2.35	3	660	210	6.74	0.21	66.1	38.2
Grain	ρ_s ($x10^5/cm^2$)	Ns	Cl (ppm)	1σ (ppm)	U (ppm)	1σ (ppm)	t (Ma)	1σ (Ma)
At09 - 2.d	11.22	15	1070	180	34.41	0.65	61.8	16
At09 - 3.d	9.51	10	790	190	26.9	1	67.3	21.3
At09 - 5.d	7.30	5	1000	270	28.28	0.57	49.1	22
Grain	ρ_s ($x10^5/cm^2$)	Ns	Cl (ppm)	1σ (ppm)	U (ppm)	1σ (ppm)	t (Ma)	1σ (Ma)
At10 - 1.d	5.79	6	660	200	6.84	0.26	159.1	65
At10 - 2.d	6.54	13	650	220	11.25	0.77	110	30.7
At10 - 3.d	14.90	23	720	310	13.17	0.5	211.7	44.3
At10 - 4.d	3.50	6	740	300	6.17	0.29	107.1	43.8
At10 - 5.d	6.75	13	730	160	6.93	0.31	183	50.9
At10 - 6.d	8.87	15	1490	200	10.99	0.59	152.4	39.6
At10 - 7.d	7.77	13	700	180	11.81	0.65	124.7	34.8
Grain	ρ_s ($x10^5/cm^2$)	Ns	Cl (ppm)	1σ (ppm)	U (ppm)	1σ (ppm)	t (Ma)	1σ (Ma)
At11 - 1.d	10.80	12	610	280	24.51	0.77	83.7	24.2
At11 - 2.d	12.20	15	1.27E+05	22000.00	22.6	2.6	102.3	27
At11 - 3.d	8.81	11	610	160	6.73	0.42	245	74.3
At11 - 4.d	9.66	12	450	180	12.26	0.27	149	43.1
At11 - 6.d	14.00	28	Below LOD	Below LOD	10.27	0.41	255.3	48.5
At11 - 7.d	7.80	16	470	180	13.12	0.32	112.6	28.2
At11 - 9.d	5.43	8	560	160	9.17	0.34	112.4	39.8
At11 - 10.d	10.60	16	550	200	5.68	0.33	346.8	87.3
At11 - 11.d	7.84	26	Below LOD	Below LOD	12.78	0.5	116	22.9
At11 - 12.d	14.20	32	470	230	12.26	0.32	216.9	38.4

At11 - 13.d	6.40	17	450	250	5.35	0.19	224.2	54.5
At11 - 15.d	8.69	20	440	280	6.61	0.31	246.5	55.4
At11 - 17.d	16.20	16	610	170	27.56	0.57	111.5	27.9
At11 - 18.d	7.98	7	510	260	24.22	0.89	62.6	23.7
Grain	ρ_s ($x10^5/cm^2$)	Ns	Cl (ppm)	1σ (ppm)	U (ppm)	1σ (ppm)	t (Ma)	1σ (Ma)
At13 - 2.d	18.58	21	490	270	39.64	0.86	88.93	19.43
At13 - 4.d	30.81	47	590	420	29.29	0.78	189.94	27.82
At13 - 5.d	13.77	20	Below LOD	Below LOD	38.1	1.5	68.78	15.44
At13 - 6.d	40.45	43	460	200	47.4	1.3	161.43	24.72
At13 - 8.d	25.09	44	600	230	78.4	2.9	60.97	9.26
At13 - 9.d	10.29	13	600	340	41.8	1.5	46.97	13.06
At13 - 11.d	3.44	8	Below LOD	Below LOD	9.13	0.28	71.43	25.28
At13 - 12.d	9.51	15	600	220	21.63	0.58	83.29	21.54
At13 - 13.d	10.80	24	670	180	37.1	1.1	55.42	11.34
At13 - 15.d	25.15	36	760	370	51.68	0.96	92.38	15.42
At13 - 16.d	13.89	16	720	290	43.2	1.8	61.22	15.36
At13 - 17.d	11.98	15	350	190	10.83	0.78	194.46	50.7
At13 - 18.d	11.89	18	540	180	17.9	0.44	125.96	29.73
At13 - 19.d	7.03	13	710	380	29.96	0.98	52.91	14.7
At13 - 20.d	5.78	8	440	230	14.39	0.42	75.95	26.87
Grain	ρ_s ($x10^5/cm^2$)	Ns	Cl (ppm)	1σ (ppm)	U (ppm)	1σ (ppm)	t (Ma)	1σ (Ma)
At14 - 2.d	4.22	10	590	180	5.59	0.24	142.6	45.2
At14 - 3.d	7.30	8	510	160	16.84	0.43	82	29
At14 - 4.d	2.62	6	570	280	6.9	0.61	117.6	48.3
At14 - 5.d	8.51	17	440	210	11.34	0.53	141.6	34.5
At14 - 6.d	2.79	17	480	160	7.11	0.27	96.4	23.5
At14 - 7.d	7.83	18	360	180	17.37	0.73	85.5	20.2
At14 - 8.d	7.90	16	510	140	17.95	0.47	83.3	20.9
At14 - 9.d	4.18	15	500	120	5.85	0.18	135	34.9
At14 - 10.d	4.38	9	400	170	5.78	0.14	142.8	47.6

At14 - 11.d	7.36	10	460	160	7.08	0.3	201.2	63.8
At14 - 12.d	8.40	17	460	170	8.73	0.38	180.7	44
Grain	ρ_s ($x10^5/cm^2$)	Ns	Cl (ppm)	1σ (ppm)	U (ppm)	1σ (ppm)	t (Ma)	1σ (Ma)
At15 - 1.d	33.70	46	500	200	73.2	1.3	87.02	12.85
At15 - 2.d	16.30	20	480	320	41.9	1.2	73.7	16.51
At15 - 3.d	35.20	69	530	220	120.2	2.3	55.7	6.73
At15 - 4.d	35.90	82	540	260	96.8	1.5	70.27	7.78
At15 - 5.d	36.80	42	Below LOD	Below LOD	146.9	4.1	47.73	7.39
At15 - 7.d	9.60	33	540	170	73.8	1.5	24.78	4.32
At15 - 8.d	20.10	28	450	170	37.43	0.71	101.26	19.16
At15 - 9.d	13.90	31	Below LOD	Below LOD	34.4	0.81	76.73	13.81
At15 - 10.d	13.80	35	290	220	112.9	2.8	23.27	3.94
At15 - 12.d	27.60	36	Below LOD	Below LOD	38.7	1.5	134.23	22.52
At15 - 13.d	14.50	37	Below LOD	Below LOD	66.4	2.2	41.6	6.87
At15 - 17.d	32.90	55	440	150	53.7	1.1	116.09	15.7
At15 - 20.d	32.70	45	450	180	67	1.3	92.3	13.79
Grain	ρ_s ($x10^5/cm^2$)	Ns	Cl (ppm)	1σ (ppm)	U (ppm)	1σ (ppm)	t (Ma)	1σ (Ma)
At16 - 1.d	7.74	8	340	130	22.6	1.1	65.3	23.1
At16 - 3.d	2.87	3	350	140	9.68	0.29	56.7	32.7
At16 - 4.d	6.70	12	470	280	31.31	0.91	44.8	12.9
At16 - 5.d	2.80	5	310	140	9.52	0.38	43.7	19.5
At16 - 6.d	7.44	6	Below LOD	Below LOD	14.45	0.56	97.7	39.9
At16 - 7.d	1.59	2	400	150	5.82	0.26	51.9	36.7
At16 - 8.d	6.05	9	1680	420	8.44	0.46	165.5	58.7
At16 - 9.d	5.28	9	480	170	6.38	0.27	229.4	69.3
At16 - 10.d	3.49	5	420	160	8.8	0.23	75.4	33.8
Grain	ρ_s ($x10^5/cm^2$)	Ns	Cl (ppm)	1σ (ppm)	U (ppm)	1σ (ppm)	t (Ma)	1σ (Ma)
At17 - 1.d	2.92	11	360	110	8.32	0.15	66.6	20.1
At17 - 2.d	4.56	9	480	140	10.78	0.29	80.4	26.8
At17 - 4.d	4.08	17	490	140	14.12	0.9	55	13.5

At17 - 5.d	3.90	8	560	190	11.11	0.4	66.7	23.6
At17 - 6.d	2.98	4	440	150	7.58	0.34	74.8	37.4
At17 - 7.d	2.95	4	300	180	3.06	0.37	181	91.2
At17 - 8.d	2.70	4	450	130	8.23	0.27	62.4	31.2
At17 - 10.d	3.64	7	460	150	5.52	0.46	124.9	47.5
At17 - 11.d	6.21	11	480	140	9.18	0.23	128	38.6
At17 - 13.d	2.73	6	470	140	5.39	0.18	95.9	39.2
At17 - 14.d	3.47	10	420	150	6.78	0.65	97.1	31.1
At17 - 15.d	4.50	5	400	150	8.65	0.24	98.7	44.2
At17 - 16.d	4.07	8	280	120	9.16	0.37	84.1	29.8
At17 - 17.d	6.56	12	480	140	9.7	0.43	127.8	37
At17 - 18.d	3.86	7	340	140	5.55	0.24	131	49.6
At17 - 19.d	2.62	6	480	140	4.7	0.17	105.6	43.2
Grain	ρ_s ($x10^5/cm^2$)	Ns	Cl (ppm)	1σ (ppm)	U (ppm)	1σ (ppm)	t (Ma)	1σ (Ma)
At18 - 1.d	13.50	17	490	190	27.52	0.79	93	22.6
At18 - 2.d	6.35	16	340	120	28.98	0.66	41.7	10.4
At18 - 3.d	12.00	44	390	200	27.54	0.86	82.8	12.6
At18 - 4.d	12.40	20	Below LOD	Below LOD	24.1	2.3	97.1	22.2
At18 - 6.d	10.50	35	410	170	27.3	1.2	72.9	12.4
At18 - 7.d	16.50	22	Below LOD	Below LOD	24.35	0.52	128.5	27.4
At18 - 9.d	16.60	27	480	260	57.3	1.2	55	10.6
At18 - 10.d	8.97	32	270	180	21.05	0.5	80.8	14.3
At18 - 11.d	6.65	7	420	150	21.63	0.86	58.6	22.2
Grain	ρ_s ($x10^5/cm^2$)	Ns	Cl (ppm)	1σ (ppm)	U (ppm)	1σ (ppm)	t (Ma)	1σ (Ma)
At19 - 2.d	13.10	38	420	140	21.69	0.45	113.98	18.53
At19 - 3.d	7.24	8	330	150	16.66	0.55	82.11	29.06
At19 - 4.d	5.90	8	330	160	18.28	0.47	61.17	21.64
At19 - 5.d	20.70	38	660	270	51.7	1.7	75.85	12.37
At19 - 6.d	23.30	48	590	170	41.7	1	105.86	15.33
At19 - 7.d	7.96	11	560	190	25.62	0.43	59.15	17.84

At19 - 8.d	9.55	23	400	140	31	1.3	58.54	12.27
At19 - 9.d	11.90	29	460	140	45.3	1.8	50.12	9.36
At19 - 10.d	8.29	27	430	160	26.46	0.53	59.51	11.47

11. APPENDIX C: AU-Pb DATA TABLE

Table 6 – Single grain AU-Pb data as calculated using Iolite software (Paton et al., 2011) for all samples used in this study. Final 238/206 and 207/206 represent the ratio concentrations of $^{238}U/^{206}Pb$ and $^{207}Pb/^{206}Pb$ with 2σ reporting the standard error. Error correlation represents the correlation of standard error between $^{238}U/^{206}Pb$ and $^{207}Pb/^{206}Pb$. Final 207 Age represents common-Pb corrected Au-Pb ages with 2σ reporting the standard error.

Grain	Final 238/206	2σ	Final 207/206	2σ	Error Correlation 238/206 vs 207/206	Final 207 age (Ma)	2σ (Ma)
At001 - 1.d	14.51	0.59	0.33	0.02	0.39	148	12.9
At001 - 2.d	24.15	0.82	0.05	0.00	0.03	128.8	15.7
At001 - 3.d	15.92	0.56	0.28	0.01	0.28	153.8	14.1
Grain	Final 238/206	2σ	Final 207/206	2σ	Error Correlation 238/206 vs 207/206	Final 207 age (Ma)	2σ (Ma)
At02 - 1.d	20.12	0.73	0.17	0.01	0.17	261.60	17.00
At02 - 2.d	18.80	0.78	0.18	0.01	-0.39	274.60	11.00
At02 - 5.d	18.80	0.81	0.20	0.01	0.32	269.00	16.00
At02 - 6.d	19.84	0.79	0.18	0.01	0.40	264.40	14.00
At02 - 10.d	20.12	0.69	0.16	0.01	0.49	266.20	15.00
At02 - 11.d	21.05	0.84	0.14	0.01	0.45	269.00	19.00
At02 - 12.d	16.39	0.62	0.26	0.02	0.50	270.00	25.00
At02 - 13.d	21.14	0.80	0.13	0.01	0.33	267.20	12.00
At02 - 20.d	15.29	0.65	0.31	0.02	0.49	268.00	20.00
At02 - 21.d	17.39	0.67	0.24	0.01	0.04	269.30	17.00
At02 - 23.d	20.08	0.89	0.15	0.01	-0.39	271.10	11.00
At02 - 24.d	19.72	0.78	0.19	0.01	-0.27	264.00	15.00
At02 - 26.d	18.62	0.83	0.18	0.01	-0.40	274.70	11.00
At02 - 27.d	20.79	0.95	0.14	0.01	-0.59	264.60	9.80
At02 - 29.d	19.88	1.03	0.13	0.01	0.08	281.50	14.00
At02 - 30.d	20.04	0.96	0.16	0.01	-0.30	266.30	13.00

Grain	Final 238/206	2σ	Final 207/206	2σ	Error Correlation 238/206 vs 207/206	Final 207 age (Ma)	2σ (Ma)
At-03 - 1.d	15.72	0.57	0.32	0.01	0.16	248.00	17.00
At-03 - 2.d	17.01	0.61	0.25	0.01	0.30	262.30	13.00
At-03 - 4.d	19.01	0.72	0.21	0.01	0.21	254.90	11.00
At-03 - 6.d	16.37	0.64	0.27	0.01	0.36	264.00	17.00
At-03 - 7.d	17.99	0.68	0.23	0.01	0.40	258.70	14.00
At-03 - 8.d	16.16	0.60	0.28	0.01	0.44	259.00	20.00
At-03 - 9.d	15.60	0.58	0.31	0.01	0.31	255.20	14.00
At-03 - 10.d	14.84	0.55	0.32	0.01	0.21	258.00	18.00
At-03 - 11.d	18.05	0.65	0.23	0.01	0.41	259.80	13.00
At-03 - 12.d	14.41	0.56	0.32	0.01	0.46	266.00	22.00
At-03 - 13.d	15.75	0.60	0.30	0.01	0.45	258.50	16.00
At-03 - 14.d	17.48	0.67	0.26	0.01	0.38	254.80	16.00
At-03 - 16.d	15.08	0.55	0.31	0.01	0.26	262.20	18.00
At-03 - 17.d	19.42	0.72	0.20	0.01	0.40	256.00	13.00
Grain	Final 238/206	2σ	Final 207/206	2σ	Error Correlation 238/206 vs 207/206	Final 207 age (Ma)	2σ (Ma)
At04 - 3.d	18.12	0.82	0.28	0.01	0.24	231.60	231.60
At04 - 4.d	14.22	0.77	0.40	0.02	0.58	220.00	220.00
At04 - 5.d	12.95	0.64	0.43	0.02	0.25	221.00	221.00
At04 - 6.d	17.36	0.81	0.31	0.01	-0.23	225.90	225.90
At04 - 7.d	17.79	0.85	0.32	0.01	0.21	218.00	218.00
At04 - 8.d	18.42	0.88	0.30	0.01	0.55	221.20	221.20
At04 - 9.d	17.15	0.85	0.32	0.01	0.67	228.00	228.00
At04 - 10.d	18.45	0.85	0.27	0.01	0.38	233.90	233.90
At04 - 11.d	18.21	0.83	0.27	0.01	0.20	236.40	236.40
At04 - 12.d	16.78	0.76	0.31	0.01	0.27	233.00	233.00
At04 - 13.d	16.18	0.73	0.31	0.01	0.43	243.70	243.70
At04 - 15.d	17.86	0.92	0.31	0.02	0.27	224.00	224.00
At04 - 16.d	14.33	0.68	0.35	0.02	0.22	246.00	246.00
At04 - 17.d	13.16	0.64	0.43	0.02	0.67	221.00	221.00

At04 - 18.d	16.50	0.82	0.30	0.01	0.26	247.10	247.10
At04 - 19.d	16.53	0.76	0.33	0.02	0.44	231.00	231.00
At04 - 20.d	15.82	0.70	0.32	0.01	0.51	243.30	243.30
Grain	Final 238/206	2σ	Final 207/206	2σ	Error Correlation 238/206 vs 207/206	Final 207 age (Ma)	2σ (Ma)
At05 - 1.d	14.06	0.67	0.35	0.01	0.56	377.00	21.00
At05 - 3.d	13.74	0.70	0.39	0.02	0.66	377.00	24.00
Grain	Final 238/206	2σ	Final 207/206	2σ	Error Correlation 238/206 vs 207/206	Final 207 age (Ma)	2σ (Ma)
At08 - 1.d	2.21	0.15	0.73	0.03	0.35	210.00	170.00
At08 - 2.d	2.02	0.15	0.74	0.04	0.25	200.00	230.00
At08 - 3.d	2.12	0.16	0.72	0.03	0.20	250.00	140.00
At08 - 4.d	4.03	0.33	0.68	0.04	-0.07	212.00	99.00
At08 - 5.d	5.07	0.28	0.60	0.02	0.21	306.00	62.00
At08 - 6.d	6.46	0.41	0.67	0.04	0.15	149.00	64.00
Grain	Final 238/206	2σ	Final 207/206	2σ	Error Correlation 238/206 vs 207/206	Final 207 age (Ma)	2σ (Ma)
At09 - 2.d	12.09	0.56	0.34	0.01	-0.16	-15.00	56.00
At09 - 3.d	10.66	0.56	0.46	0.02	0.54	-265.00	69.00
At09 - 5.d	9.86	0.46	0.33	0.01	0.21	22.00	54.00
Grain	Final 238/206	2σ	Final 207/206	2σ	Error Correlation 238/206 vs 207/206	Final 207 age (Ma)	2σ (Ma)
At10 - 1.d	4.05	0.25	0.64	0.03	0.26	453.00	85.00
At10 - 2.d	6.96	0.48	0.50	0.03	0.18	403.00	55.00
At10 - 3.d	3.94	0.23	0.68	0.03	0.26	397.00	74.00
At10 - 4.d	4.95	0.32	0.60	0.03	0.47	440.00	69.00
At10 - 5.d	6.69	0.38	0.51	0.02	0.22	411.00	50.00
At10 - 6.d	7.20	0.41	0.49	0.02	-0.01	415.00	33.00
At10 - 7.d	4.05	0.25	0.64	0.03	0.26	453.00	85.00
Grain	Final 238/206	2σ	Final 207/206	2σ	Error Correlation 238/206 vs 207/206	Final 207 age (Ma)	2σ (Ma)
At11 - 1.d	13.33	0.64	0.40	0.02	0.17	251.00	26.00
At11 - 2.d	5.92	0.77	0.66	0.11	0.82	200.00	190.00
At11 - 3.d	6.75	0.44	0.57	0.03	0.25	275.00	49.00
At11 - 4.d	7.91	0.38	0.56	0.03	0.40	259.00	64.00

At11 - 6.d	8.01	0.53	0.54	0.03	-0.08	272.00	46.00
At11 - 7.d	8.46	0.44	0.54	0.02	0.57	262.00	46.00
At11 - 9.d	8.90	0.50	0.52	0.03	0.50	265.00	46.00
At11 - 10.d	5.39	0.38	0.63	0.03	0.51	265.00	57.00
At11 - 11.d	9.43	0.59	0.50	0.03	-0.06	268.00	36.00
At11 - 12.d	8.48	0.42	0.54	0.02	0.54	263.00	52.00
At11 - 13.d	7.33	0.49	0.61	0.03	0.28	212.00	47.00
At11 - 15.d	7.72	0.50	0.62	0.04	0.16	201.00	57.00
At11 - 17.d	12.87	0.63	0.42	0.01	0.18	250.00	24.00
At11 - 18.d	11.61	0.61	0.44	0.02	0.76	265.00	33.00
Grain	Final 238/206	2σ	Final 207/206	2σ	Error Correlation 238/206 vs 207/206	Final 207 age (Ma)	2σ (Ma)
At13 - 2.d	19.42	1.24	0.38	0.02	0.35	176.00	21.00
At13 - 4.d	16.72	0.89	0.43	0.02	0.21	181.00	23.00
At13 - 5.d	20.04	0.96	0.40	0.01	0.66	163.90	16.00
At13 - 6.d	24.24	1.12	0.32	0.01	0.35	162.40	16.00
At13 - 8.d	19.34	1.31	0.36	0.02	-0.48	186.00	15.00
At13 - 9.d	20.83	1.00	0.40	0.02	0.05	157.00	19.00
At13 - 11.d	9.12	0.52	0.63	0.03	0.64	139.00	47.00
At13 - 12.d	17.12	1.00	0.45	0.03	0.39	166.00	27.00
At13 - 13.d	20.00	1.00	0.39	0.02	0.33	165.90	16.00
At13 - 15.d	23.26	1.08	0.34	0.01	0.22	162.10	14.00
At13 - 16.d	21.60	1.07	0.36	0.02	0.38	166.30	16.00
At13 - 18.d	13.59	0.72	0.53	0.02	0.29	155.00	26.00
At13 - 19.d	18.59	0.97	0.44	0.02	0.55	156.00	19.00
At13 - 20.d	12.90	0.68	0.55	0.02	0.53	145.00	28.00
Grain	Final 238/206	2σ	Final 207/206	2σ	Error Correlation 238/206 vs 207/206	Final 207 age (Ma)	2σ (Ma)
At14 - 2.d	5.52	0.25	0.64	0.03	0.08	298.00	47.00
At14 - 4.d	6.50	0.32	0.65	0.03	0.51	260.00	49.00
At14 - 5.d	8.87	0.44	0.53	0.03	0.61	292.00	39.00
At14 - 6.d	7.73	0.32	0.61	0.03	0.25	251.00	47.00

At14 - 7.d	10.87	0.48	0.47	0.02	0.28	281.00	29.00
At14 - 8.d	10.83	0.45	0.47	0.02	0.46	279.00	25.00
At14 - 9.d	5.42	0.29	0.66	0.03	0.63	282.00	58.00
At14 - 10.d	5.75	0.36	0.68	0.03	0.38	243.00	51.00
At14 - 11.d	6.57	0.32	0.59	0.02	0.57	315.00	43.00
At14 - 12.d	7.43	0.30	0.59	0.03	0.57	277.00	42.00
Grain	Final 238/206	2σ	Final 207/206	2σ	Error Correlation 238/206 vs 207/206	Final 207 age (Ma)	2σ (Ma)
At15 - 1.d	11.39	0.36	0.46	0.01	0.07	255.50	16.00
At15 - 2.d	10.18	0.34	0.51	0.01	0.58	254.00	24.00
At15 - 3.d	13.09	0.41	0.38	0.01	0.29	273.10	18.00
At15 - 4.d	11.24	0.37	0.43	0.01	0.58	283.00	17.00
At15 - 5.d	13.70	0.43	0.36	0.00	0.27	273.50	12.00
At15 - 7.d	13.64	0.41	0.38	0.01	0.47	264.40	17.00
At15 - 8.d	6.52	0.23	0.60	0.01	0.19	280.00	29.00
At15 - 9.d	5.91	0.19	0.62	0.01	0.27	275.00	41.00
At15 - 10.d	12.33	0.37	0.41	0.01	0.35	268.20	20.00
At15 - 12.d	8.60	0.46	0.57	0.02	-0.02	240.00	26.00
At15 - 13.d	11.53	0.37	0.43	0.02	0.12	274.00	24.00
At15 - 17.d	10.14	0.35	0.50	0.02	0.31	262.00	27.00
At15 - 20.d	10.96	0.38	0.48	0.02	0.32	254.00	23.00
Grain	Final 238/206	2σ	Final 207/206	2σ	Error Correlation 238/206 vs 207/206	Final 207 age (Ma)	2σ (Ma)
At16 - 1.d	15.08	0.61	0.44	0.02	0.13	171.00	21.00
At16 - 3.d	9.08	0.40	0.56	0.03	0.09	151.00	38.00
At16 - 4.d	17.83	0.89	0.40	0.02	0.49	165.00	18.00
At16 - 5.d	9.08	0.45	0.61	0.03	0.48	99.00	43.00
At16 - 6.d	9.75	0.51	0.47	0.02	-0.12	227.00	27.00
At16 - 7.d	6.13	0.56	0.63	0.04	0.27	111.00	80.00
At16 - 8.d	6.94	0.53	0.61	0.06	0.44	129.00	86.00
At16 - 9.d	5.29	0.31	0.60	0.03	0.29	188.00	73.00
At16 - 10.d	6.63	0.26	0.57	0.02	0.57	202.00	56.00

Grain	Final 238/206	2σ	Final 207/206	2σ	Error Correlation 238/206 vs 207/206	Final 207 age (Ma)	2σ (Ma)
At17 - 1.d	5.56	0.23	0.70	0.03	0.62	155.00	54.00
At17 - 2.d	6.89	0.25	0.65	0.02	0.33	193.00	44.00
At17 - 4.d	6.29	0.55	0.71	0.06	-0.17	112.00	74.00
At17 - 5.d	7.31	0.38	0.72	0.03	0.20	97.00	37.00
At17 - 6.d	6.11	0.33	0.70	0.03	0.30	154.00	57.00
At17 - 8.d	5.46	0.26	0.70	0.02	0.45	169.00	45.00
At17 - 10.d	3.86	0.31	0.73	0.03	0.16	172.00	85.00
At17 - 11.d	6.58	0.29	0.68	0.03	0.52	168.00	45.00
At17 - 13.d	3.96	0.17	0.74	0.03	0.23	143.00	82.00
At17 - 14.d	4.08	0.32	0.71	0.03	-0.02	175.00	61.00
At17 - 15.d	5.58	0.25	0.69	0.02	0.33	172.00	45.00
At17 - 16.d	6.18	0.33	0.69	0.02	0.35	152.00	40.00
At17 - 17.d	5.86	0.31	0.67	0.03	0.02	187.00	49.00
At17 - 18.d	4.42	0.23	0.74	0.03	0.07	121.00	69.00
At17 - 19.d	3.47	0.19	0.75	0.03	0.64	160.00	89.00
Grain	Final 238/206	2σ	Final 207/206	2σ	Error Correlation 238/206 vs 207/206	Final 207 age (Ma)	2σ (Ma)
At18 - 1.d	8.50	0.34	0.63	0.03	0.83	204.00	43.00
At18 - 2.d	8.94	0.31	0.60	0.01	0.41	218.00	20.00
At18 - 3.d	9.78	0.37	0.60	0.02	0.35	195.00	22.00
At18 - 6.d	7.23	0.29	0.66	0.02	0.20	199.00	32.00
At18 - 7.d	7.73	0.33	0.65	0.02	0.33	207.00	36.00
At18 - 9.d	12.95	0.40	0.51	0.01	0.49	203.60	16.00
At18 - 10.d	6.83	0.28	0.69	0.02	0.43	178.00	27.00
At18 - 11.d	7.35	0.31	0.64	0.02	0.44	227.00	36.00
Grain	Final 238/206	2σ	Final 207/206	2σ	Error Correlation 238/206 vs 207/206	Final 207 age (Ma)	2σ (Ma)
At19 - 2.d	8.39	0.32	0.65	0.02	0.60	163.00	34.00
At19 - 3.d	6.30	0.24	0.68	0.02	0.49	173.00	40.00
At19 - 4.d	7.50	0.27	0.67	0.02	0.19	157.00	36.00
At19 - 5.d	13.14	0.55	0.53	0.01	-0.15	177.90	12.00

At19 - 6.d	11.67	0.37	0.56	0.01	0.31	183.00	22.00
At19 - 7.d	9.06	0.34	0.61	0.02	0.59	186.00	29.00
At19 - 8.d	13.30	0.60	0.56	0.02	0.18	157.00	18.00
At19 - 9.d	13.79	0.48	0.53	0.01	0.13	168.90	15.00
At19 - 10.d	8.29	0.29	0.63	0.02	0.38	178.00	27.00

12. APPENDIX D: THERMAL HISTORY MODELS

12.1 Individual thermal history plots

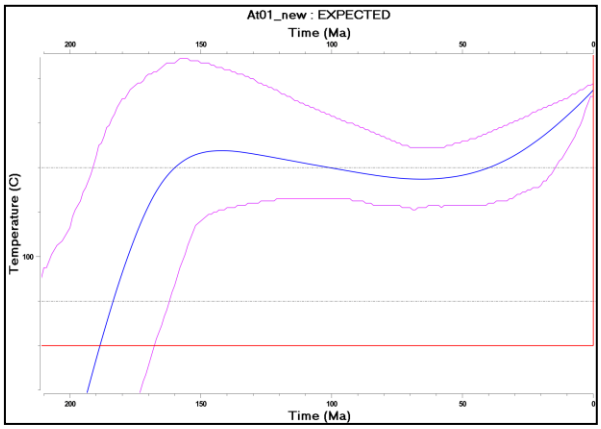

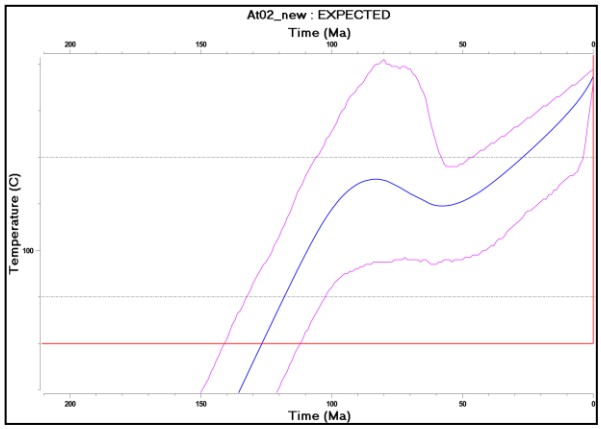

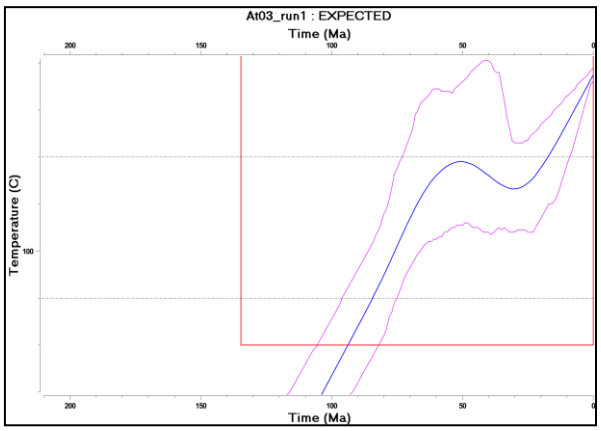

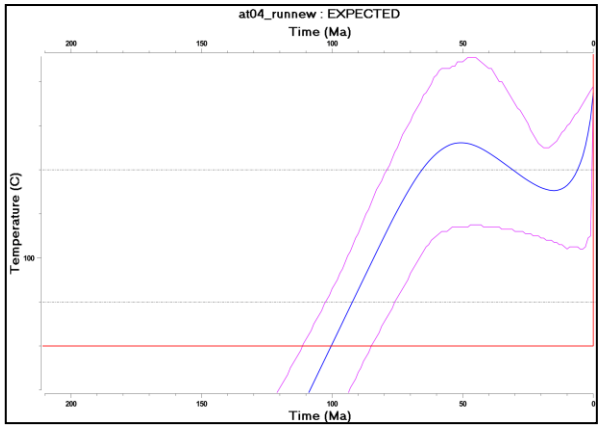

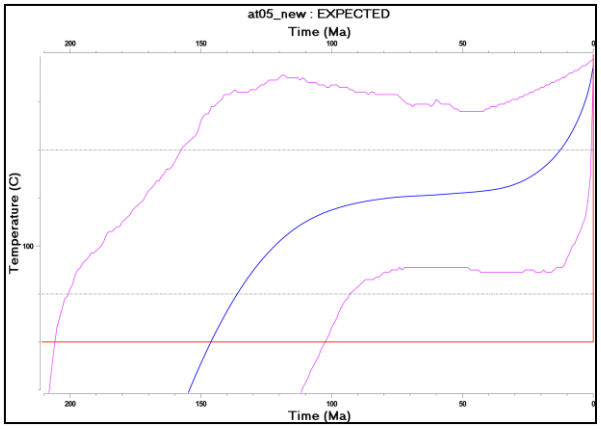

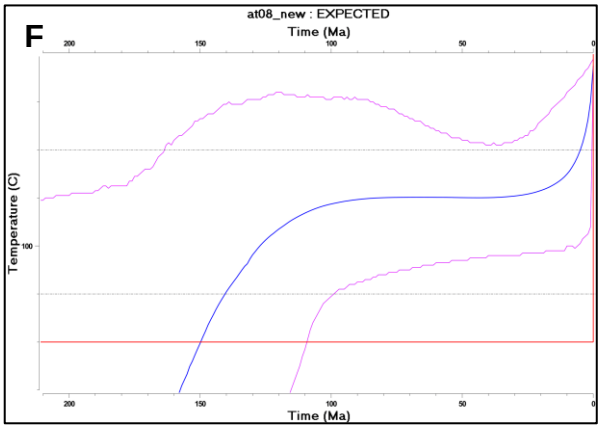

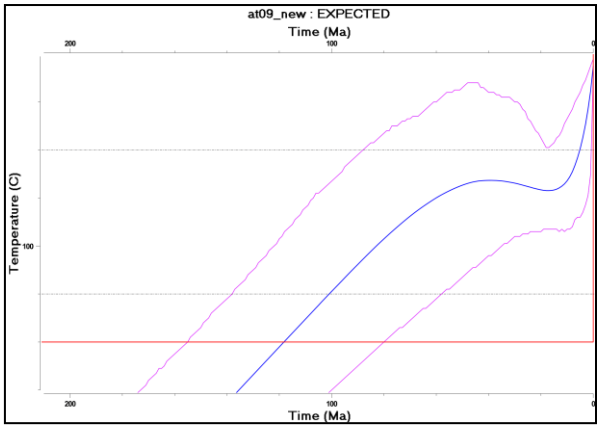

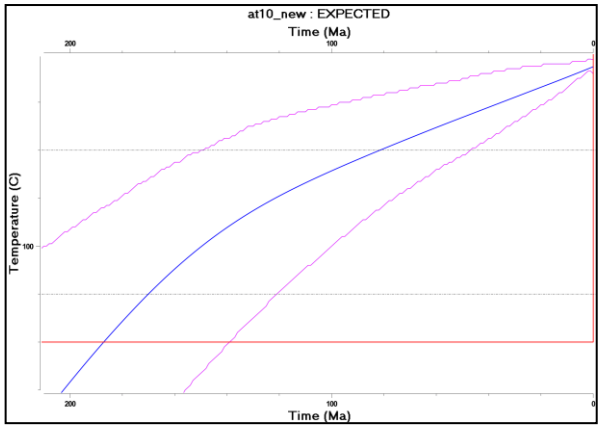

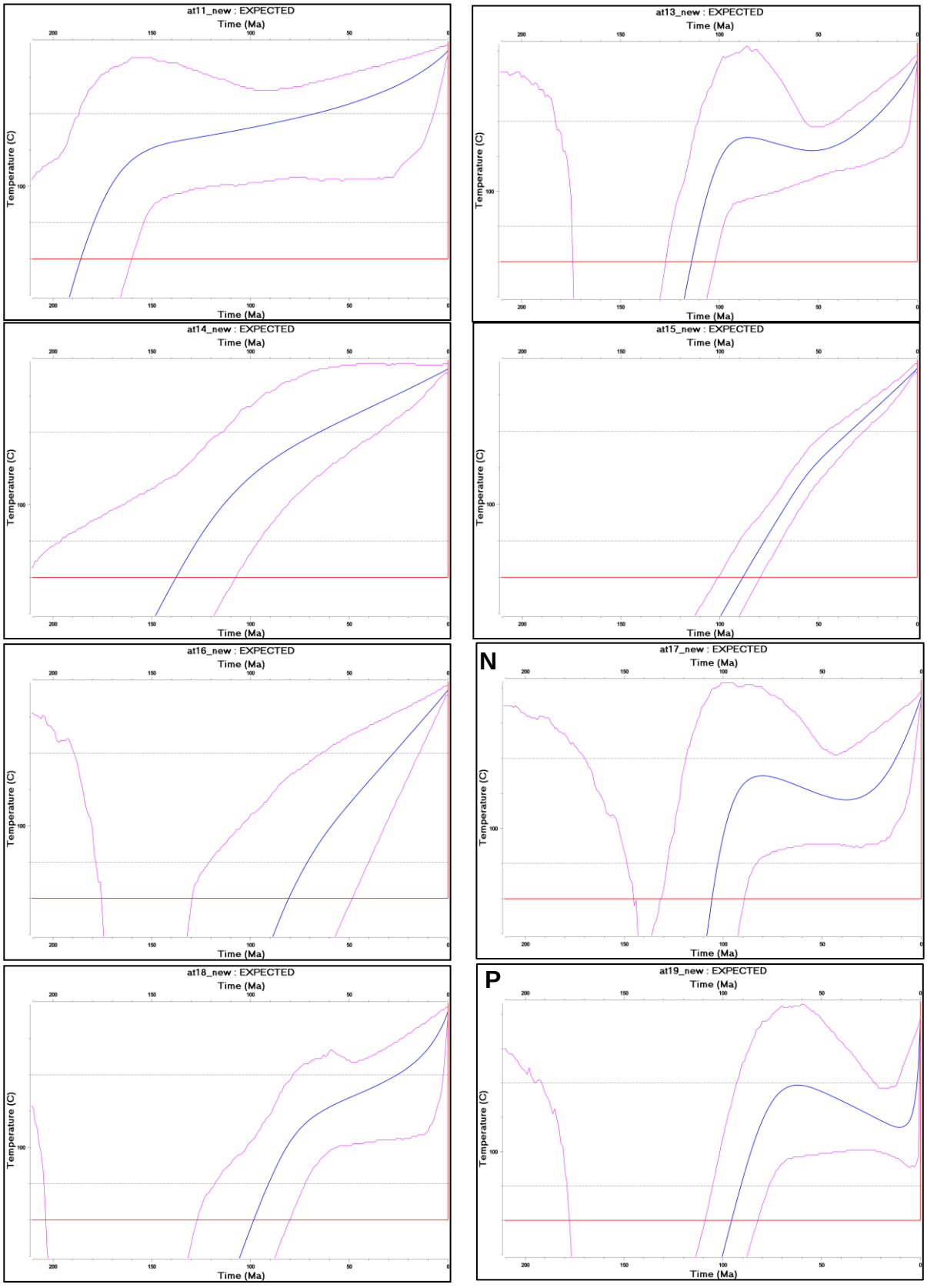

Figure 15 – Expected thermal history plots for all samples (A-P), with focus around the APAZ. Temperature (ºC) is on the y-axis, whilst time (Ma) is on the x-axis. Dashed lines represent the upper and lower temperature of the APAZ (60-120 ºC). Purple lines represent the upper and lower limits of the expected model, with the blue line representing the best fit. The red line does not represent anything of importance.

12.2 Individual T(t) plots

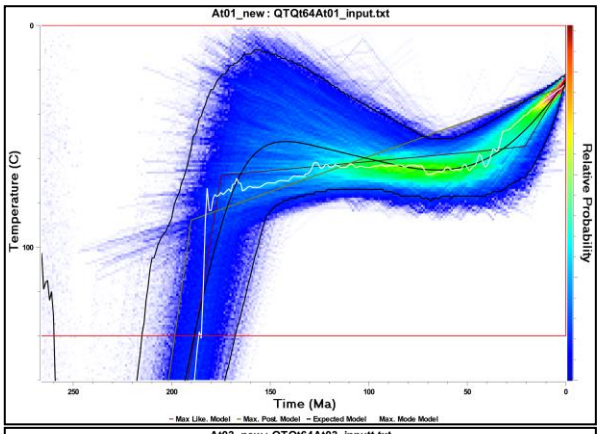

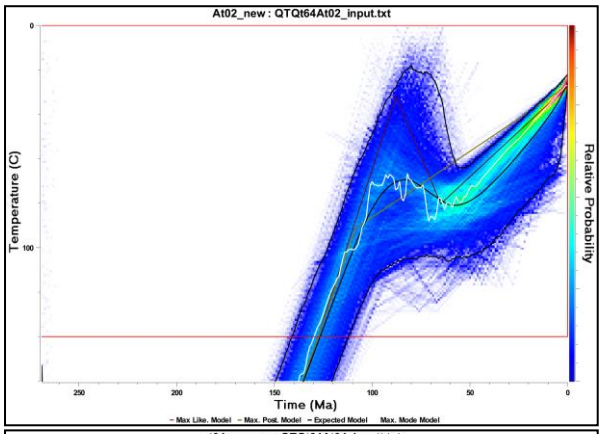

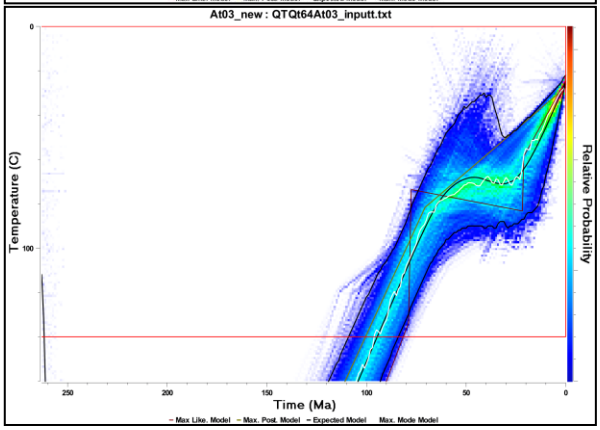

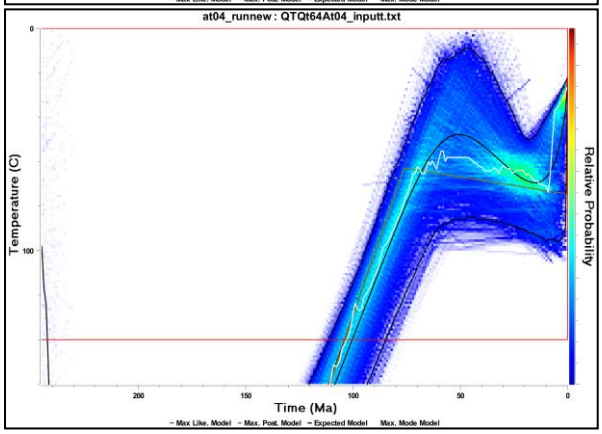

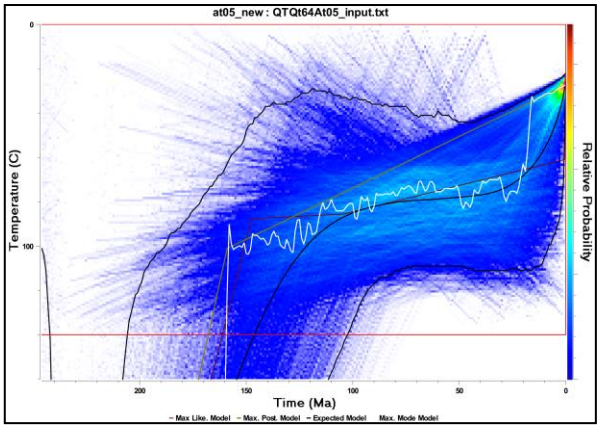

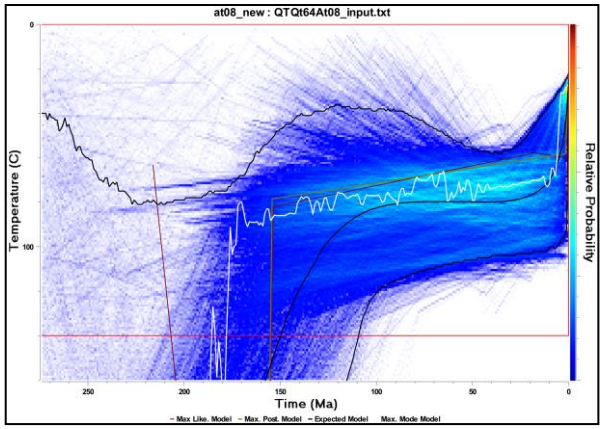

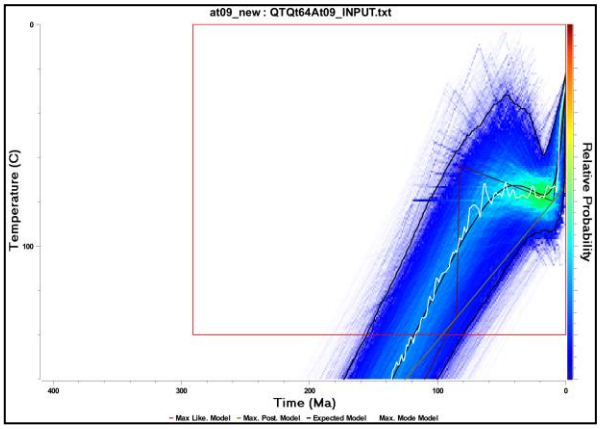

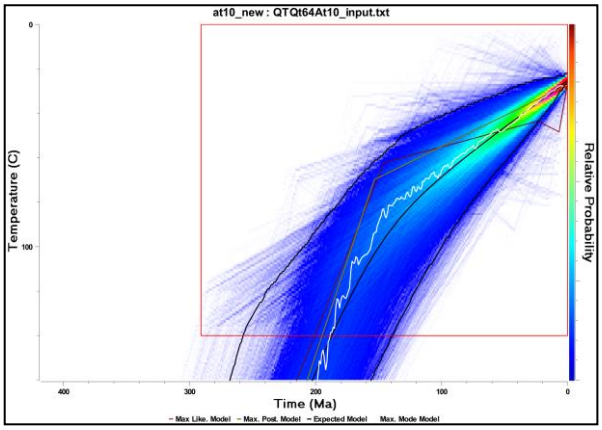

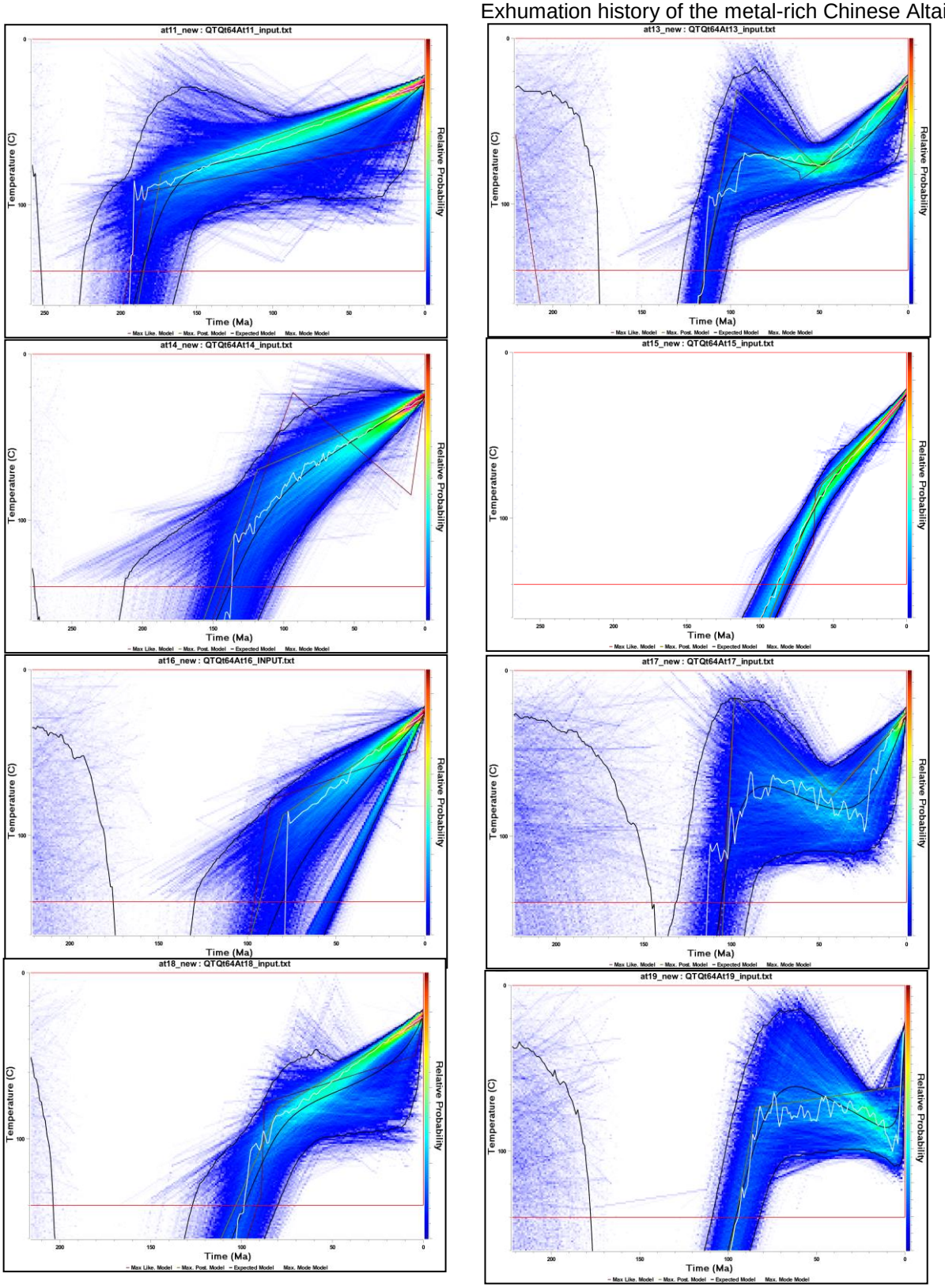

Figure 16 – Predicted thermal history plot for all samples (A-P) with focus around the APAZ (60-120 ºC). The left y-axis represents temperature (ºC) whilst the right y-axis represents a relative probability colour code where warmer colours represent high probability and cooler colours represent high uncertainty. The x-axis represents time (Ma). The black lines represent the model's upper and lower limits as well as a smoothed best fit line. The light blue line that overlays the smoothed best fit line represents the true best fit line. The red lines represent nothing of importance.

12.3 Individual prediction histogram plots

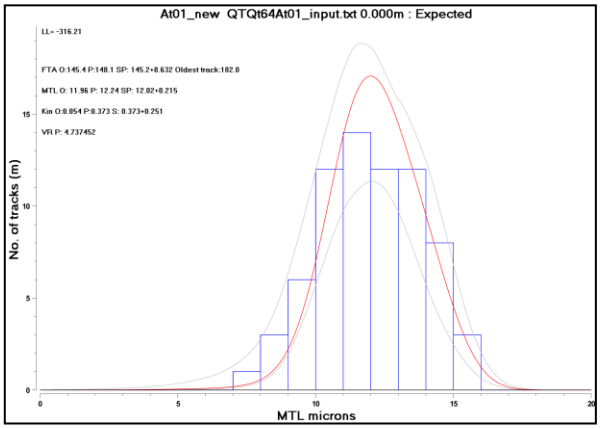

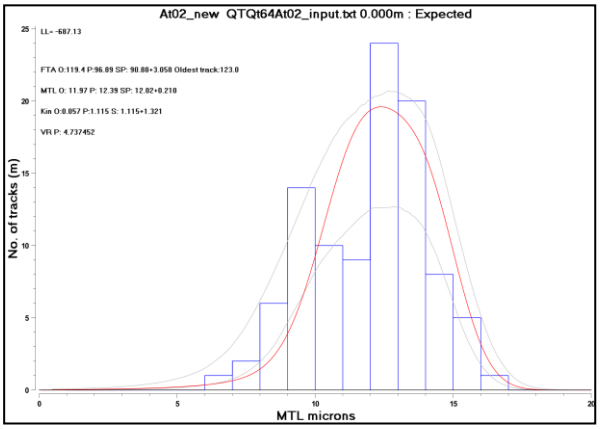

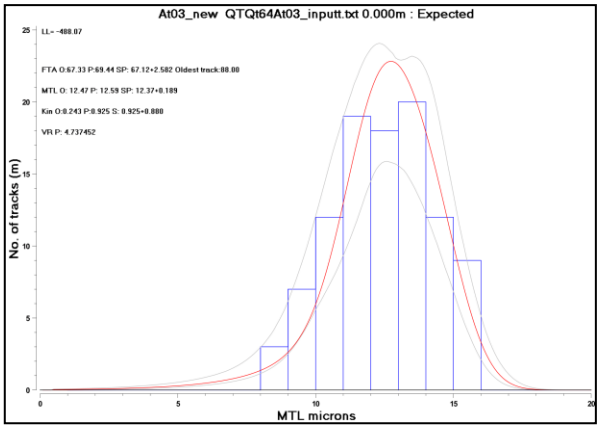

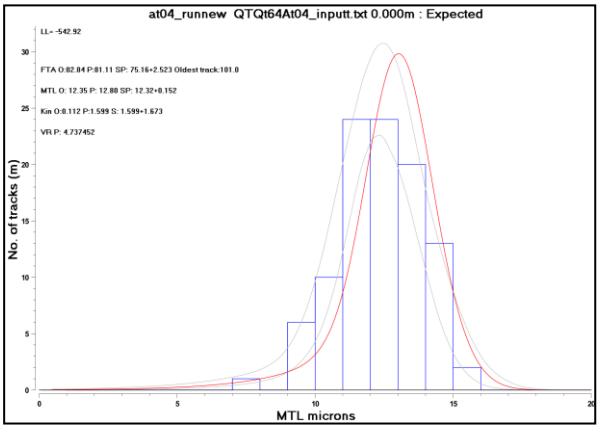

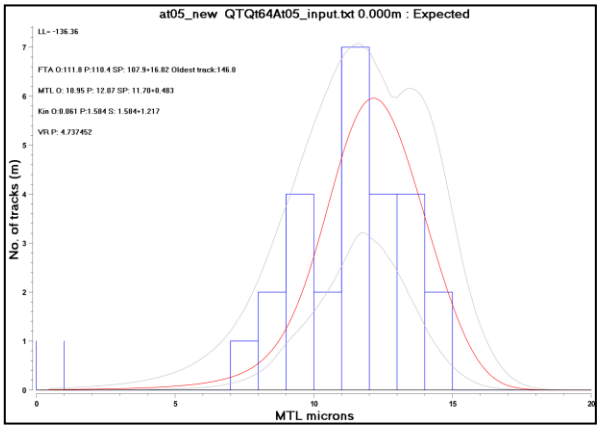

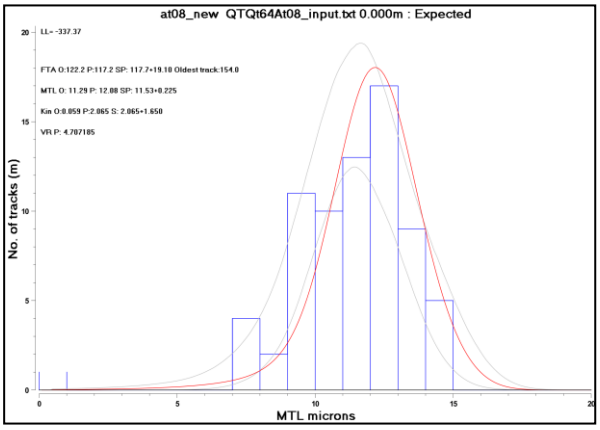

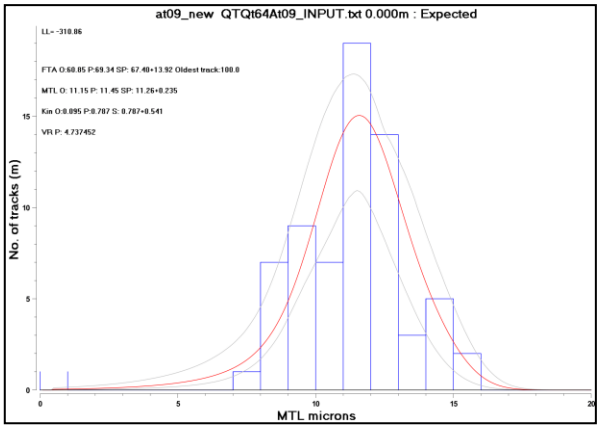

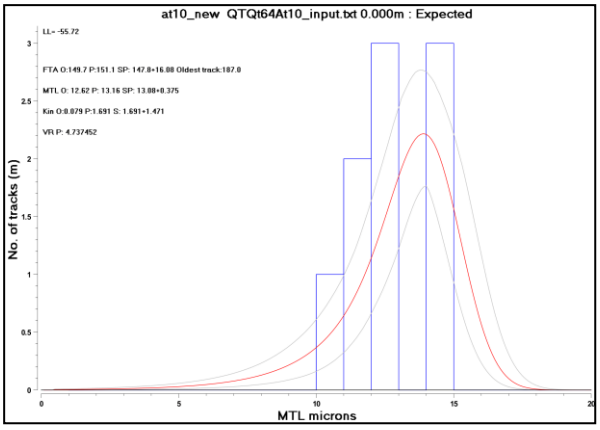

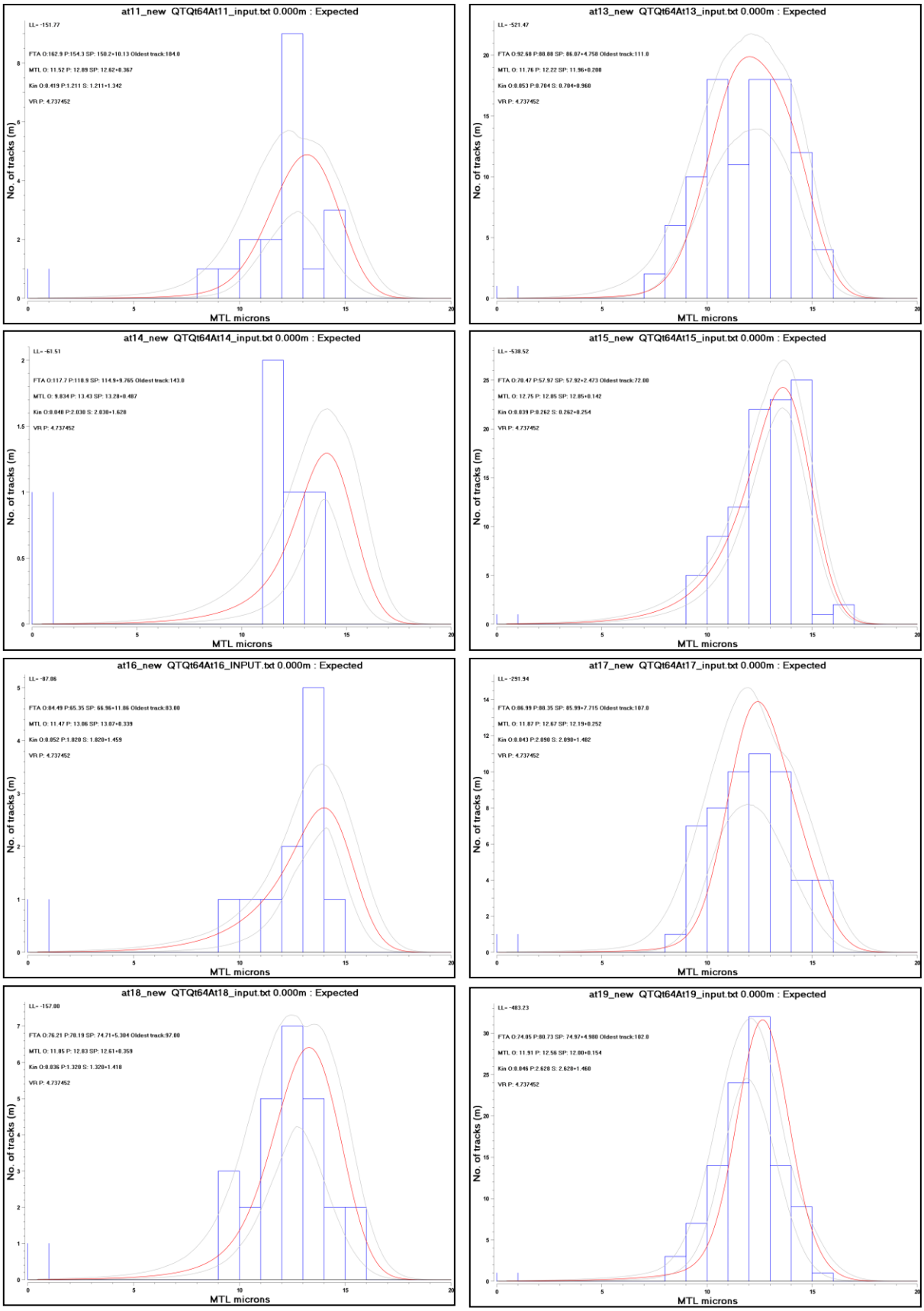

Figure 17 – Predicted histogram plots for all samples (A-P) showing the distribution of mean track lengths (MTLs) on the x-axis per number of measured confined tracks (y-axis). FTA represents fission track age in Ma. Kin represents the kinetic parameter, for this study, Cl. O represents the observed value, whilst P represents the predicted value.